이학박사학위논문

Generation of Entanglement with Two-dimensional Motion in a Trapped Ion System

포획된 이온의 2차원 운동을 이용한 양자 얽힘 생성

2023 년 8 월

서울대학교 대학원

물리천문학부

전 홍 기

Generation of Entanglement with Two-dimensional Motion in a Trapped Ion System

포획된 이온의 2차원 운동을 이용한 양자 얽힘 생성

지도교수 신 용 일

이 논문을 이학박사 학위논문으로 제출함

2023 년 6 월

서울대학교 대학원

물리천문학부 물리학전공

전 홍 기

전홍기의 이학박사 학위논문을 인준함

2023 년 6 월

위 원 장	안경원	(인)
부위원장	신용일	(인)
위 원	김도헌	(인)
위 원	김태현	(인)
위 원	김준기	(인)

Generation of Entanglement with Two-dimensional Motion in a Trapped Ion System

by

Honggi Jeon, B.S.

Dissertation

Presented to the Faculty of the Graduate School of

Seoul National University

in Partial Fulfillment

of the Requirements

for the Degree of

Doctor of Philosophy

Seoul National University

August 2023

Abstract

Honggi Jeon
Department of Physics and Astronomy
The Graduate School
Seoul National University

A quantum system quickly becomes intractable for classical computers because the required computation increases exponentially with the size of the system. The field of quantum computing emerged in an effort to simulate quantum systems with a computer that operates based on quantum mechanics. Since it works in a way that is fundamentally different from the classical computer, certain calculations, such as factoring a large number, has been shown to be much faster when done by quantum algorithms.

The quantum computer can be constructed using any sufficiently stable and highly controllable quantum system. The trapped ion quantum computer, one of the most popular platforms, electrodynamically confines a chain of atomic ions and uses their spin and motion for quantum information processing.

In this thesis, we demonstrate how the two-dimensional motion in a trapped ion system can be used to generate various quantum states, including qubit Bell states and entangled coherent states of motion. These experiments require a very well controlled and stable system. Thus we first discuss the development of a trapped ion experimental setup on which all the results presented here were carried out. Each subsystem will be examined and its design will be discussed.

The basic characterization of the system, including heating rates, various

coherence times and micromotion measurement results will be presented. A universal quantum gate set consisting of single qubit rotations and two-qubit entangling gates has been successfully implemented with the current setup. We discuss their experimental realization and characterization, which will be a valuable resource for the future experiments with the setup.

Next, the results of the experiments involving the two-dimensional motion of the ion will be presented. The entangled coherent state, a multi-mode extension of the cat state has been the subject of intense theoretical research in the last few decades due to its usefulness in quantum metrology, communication and computation. It is also relevant in the study of encoded qubits. It has been experimentally realized with photons and superconducting circuits, but not with trapped ions so far. In our setup, we successfully implemented entangled coherent states with the transverse degrees of freedom of a single trapped ion using a two-dimensional spin-dependent force and projective measurement of the spin. The modulation of phonon number state parity has been measured in order to observe and characterize the periodic entanglement of the motional states. We also demonstrate that the two-dimensional force can be used to drive Mølmer-Sørensen interaction with a chain of two ions, and experimentally verify that it reduces the required laser power.

This work demonstrates the successful construction of a trapped ion quantum computer and shows how two-dimensional motion in a trapped ion system can be used for the generation of entangled quantum states, the two qubit Bell state and entangled coherent state. The letter is especially of significance considering that it is equivalent to the Bell state of two qubit states encoded in coherent states. The generation of entangled coherent states reported here can facilitate the study and utilization of encoded qubits.

Keywords: Trapped ion, quantum computer, quantum computation, entangled coherent state, two-qubit gate, single-qubit gate

Student Number: 2015-20351

For small creatures such as we
the vastness is bearable only through love.

Carl Sagan

Contents

List of Figures

List of Tables

Chapter 1

Introduction

The trapped ion is a very unique system in many aspects. First, it is inherently isolated. The large charge-to-mass ratio implies that it cannot come into close contact with other charged particles with the same polarity, allowing us to isolate individual atomic ions using electromagnetic fields. This enables us to make use of their quantum coherence for an extended period of time.

The trapped ion is highly controllable at the same time. The tendency of its valence electron to couple strongly to visible light or RF fields enables precise manipulation of its various degrees of freedom including spin and motion. Also, the trapped ions are identical particles. Every single trapped ion of the same atomic number ever trapped has the same charge, mass and electronic structure. Of course, its interaction with background fields causes perturbation effects such as Stark shift and Zeeman shift, but for a subgroup of trapped ions with field-insensitive clock states, such effects can be made virtually negligible with the current technology.

In the last few decades, there has been monumental progress in the field of quantum computation. Owing to its long coherence time and high controllability, the trapped ion has been a major player in the field. In this chapter, I will give a broad overview of trapped ion quantum computer. Afterwards, I will talk about the entangled coherent state and its realization in our system.

1.1 Trapped Ion Quantum Computer

1.1.1 The trapped ion

In the context of quantum information experiment, the trapped ion is basically a quantum magnet suspended in a three-dimensional harmonic oscillator in ultra-high vacuum. Therefore, we are given a Hilbert space that is composed of its spin and motion in three orthogonal directions, or along its principal axes.

Even before the advent of modern lasers and precision optics, the two pioneers Hans Dehmelt and Wolfgang Paul [1, 2] invented devices that can trap charged particles including atomic ions. The more popular version of the device, named linear Paul trap after its inventor, uses four linear electrodes and two end cap electrodes that are positioned at the two ends of the device. One might think that applying DC voltages to the electrodes is enough to trap a charged particle three-dimensionally, but the fact that the Laplacian of an electrostatic potential is zero in free space ($\nabla^2 V = 0$, also known as Earnshaw's theorem) implies that this is impossible. The workaround to this problem first conceived by Wolfgang Paul is to use an oscillating potential that forms a stable confinement in one direction at one instant and in an orthogonal direction at another. Therefore in a Paul trap, an RF voltage is applied to the linear electrodes and it acts as a rotating transverse confinement field. The longitudinal confinement along the geometric axis of the trap can be provided by a static potential, which

is realized by the endcap electrodes.

A charged particle of mass m and charge e trapped by a potential of the form $U + V\cos\Omega t$ is subject to the following equation of motion called Mathieu equation:

$$\frac{d^2x_i}{d\tau^2} + a_i - 2q_i\cos 2\tau x_i = 0 \tag{1.1}$$

where x_i is the coordinate of the ion in the i-th axis, $\tau = \Omega t/2$, $a_i = \alpha_i eU/mr_0^2\Omega^2$ and $q_i = -\beta_i eV/mr_0^2\Omega^2$. r_0 is the distance from the ion to the electrode, and α_i and β_i are geometric factors derived from the shape of the electrodes. Depending on the values of a_i and q_i, the particle is either stably trapped or ejected from the trap. The diagram that shows the "regions of stability" is called the stability diagram, and an example is shown in Fig. 1.1(a). The ion is stably confined only when the parameters are in the shaded regions, and an ion trap should operate in a region where the ion is stable in every axis.

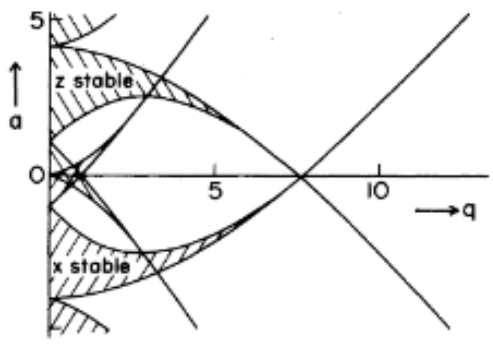

(a)

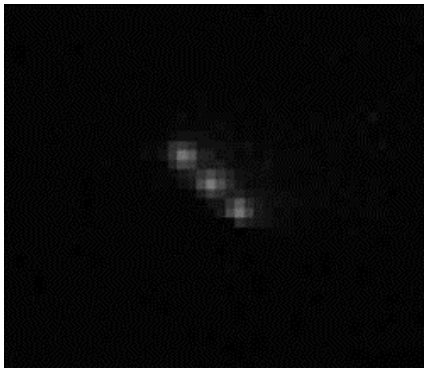

(b)

Figure 1.1: (a) An example of the stability diagram for Mathieu equation for a linear Paul trap [1]. (b) A chain of trapped ions. The ions are confined by DC potential along the direction of the chain, and by RF pseudopotential in the radial directions.

The motion of the ion following Eq. (1.1) is identical to that of a particle

trapped in a three-dimensional harmonic potential when averaged over a time much longer than $1/\Omega$, the period of the RF field oscillation.

1.1.2 $^{171}Yb^{+}$ qubit

There are many possible choices for the ion qubit, since metals with two valence electrons such as Be, Mg, Ca and Ba end up with a single valence electron after being first-ionized. Ytterbium, along with Calcium, is a very popular choice because it has magnetic field insensitive clock states and its transition frequencies can be addressed by well-developed and stable laser sources.

The electronic structure of $^{171}Yb^{+}$ is shown in Fig. 1.2. The Doppler cooling is realized by a 369.5nm laser beam that drives the transition between $\left|S_{1/2}, F=1, m_F=0\right\rangle$ and $\left|P_{1/2}, F=0\right\rangle$, with RF sidebands for repumping populations falling to the $\left|S_{1/2}, F=0\right\rangle$ state. There is a small branching ratio to the $\left|D_{3/2}\right\rangle$ state, and a 935nm laser beam is required to repump the population and close the cooling cycle. The qubit states are the ground hyperfine states, $|F=0, m_F=0\rangle$ and $|F=1, m_F=0\rangle$. These states are first order insensitive to magnetic field, but their separation varies quadratically to the applied magnetic field due to second order Zeeman shift. The control of the spin and motion is implemented by a pulse laser at 355 nm. The pulse laser generates a frequency comb, and we use its wide-bandwidth frequency components to drive Raman transition.

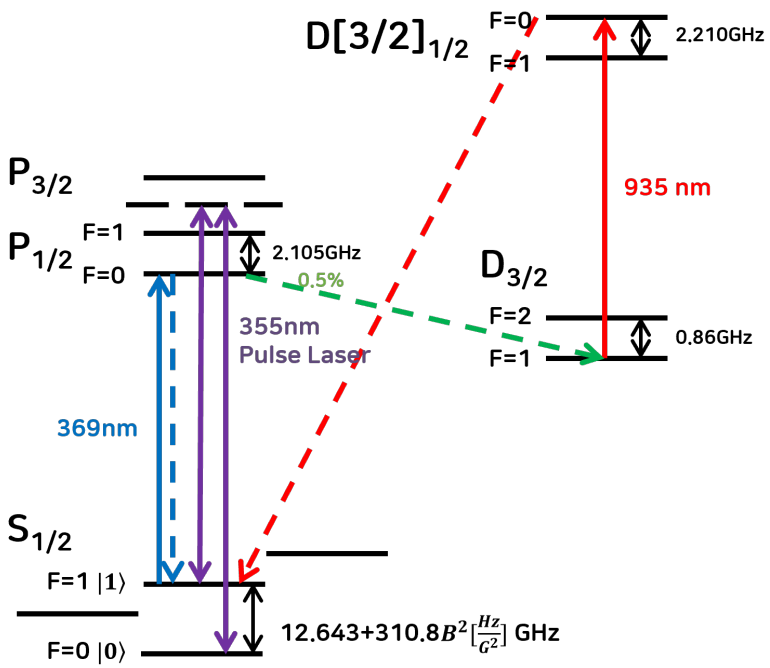

Figure 1.2: Electronic structure of the $^{171}Yb^{+}$ Ion. Solid lines represent transitions driven by lasers and dashed lines are spontaneous emission.

1.1.3 The quantum computer

First conceived by Yuri Manin and Richard Feynman [3], the quantum computer is the most natural solution to the problem of simulating many-body quantum systems. As the number of quantum particles in the system increases, the classical computer cannot keep up with the required amount of computation because the number of eigenstates of the system increases exponentially with the number of particles. Especially, in the last decade the exponential improvement of the computing power of classical systems have slowed down [4], implying that most quantum many-body systems may remain uncomputable. Therefore, a fundamentally new way of calculating the dynamics of the quantum system is needed, and the quantum computer deals with it by making the computation system itself quantum.

Quantum computing systems have been realized in many different physical platforms such as the trapped ion, superconducting circuit and photon [5, 6, 7, 8, 9, 10, 11]. One set of criteria for determining if a physical system is a good platform for quantum computing is the DiVincenzo criteria [12]. The relevant part of the criteria is as follows:

- The system has a well characterized and scalable two level system
- The qubit can be easily and effectively initialized
- The coherence time of the system is long enough
- A universal set of quantum operations can be implemented
- Each qubit's state can be measured separately

As of 2023, the trapped ion excels in every criterion except for the first one. In the trapped ion quantum computation system, state initialization is

achieved by optical pumping which is virtually perfect. Coherence times longer than an hour have been achieved [13]. Universal gate sets, such as the CNOT gate and single qubit rotations, have been realized with high fidelities [14, 15]. The quantum state of each qubit can be measured with negligible cross-talks by a number of means such as direct imaging of the ion chain and use of an array of photon counting devices [16, 17, 18, 19, 20, 21]. However, scalability, perhaps the most important of the criteria, remains an open problem. Trapping in a single ion trap hundreds of qubits does not work well for many reasons. There are various attempts to make the trapped ion system more scalable, such as photon interconnects and shuttling ions [22, 23, 24, 25].

Whether or not we will achieve true scalability in the near future is not clear and may even depend on the information-theoretic nature of the Universe [26]. However, it is likely that the efforts to realize scalable quantum computation will not stop, since it may be our only chance at computing large quantum many-body problems at the moment.

In this thesis, our attempts at constructing a quantum computing system that successfully demonstrates the components of a universal quantum computer is presented. We realized single qubit rotation with microwave and Raman transition and estimated its fidelity with randomized benchmarking. Also, we realized Molmer-Sorensen gates with a two-dimensional spin-dependent force and measured the fidelity. The results will be presented in later chapters.

1.2 Entangled coherent state

1.2.1 Theoretical interest

The coherent state is sometimes regarded the most classical quantum state because it is well localized and follows classical trajectory [27]. This makes the entangled coherent state is inherently interesting because it is the quantum entangled variant of the most classical state. Therefore, it has been the focus of much theoretical research efforts in the past few decades. Its quantum nauture can be used to probe the fundamenal aspects of quantum mechanics by studying Bell's inequality and Leggett's inequality [28, 29]. It has also been utilized in quantum metrological studies [30, 31]. The state has also been studied in the context of quantum computation and communication [32, 33, 34, 35, 36]. Also, there is a rising interest in encoded qubits, which utilize continuous variable states such as coherent states as logical qubit states. These states offer significant advantages in error detection and correction, and has been used in the first experimental implementation of error correction [37]. In trapped ion systems, similar experiments were carried out using GKP states [38]. In this context, the generation of entangled coherent states is very important, as it can be used as a building block for quantum computation with encoded qubits.

1.2.2 Realization

Despite the theoretical interests, the entangled coherent state had not been experimentally realized until 2009 when Ourjoumtsev et al. succeeded in entangling two cat states of light [39]. It was followed by Wang et al. who realized the same quantum state in microwave cavities coupled to a superconducting circuit [40, 41].

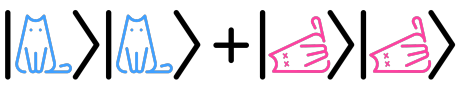

Figure 1.3: The entangled coherent state is a multimode and entangled version of the coherent state. Using the famous cat analogy, it can be understood as the entangled state of the two cats in two separate boxes. In braket notation, the two mode entangled even coherent state can be expressed as $1/\sqrt{2+2e^{-2(|\alpha|^2+|\beta|^2)}}(|\alpha\rangle\,|\beta\rangle+|-\alpha\rangle\,|-\beta\rangle)$(image courtesy of Wonhyeong Choi)

The motional degrees of freedom of the trapped ion system have been used to generate various non-classical states, such as single-mode cat states or NOON states [42, 43, 44]. However, the entangled coherent state has not been experimentally realized in ion traps so far. This thesis presents the first realization of the entangled coherent state in the trapped ion system. This is achieved by combining a two-dimensional spin-dependent force with projective measurement of spin. Details of the experiment will be discussed in the relevant chapters.

1.3 My life at SNU graduate school

My first and second years were mostly focused on course work because I did not have a working atomic ion trap setup. However that does not mean I did not spend any time in the lab. During these years, I worked with macroscopic quadrupole traps to trap micrometer sized dielectric particles and liquid

droplets. It was quite challenging and I sometimes felt completely lost because I did not have any seniors to help me, but at the same time it was extremely rewarding because I got to solve physics and engineering problems on my very own with limited human and material resources. Every time I succeeded in something, sometimes as trivial as generating a high voltage AC by backfeeding cheap transformers with a high power RF source(do not try this even at the lab), I felt a strong sense of achievement. I still remember the moment when I first trapped water droplets after shutting down the lab a couple of times and blowing up about a dozen transformers. Although this project ended without any publications, I think this experience helped me greatly for the rest of my PhD program because I learned how to solve problems on my own and how exciting it can be to get something to work after hours and days of failure.

At the end of my second year, I was sent to MIT to work with actual atomic ions at the Vuletic ion lab. It was in this lab where I learned most of my practical knowledge on atomic physics, both in theory and experiment. The two graduate students I worked with, Joon and Ian, have since been my good friends and teachers. They spent much time to teach me everything they know, and I believe I reciprocated by being a deligent and resourceful junior. The first project we embarked on after resurrecting the long-neglected ion trap setup was observing ions tunneling through a Prandtl-Tomlinson type potential formed by an optical lattice and the electrostatic potential of the surface trap. It was only after I went back to Korea after over a year of attempts that they decided that this experiment was not feasible with the current machine. The next project, which I was lucky to be able to participate when I returned, was measuring the isotope shifts of the narrow transitions of various even isotopes of ytterbium. This experiment was motivated by the idea that a certain type of hypothetical force carrier, heavy boson or dark photon as theorists call it,

might leave an imprint on the energy levels of atoms by altering isotope shifts in a special pattern, which is the consequence of the new particle mediating interaction between neutrons and electrons. I learned much from this project as well since we had to install and stabilize a new titanium-sapphire laser and introduce a new laser beam path for the probe beams.

When I first joined the current group in the summer of 2020 after switching my thesis advisor, I realized that I had to make my own setup almost from scratch because the only ion trap we had back then did not and still does not work very well due to charging-related issues. Thus, I started constructing a new system with a blade trap that was originally assembled at SKT. Luckily there were many talented and passionate students I could work with. We installed the vacuum chamber on February 1st 2021, and trapped our first $^{171}Yb^{+}$ a month after. We saw our first Raman transition and sideband cooling in July that year, and implemented spin-dependent force in the same year. After having to stop the experiment for a few months to install a new pulse laser, we successfully realized two-qubit gate with trapped ions for the first time in Korea in May of 2022. It was 16 months after installing the vacuum chamber. I think our progress was extremely fast, especially considering that none of us have done this before.

1.4 Outline of thesis

This thesis is composed of three parts. The first is the construction of the experimental setup. I will discuss the various subsystems that make up the setup, and explain the design philosophy and decisions that were made to ensure the stability and performance of the system.

The next is the basic characterization of the qubit and the implementation

and analysis of basic quantum gates that constitute a universal quantum gate set. I will discuss fundamentals of the trapped ion experiment, such as light-atom interaction, micromotion compensation, heating rate and coherence time measurements. This part will also include single qubit gate benchmark results, theoretical aspects of the Molemer-Sorensen gate and its implementation and characterization in our setup.

The third part is the experimental realization of entangled coherent states. It is implemented by utilizing the spin and motional degrees of freedom of the trapped ion. This is the first demonstration of the quantum state in a trapped ion system, and is confirmed by the observation the periodic modulation of its phonon state parity, a direct consequence of the entanglement of the two motional states. Together with the precise control of quantum states possible in the trapped ion system, this experiment will pave the way for interesting possibilities.

Finally, I will outline a path towards a five-qubit trapped ion system based on the current experimental setup. This includes an individual detection and addressing system that is designed to accommodate up to five qubits in the current setup.

Chapter 2

Experimental Setup

The field of trapped ion quantum information experiment has become as much of an engineering challenge as it is a physics experiment. The rapid progress of the field in the past couple of decades have set the bar quite high for "interesting" or "paper-worthy" experiments. It seems that the field is at a stage where commercially available solutions have not quite caught up with the requirements of the cutting-edge research. As a result, the researcher is required to be a good electrical, mechanical and software engineer as well as a good physicist.

Let us think about the prerequisites for a simple Molmer-Sorensen gate experiment. For the gate operation to be applied correctly, the following steps have to be taken flawlessly.

- The ions are trapped in a stable electrical potential, with an appropriate amount of stabilized bias magnetic field and minimal micromotion.

- They are Doppler cooled to hundreds of micro-Kelvins.
- They are sideband cooled to quantum ground state.
- A sequence of laser pulses with appropriate frequencies and amplitudes are applied to the ion chain for a predetermined amount of time, which is usually on the order of ~ 10 μs. The pulses should be phase-locked for coherent control of the wave function which is a prerequisite for quantum computation.

Imperfection at any stage will have detrimental effects on the fidelity or feasibility of the gate operation. For example, if the bias magnetic field is noisy, the coherence time of the ion qubits will be affected. Also, if the intensity of the pulse laser fluctuates, the accuracy of gate operations will suffer and sideband cooling may not work properly, resulting in a temperature that is higher than optimal. This will increase the sensitivity of the gate operation to imperfection in calibration, which will reduce gate fidelity. The situation becomes even more complicated because calibrating all the parameters used in the steps above, such as the frequency of the motional sidebands, the correct sideband cooling sequence and the correct gate operation parameters, takes time. Therefore, the system should be noise-less and stable at the same time so that the calibrated parameters do not drift away before useful operations can be performed. This makes the construction of the trapped ion quantum computer quite an engineering challenge that requires prowess in multiple disciplines. In this chapter, I will go over the various subsystems of the experimental setup, and examine their designs not only from the perspective of a physicist but also from that of an engineer.

2.1 Overview

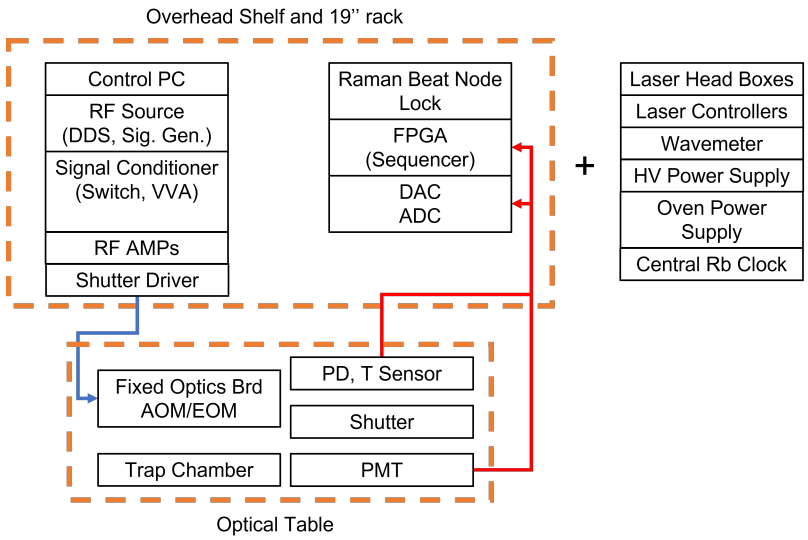

Figure 2.1: The setup can be considered as the collection of its subsystems. Only the optical system and the vacuum chamber is placed on the optical table, as heat and acoustic noise can affect the performance of the setup by introducing slow drifts and noises. The table itself is separated from its surroundings by an aluminum profile system and plastic walls. The modules in the optical system is again individually shielded by aluminum cases to protect them from the drift of the ambient temperature and to facilitate maintenance. Each module in the electrical system is encased in a metallic chassis.

The experimental setup can be broken down into subsystems as shown in Fig. 2.1. The subsystems are the optical system, electrical system, trap and vacuum chamber system, and the control software. The optical system and the vacuum chamber are situated on the optical table, which is shielded from its surroundings by a shelf system made of aluminum profiles and acrylic walls. The electrical system is isolated from the two, as there are cooling fans that produce acoustic noises and air currents which destabilize the beam paths and reduce phase coherence of the pulse laser beams. The setup is controlled by two PC's.

One is connected to the wavemeter and used to control the frequencies of the continuous-wave(CW) lasers, while the other controls everything else including the RF system and the experiment sequence controller. The home-built control program is resource-heavy and not very stable. Therefore the wavemeter is controlled by a separate computer because I did not want the CW lasers to drift away, heat up and eject the ion from the trap in case the main control computer has to be reset due to errors.

2.2 Optical systems

2.2.1 Continuous-wave lasers

As can be seen in Fig. 1.2, two CW lasers(369.5 nm and 935 nm) are required for the Doppler-cooling of the ion. In addition to this, we use another CW laser with the wavelength of 399 nm to excite the electron in the neutral Yb atomic beam. The electron is then excited again to the continuum by either the 355 nm pulse laser or the 369.5 nm laser for photoionization, which generates Yb^+ ions. We trap the qubit ion, $^{171}Yb^+$, by adjusting the frequencies of the CW lasers so that they are resonant only to the transitions of the particular isotope.

A schematic diagram of the beam paths is presented in Fig. 2.2. The 399 nm (ionizer) and 935 nm (repumper) beams enter the vacuum chamber from the lower left viewport(when the chamber is viewed from the imaging camera) after being combined by a shortpass dichroic mirror. The beams are focused before they enter the chamber. Due to the large difference in the wavelength, the spot diameter of the ionizer is about 100 μm, but the repumper is several times larger than that. This has no detectable effect on the experiment. The repumper has a 3.07 GHz sideband created by an electro-optic modulator(EOM) to address the hyperfine levels of the repumped level. To make the system as low-maintenance

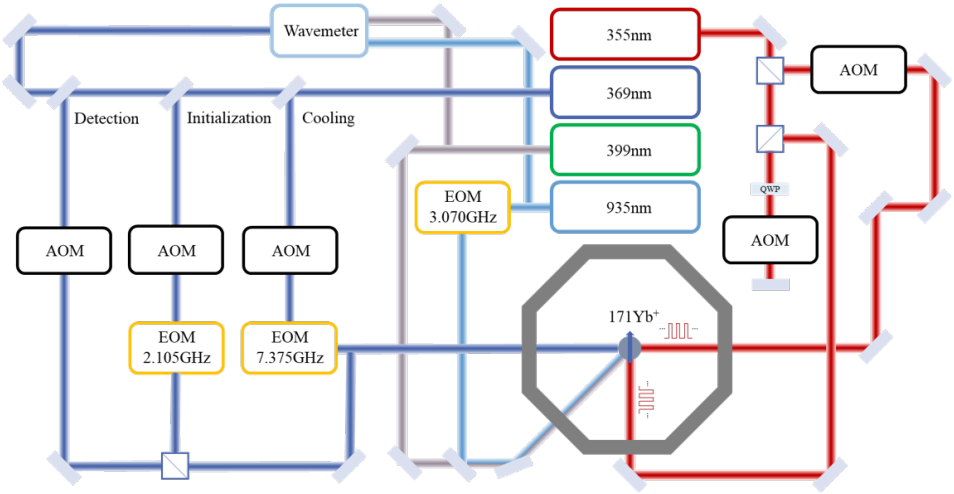

Figure 2.2: An overview of the beam paths viewed from the direction of the imaging system. The 369.5 nm beam paths, which includes three AOM's and two EOM's, are implemented by a watercooled fixed optical board for maximum stability. The 355 nm beam path, which is used for quantum state manipulation, is enclosed by aluminum walls to prevent air currents and thermal effect from affecting the phase coherence and pointing stability of the beams.

and stable as possible, the beam path between the 935 nm laser head and the output collimator next to the vacuum chamber is all fiber-connected. That is, the laser exits the laser head via a fiber coupled output port, which is split into two with 1:99 power ratio by a fiber beam splitter. The weaker beam goes to the wavemeter, and the stronger to a fiber EOM which produces the 3.07 GHz sideband. The output port of the EOM is then connected to the final output collimator. Also, the repumping laser is a distributed-feedback(DFB) laser and is controlled only by temperature and current, which further simplifies the system. As a result, it has needed little maintenance in the last two and half years. Fiberizing every component of the beam path, including the laser head, makes the system simple and robust.

Typically, the power of the ionizer is about 200 μW while the repumper is

2∼3 mW. A much lower power will be sufficient if the spot size is reduced by using a dedicated focusing lens. The ionizer can be shuttered off by a home-made shutter activated by a TTL signal from the main field-programmable-gate-array(FPGA) after a desired number of ions have been trapped.

The initial alignment between the beams were achieved by looking at the beams after they exit the chamber through the viewport on the opposite side. After making the beams overlap, we translate the focusing lens which is mounted on a two-dimensional translation stage. In this step, we first look for the scattering of the ionzier on the trap blades with the ion imaging CCD. The CCD should first be aligned to the center of the trap by positioning it to look at the middle point of the endcap electrodes. Afterwards we turn on the atomic oven and increase the current to a relatively high value and wait for a couple of minutes. If the ionizer is aligned correctly and set to the right frequency, a bright cloud of neutral Yb atoms should be visible at the center of the CCD image. The micrometer is now fine-tuned to situate the two beams at the center of the trap.

The CW laser central to the $^{171}Yb^{+}$ ion experiment is the 369.5 nm laser. It is responsible for the Doppler cooling of the ion and the initialization and detection of the qubit states. The cooling, initialization and detection beams are prepared in a breakout board that receives a fiber coupled 369.5 nm light and splits it into a number of beam paths. After passing through AOM's and EOM's, the beams are then fiber-coupled and sent to the output couplers located to the left of the chamber. In the cooling beam path, there is an acousto-optic modulator(AOM) driven at 160 MHz to switch the beam on and off. There is also an EOM driven at 7.375 GHz whose 2nd order sideband pumps out the population in the $|0\rangle = \left|S_{1/2}, F = 0, m_F = 0\right\rangle$ state to close the Doppler

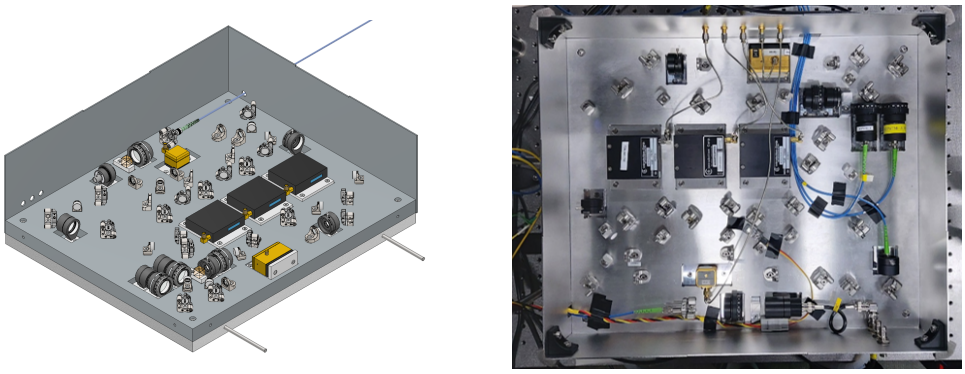

(a) (b)

Figure 2.3: (a) A CAD image of the breakout board. (b) A picture of the completed setup

cooling cycle. The initialization and the detection beams have perpendicular polarizations, although not optimal, and are coupled to the same polarization-maintaining(PM) fiber.

To control the detection and initialization beams, we use AOM's for each beam. The AOM is driven at 200 MHz, 40 MHz higher than the cooling beam AOM, because the Doppler cooling tends to work better with a few tens of MHz red-detuned(although theoretically the lowest Doppler cooling temperature is achieved at a detuning of half the linewidth of the cooling transition, which is 10 MHz), while the initialization and the detection beams are most efficient close to resonance. The frequency of the EOM used for initialization is 2.105 GHz. The cooling and Initialization-Detection beams are combined by a D-shaped mirror right before the focusing lens. The breakout board is a watercooled fixed optics setup which maximizes stability. The board is indeed one of the most stable parts of the setup and its internal optics do not need any maintenance as long as the chiller is operating properly. A picture of the breakout board is shown in Fig. 2.3(b).

For the 369.5 nm laser beams, the input fiber couplers are cost-efficient singlet aspherics because the quality of the lens does not have much effect on the coupling efficiency. However, the outgoing beams should be as Gaussian as possible to ensure that the beam profiles at the ion match the expected size and shape. The beam in the breakout board should be of high quality for the same reason. Thus for the output couplers we chose high quality triplets from Micro Laser Systems as shown in Table 2.1. There has been an issue with the optical fiber connecting the laser head module and the breakout board where the both ends of the fiber receive sudden optical damage, which results in reduced transmission and defocused beam profile. We have not quite figured out why this happens, but reducing the optical power going into the fiber seems to help. Initially we coupled about 2 mW of power into the fiber, and the fiber tips would last just over a month. Now we input less than 1 mW and the fiber stays intact for as long as six months. When the fiber tips are damaged, polishing them with a multi-step fiber polishing kit can restore them. We think it is a different issue from solarization, which results in a slow degradation of coupling efficiency and is also present in our system.

	Product Name	Vendor
Output coupler to chamber	FC-5	Micro Laser Systems
Output coupler to breakout board	FC-5	Micro Laser Systems
Cooling beam AOM	ASM-1702B8	Intraaction
Initialization beam AOM	ASM-2002B8	Intraaction
Detection beam AOM	ASM-2002B8	Intraaction
Cooling beam EOM	Model 4851	New Focus
Initialization beam EOM	Model 4435	New Focus
Focusing lens	PLCX-25.4-64.4-UV	CVI Optics

Table 2.1: A list of selected items in the CW laser beam paths

2.2.2 Pulse laser

The pulse laser is the main workhorse of the quantum part of the experiment. The CW lasers, while necessary for trapping and Doppler cooling the ion, are not involved in coherent operations. Thus, their optical phases do not matter because all we need is scattering photons off the ion. However, the phase of the pulse laser is directly imprinted on the quantum state of the qubit and needs to be controlled precisely. The situation is made more complicated by the fact that the Raman transition is realized by a Mach-Zehnder interferometer in which the two Raman beams follow different beam paths. This makes the phase of the Raman transition sensitive to the fluctuations in the beam paths in the scale of the laser wavelength. Therefore it is necessary to enclose the space between the pulse laser and the vacuum chamber, which we implemented by carefully designed overlapping aluminum walls. Other materials such as acrylic or laser blackout fabric were avoided because the strong pulse laser beams can ignite them. A picture of the enclosed beam path is shown in Fig. 2.4.

From here on, the two beam will be called the H(horizontal) beam and the V(vertical) beam. The V beam enters the chamber via the bottom viewport of the vacuum chamber as the name implies. This made the aligning process a nightmare because we could not see the beam exiting the chamber from the opposite side as it was blocked by the ion pump assembly. Nonetheless I found a way to align the beam reliably. The procedure is as follows. (1) Make sure that the vertical beam is parallel to the optical table surface and aligned to go through the point that is the projection of the center of the vacuum chamber. (2) Place a 45 ° fixed folding mirror that sends the beam upward through the center of the bottom viewport. This should be done carefully because if the folding mirror rotates slightly, the vertical beam will be directed at an angle to

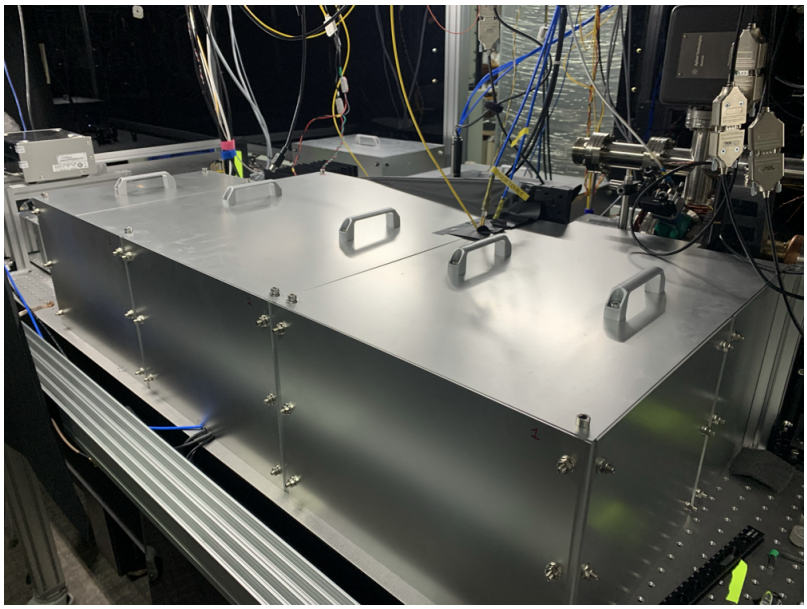

Figure 2.4: The pulse laser beam path is shielded off with aluminum walls. The walls are bolted to aluminum profiles, which are fixed on the optical table. The goal is to block air currents from affecting the laser phase, so the walls are designed to slightly overlap with each other to minimize gaps between them. About 80 % of the beam path is shielded. The rest could not be enclosed due to the difficulty of designing aluminum panels that fit the contours of the vacuum chamber. In addition to the aluminum walls, the beam path is protected by a secondary enclosure that covers all of the optical table as is usual in atomic physics setups.

the normal vector of the optical table which will give confusing results in the next steps. I recommend that the whole process be monitored by a properly aligned ion imaging CCD. If the beam is aligned to go through the center of the trap, the pulse laser will be scattered by the inner surface of the blades and a scattering pattern will emerge on the CCD image. (3) Scan the final focusing lens horizontally, so that the laser beam scans the trap horizontally or in a direction perpendicular to the trap axis. Since the gap between the neighboring blades is 460 μm, the scattering should virtually disappear while

the lens stage traverses the same distance assuming the focus of the beam is in the inner area of the trap. If this step produces unsatisfactory results such as very narrow or wide range of drastically reduced scattering, go back to step (2) and attempt to align the folding mirror again. (4) Place the beam on the left edge(lower value for the position of the translation stage) of the trap inner space, and scan the beam vertically. Within the scanning range, two bright spots with large scattering should be visible. Place the beam at the center of the two spots. A CCD image of the two spots are shown in Fig. 2.5. This will have a large uncertainty as the spots are quite large, but it does not matter because the neighboring area will be scanned thoroughly. (5) Scan the position of the focusing lens two-dimensionally with sufficiently large ranges and long probe time. While scanning, the vertical beam should be set to a frequency that can excite Raman transition, either via co-propagating qubit flopping or together with the H beam. Obviously, the co-propagating transition is the better option because it does not require the alignment of the H beam. If the system is capable of neither, one can try to detect Stark shift caused by the non-resonant high intensity beam, but it will be a much smaller signal and requires a well characterized microwave qubit transition [45]. The scan usually consists of about 1000 steps, and was done automatically by running a sequence with a fixed qubit transition time and setting as the scanned parameters the vertical and horizontal position of the lens. Once the beam is properly aligned, the thermal drift of the beam position over time is very small and the full 2D scan is rarely needed. It seems that this kind of continuous operation degrades the lubrication of the motorized stage quickly. If the motor is stuck, applying a small amount of grease restores movement.

We use a pulse laser to drive the transition between the qubit states because it is the best solution currently available for bridging the 12.6 GHz energy gap

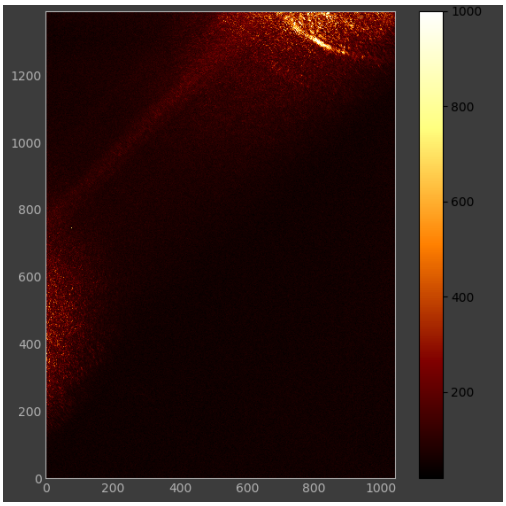

Figure 2.5: Image of the trap center acquired by a properly aligned CCD when the V beam roughly hits the center of the trap but is not precisely aligned. The trap axis goes from the lower left and upper right corners of the image. The diagonal bright line is one of the inner surfaces of the blade trap, illuminated by the V beam which is currently position to the left of the trap center. The two bright spots that can be used for the vertical alignment of the V beam are the two circular bright patches along the upper diagonal line. The vertical center of the 2D scanning range is set to be the average vertical coordinate of the two spots. The horizontal is found by finding the horizontal range with little to no scattering, which corresponds to the gap between the blades.

between the qubit states. It is a microwave frequency, so a coherent microwave oscillating at 12.6 GHz is able to drive the transition between the $|1\rangle$ and $|0\rangle$ states. However, the microwave cannot be focused tightly to individually address single ions in an ion chain. Its coupling with the motional mode is also very small because of the small momentum of the microwave photon. These problems have successfully been overcome by using large near-field magnetic field gradients, but they require precisely engineered microwave antennae that should be integrated in the trap itself [46, 47, 48]. If we use non-counter propagating laser beams, we can solve both of these problems as they can be tightly

focused down to $\sim 1\mu$m and impart large momenta on the ion. This scheme requires the phase coherence of the two laser beams. It does not necessitate the use of frequency combs, but phase-locking two laser beams that oscillate at frequencies that are 12.6 GHz apart is not an easy task, and any imperfection in the process would compromise the quality of qubit control. One could use an EOM to produce a phase-locked sideband to the laser and drive Raman transition with it. However, for $^{171}Yb^{+}$, the large qubit transition frequency implies that the sidebands would not be very strong [49, 50]. On the other hand, the 355nm pulse laser is an off-the-shelf solution to all of the problems mentioned so far. It even has the extra benefit of being at the magic wavelength that cancels the differential stark shift between the qubit states [51, 52].

To drive the qubit transition with frequency combs, the qubit frequency should be a multiple of the comb spacing, which is usually not the case. Therefore, we give a differential offset to the combs in each leg of the interferometer by driving the respective AOM's at different frequencies. Also, The repetition rate of the pulse laser changes over time due to the thermal and acoustic perturbations to the laser cavity. There are two ways to compensate for this: feedback and feedforward. In the feedback method, one modulates the position of a movable mirror inside the laser cavity in a fashion that counters the repetition rate drift measured by a high-speed photodetector. We used this method in the early stages of the experiment when we worked with Mira HP-D because it was supplied with a control port for that purpose. However Paladin, the new pulse laser, does not support repetition rate modulation, so we had to switch to the feedforward method. In this method, the differential offset of the combs is modulated to cancel the repetition rate drift. The rate of the drift is not straightforward to measure, and should be downconverted by a stable RF source. Our scheme is similar to Ref. [53] and uses digital PID control. Details of the digital control

and RF circuit are presented in Section 2.3.1.

The feedforward frequency is applied to the V beam by changing the RF frequency driving the AOM. It usually changes at a rate of $\sim$ 1000 Hz/s, and introduces slight deflections in the beam path. Its approximate size can be calculated as follows: $\Delta d = L\Delta\theta$ where L is the length of the beam path downstream and $\Delta\theta$ is the deflection angle of the beam which can be calculated using the driving frequency, wavelength and the speed of sound in the AOM. The estimated size of beam translation at the position of the ion is in the range of 10 $\sim$ 100 nm, which is close to the scale of the laser wavelength and enough to compromise phase coherence. We have experimentally confirmed that the phase coherence is affected by a poorly designed feedforward system. Therefore, we built the V beam AOM in double-pass configuration which cancels out the effect of the spatial dithering of the laser beam.

A schematic diagram of the Mach-Zehnder interferometer is shown in Fig. 2.7. While the V beam is used to compensate for the repetition rate drift, the frequency of the H beam is set to predetermined values to address different transitions, such as the red and blue sidebands. A delay stage in the H beam path can change the beam path length by as much as 20 cm. It is calibrated to equalize the length of the two legs of the interferometer so that the H and V beam pulses arrive at the ion at the same moment. The typical power in each beam at the end of the beam path is between 100 and 200 mW. The diameter of the horizontal beam is about 13 μm while the vertical beam is 17 μm * 37 μm, longer in the direction of the trap axis. The vertical beam is intentionally made asymmetric to help Rabi frequency balancing between the two ions in an ion chain. The beam sizes were measured by scanning the laser stages while driving Rabi oscillation with a fixed probe time.

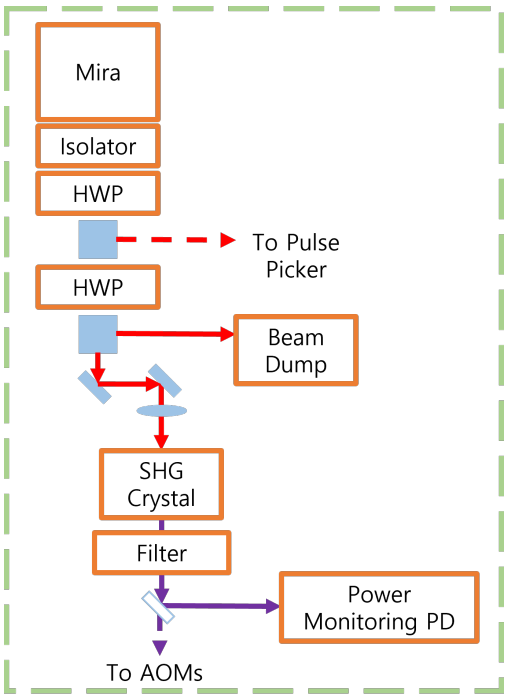

Figure 2.6: Beam path for the second-harmonic-generation(SHG) process used in the Mira setup. It is no longer in use but included for reference.

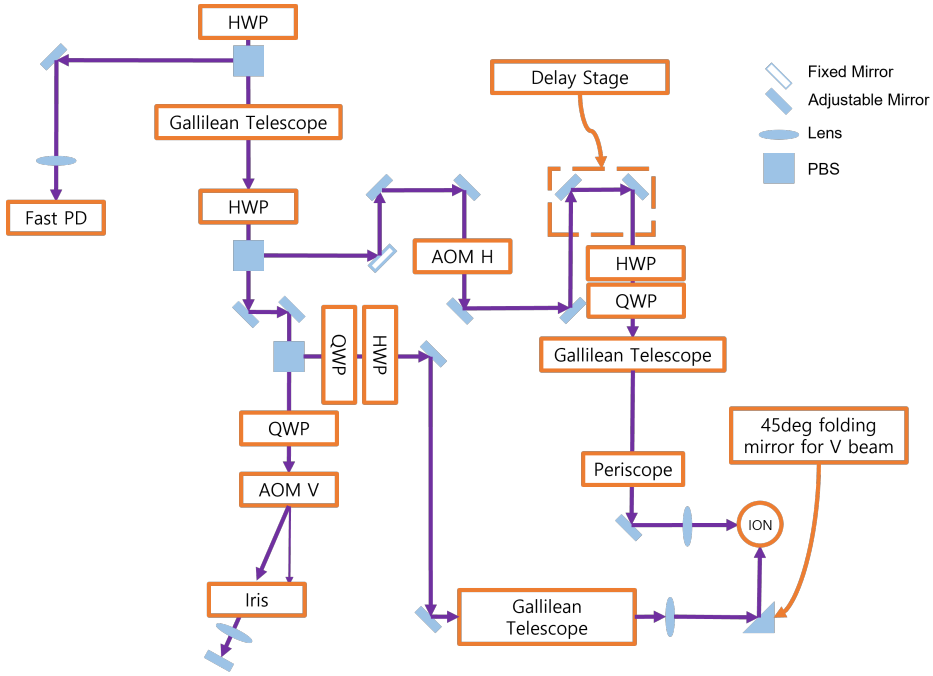

Figure 2.7: Beam path for the V and H beams. The V beam is controlled by a double-pass AOM(AOM V) whose RF frequency is updated at a rate of ~ 50 kHz to compensate for the change in the repetition rate. The H beam is modulated by a single pass AOM(AOM H). The RF drive for AOM H is set to predetermined values during experimental sequences to address different transitions for qubit and motional control. Both beams go through beam expanders and are focused down to appropriate sizes at the position of the ion. The delay stage in the H beam path fine-tunes the path length, so that the H and V pulses arrive at the ion at the same moment.

2.2.3 Imaging system

The imaging system is composed of an imaging lens (M1), CCD, and a PMT (photo-multiplier tube). The CCD is used to check on the condition of the trapped ion chain (number of trapped ions, positions of the ions) and to help with laser beam alignment by observing how the laser beams scatter off the trap electrodes. The PMT is used for actual experiment by counting photons and making a photon number histogram, which is used to infer the quantum state of the qubits. While many other setups use a complex array of lenses for imaging, we use a simple doublet system where the image of the ion is simply transferred from the object plane to the image plane with a certain magnification factor. M1 consists of a 2" aspheric lens(67-273, Edmund Optics) on the ion-side and a 2" plano-convex lens(LA4782, Thorlabs) on the other side. The magnification factor is simply the ratio of their focal lengths, and the nominal magnification is $500mm/60.0mm = 8.33$.

Both the PMT and CCD are equipped with IR block filters and bandpass filters that pass 370nm to increase signal-to-noise ratio. The PMT also has a pinhole to reject ambient light. In addition to this, the whole imaging system is encased in a blackout box. These steps are necessary because even in the bright state, $|1\rangle$, on average only 20 photons are collected by the PMT per millisecond. Even a small background count can ruin the detection fidelity.

2.3 Electrical system

Most of the modules in the electrical system of the setup, along with many pieces of equipment in other systems, are designed following the 19" rack mount standard. This is a natural choice because most scientific, computing and network instruments, ranging from laser controllers and power supplies to ethernet routers are designed to be mountable in 19" racks. Therefore the electrical modules built following the 19" standard can be stacked on top of each other or other instruments. Also, they can be mounted in commercially available server racks, which comes with many accessories that make life in the lab easier, such as cable guides, cooling fans and sliding shelves. Table 2.2 lists all the modules in the electrical system of our setup. Most modules are contained in its own 19" enclosure and the rest are planned to be modularized.

Name	Function
Qubit frequency reference	Drives MW horn and downconverts repetition rate signal
FPGA+DAC	TTL's needed for experimental sequence. Analog voltages to control instruments
DDS1	RF frequencies for AOM's in CW beam paths
RAMAN A	RF frequency generator for Raman AOM's
RAMAN B	Repetition rate stabilization RF circuit. Upto four RF frequencies for Raman AOM's
RF Switches A	6 low-frequency RF switches, 2 high-frequency RF switches and 2 VVA for RF power control
RF Switches B	5 low-frequency RF switches for Raman AOM frequency switching
RF Amps	Amplifies DDS RF signals to drive AOM's
Trap PID system	PID for trap RF power

Table 2.2: A list of modules in electrical system

2.3.1 RF sources for qubit control

Qubit state engineering requires an electromagnetic field that oscillates at or slightly detuned from the transition frequency of the qubit. The coherence of the qubit operation requires both the qubit frequency and the field frequency to be stable, as any noise in either would result in intractable time evolution, which means decoherence. Here, we will discuss the design of the field control system that produces coherent RF signals to modulate the laser and microwave radiation to control the qubit state of the trapped ion.

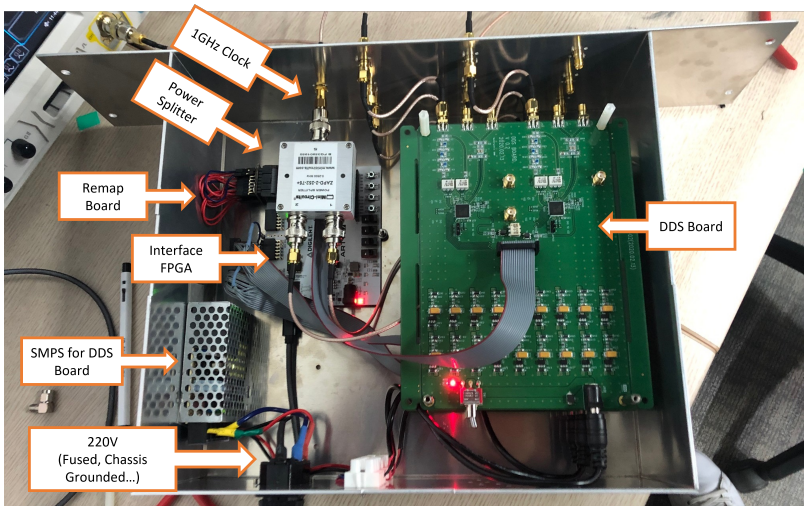

Figure 2.8: Inisde of DDS1 module. Three DDS boards each containing two RF generation chips are stacked on top of each other. They are powered by a 5V SMPS. The clock signal for the boards is supplied by an RF connector in the front panel. It is fed to a three-way splitter and goes to each board.

Let us take a look at DDS1 as an exemplary design of the electrical module. This module contains three PCB's each of which contains two RF generation chips (AD9912, Analog) that can produce RF frequencies up to 400 MHz with power in the $-10 \sim +5$ dBm range. Therefore, this module is designed to produce six RF frequencies that can be used to drive AOM's and other devices

after amplification. The boards communicate with the control computer with an FPGA(Arty-S7, Xilinx) running a custom program as the interface. We needed a remap board that maps the output pins of the FPGA to those of the DDS board. The chassis is grounded and the mains connector contains a fuse for safety. All the electrical connections were meticulously covered and mechanically fixed to guarantee robustness and prevent any accidents. We also made sure that proper components, such as lugs, wires and connectors with the right sizes were used. Also we avoided direct soldering as much as possible and used commercial solutions such as euroconnectors and Wago connectors since the mechanical strength and quality of soldered joints vary greatly depending on the quality of equipment and soldering skills. All three boards share a clock signal, which originates from a central Rb clock and is distributed within the module via a three-way splitter. This is very important because the control fields should be phase-locked in order to apply multiple gates in sequence.

The next module worth examining is the FPGA+DAC module. As the name implies, this module contains the main FPGA which produces precisely timed TTL signals used in experiments and a DAC board (DAC8734, TI) that outputs clean DC signals. The TTL's turn on and off the RF switches used in the experiment. The minimum time resolution of the signals is 10 ns, but is intentionally limited to 100 ns on the software side for consistent operation. The DC signals are used to set the reference voltage for trap RF power stabilization and provide the offset voltage for the RF blades. Some are used to control the power of the lasers via VVA's.

Raman B contains the repetition rate stabilization circuit for the pulse laser. The repetition is about 120.1 MHz, and we use the interference between the 1st and the 107th teeth of the frequency comb to drive Raman transition.

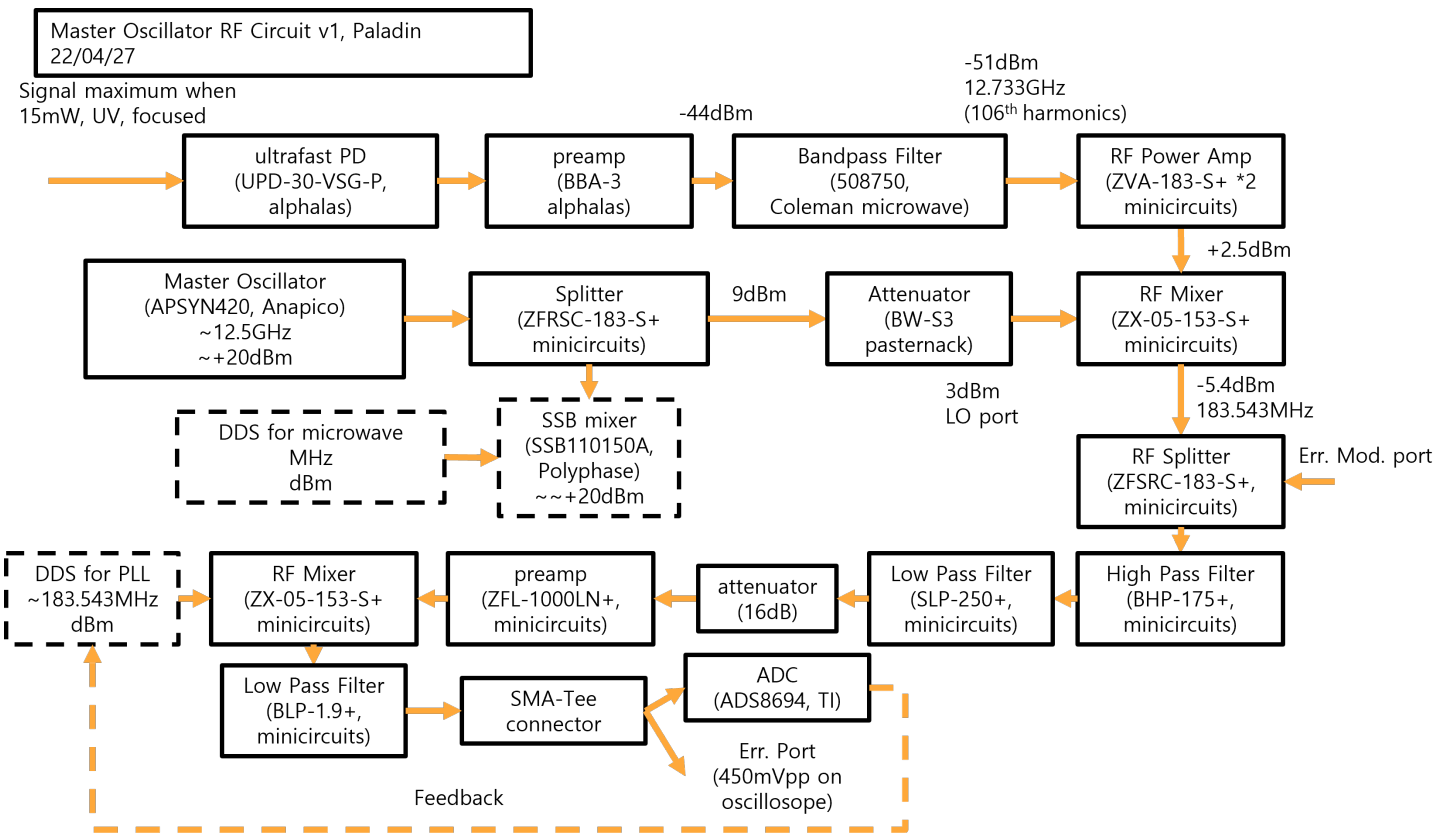

Figure 2.9: The RF circuit for measuring and compensating repetition rate drift.

A 1 Hz change in repetition rate corresponds to 107 Hz in terms of Raman transition. Therefore, the error gain of the PID system should be sufficiently high. If it only measured the drift of the fundamental signal which oscillates at 120.1 MHz, its gain or signal to noise ratio would have to be excellent since the quantum operation is about two orders of magnitude more sensitive to the drift. Some groups [20] use the 32nd harmonics of the intensity variation observed by the photodetector. This is probably because the bandwidth of the RF circuit is limited and it is easier to implement division by $32 = 2^5$ which is a simple bit shift operation in the FPGA. We measure the 106th harmonics of the photodetector signal and use it for repetition rate stabilization because the bandwidth of our circuit allows for it and our PID operation is fast enough to accommodate division operation. The details of hardware coding for the FPGA was delegated to J. Kang. Using the 106th harmonics has the advantage of increased error gain, which enables a longer coherence time.

A diagram of the RF circuit is shown in Fig. 2.9. The ultrafast photodetector signal is filtered and amplified so that only the 106th harmonics of the pulsed signal passes. It is then mixed with the reference oscillator, which is detuned by about 100 MHz from the qubit transition. Only the lower sideband is within the bandwidth of the circuit, thus this step effectively downconverts the signal. The signal is then summed with external error modulation signal, which only exists for diagnostic purposes. The signal is then mixed with a repetition rate tracking signal which is updated by the FPGA at a rate of 50 kHz. The mixed signal is fed to an ADC. The FPGA implements a PID circuit which modulates the frequency of the tracking DDS so that the voltage detected by the ADC stays at zero.

The above process can be summarized as a digital frequency following or

phase-locked-loop(PLL) circuit for the repetition rate of the pulse laser. This circuit has been realized using analog circuits as shown in Ref. [54]. The digital system is much more flexible and scalable because the numerical value of the measured repetition rate is stored in the memory of the FPGA. The value is then used to calculate the frequencies required for various transitions. Indeed, Raman B is capable of outputting four RF frequencies that can be used to drive AOM's, and the system is capable of updating all four RF frequencies simultaneously at a rate of $\sim$ 50 KHz. This number is limited by the number of DDS boards in the system, and can be increased by adding more boards, although this will decrease the update rate. An analog system would have needed four separate PLL's to achieve the same result.

A potential caveat to be careful of when using digital PLL system is the precision of floating point operations. Initially, we coded the system such that the system updates the RF frequencies in an additive manner. It calculated the difference between the previous repetition rate and the current one, and added a small correction to the outgoing RF frequencies. This resulted in the accumulation of errors in the floating point operations in every cycle. The error in each operation is negligible, but when they compound at a rate of 50 kHz, the deviation of the calculated RF frequencies becomes significant after a few minutes. This problem hindered our progress for a few weeks. It was eventually fixed by changing the code to simply recalculate the outgoing frequencies instead of calculating the required correction factor.

2.3.2 DC voltage system

The trap needs several DC voltage sources to operate properly. It needs two radial compensation voltages that translate the position of the DC null in the

radial directions. It also needs a DC offset for the RF blades in order to change the separation of the two radial modes and tilt the principal axes. Lastly, it needs a voltage for the endcaps. The electric fields generated by these DC voltages directly interact with the atomic ion. Therefore, the motion of the ion is extremely sensitive to the condition of the applied voltages. Any noise or RF pickup will be a source of decoherence. We designed the lowpass circuit presented in Fig. 2.10 to reduce noise and RF pickup in DC electrodes. It is a simple circuit, but has very peculiar requirements, so it was not easy to design it properly. The circuit should have the following qualities: (1) strong suppression of non-DC components, (2) very good rejection of $\sim$ 10 MHz RF signals because the DC electrodes are only a few millimeters apart from the RF blade, (3) operational voltages up to a few kV which is required for micromotion compensation and sufficiently strong axial confinement. There are a handful number of capacitors that satisfy all of these requirements, with some of them being discontinued in the near future. We used 2220Y2K00104KXTWS3 and 222521K00122JQTAF9LM from Knowles Syfer as the first and second stage capacitors. The expected low-pass cutoff frequency is 15.9 Hz.

Finding the right capacitor is not the only issue. The routes and pads have to be round and separated as much as possible to prevent arcing. The PCB itself can also cause problems as the high-voltage DC can short following the surface of the printed circuit board. This is well known in the electrical engineering community and called surface creepage. Interestingly, this effect has to be considered when designing a surface trap for trapped ion experiments to avoid shorting or arcing between the microfabricated electrodes [55]. The surface creepage is currently the limiting factor of our DC electrode voltages. There are potential benefits of higher endcap voltage, but the current version of the low-pass filter shorts out at around 2000 V after about an hour probably

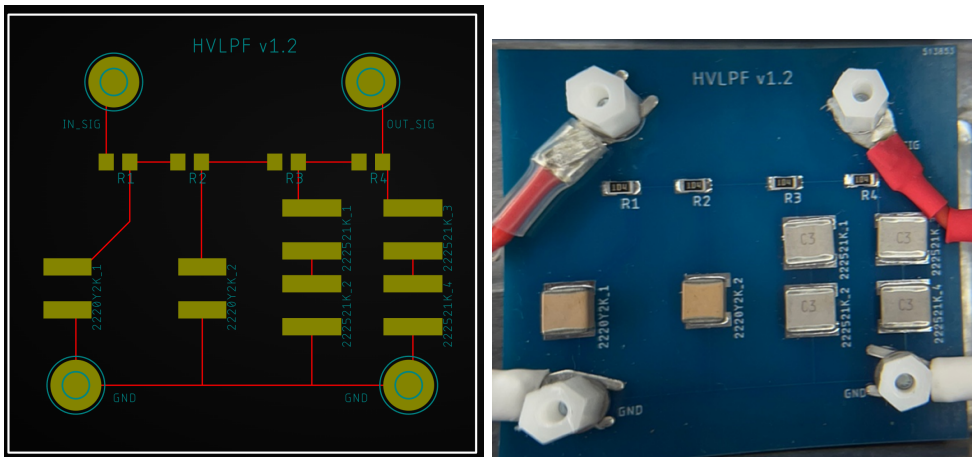

(a) (b)

Figure 2.10: (a) Schematic of the low-pass filter. (b) Picture of the actual circuit.

due to surface creepage. We tried sonicating the surface of the PCB because surface contaminants are known to exacerbate this effect, but there was no improvement. We settled on a maximum of 1300 V for the endcap to be on the safe side.

2.3.3 RF voltage system for trapping potential

We put much effort in stabilizing the RF trapping potential because it is utilized in the coherent control of motion which is necessary for non-classical motion generation and Molmer-Sorensen gate. We actively stabilize the amplitude of the trapping RF voltage. It is measured by a capacitive divider located on the inner surface of the helical resonator which is the small blue PCB in Fig. 2.11(a). The divider samples about 1/30 of the voltage, which is then rectified by a diode circuit. The voltage is reduced by another factor of 30 when rectified [56, 57]. The resulting DC voltage is an indicator of the amplitude of the RF voltage through PID control. It is then stabilized by an analog PID controller to a

reference voltage coming from the FPGA+DAC module. One can try to control the RF amplitude by directly controlling the RF source using such functions as amplitude modulation which is available in any function generator. However, its bandwidth depends on the internal circuitry of the function generator, which is usually not optimized for speed. Another option is to use a VVA, but this has the risk of introducing additional noise to the system because most VVA's require a power source. The amount of attenuation depends on the supply voltage, making the output vulnerable to power source noise. Therefore, we modulate the RF amplitude with an RF mixer. When the DC control voltage is applied to one of the input ports, it effectively becomes a wide-bandwidth RF amplitude controller [58].

Currently, the coherence time of the quantum motion of the ion is $4 \sim 5$ ms. For high fidelity entangling gates and precise control and analysis of non-classical motion, it needs to be increased. There is actually a large room for improvement because much longer coherence times have been reported in a similar setup [14]. The signal to noise ratio of the PID error signal is about 1000/2 mV, with the majority of the noise coming from 60 Hz ground loops. Better electrical isolation and higher error gain can improve the sensitivity of the PID control and improve the coherence time of the trap.

The long term stability of the RF amplitude is also crucial for ion trap experiments because drift of calibrated secular frequency deteriorates the quality of quantum state control. Despite best efforts, the secular frequency drifts at a rate of approximately 1 kHz/hr at worst. The rate of drift tends to be higher when there are more people in the lab and is lowest at night. It is most likely due to the thermal drift of the components that constitute the RF amplitude compensation system. The worst offender is likely to be the RF power sampling

and rectifying system, as the capacitors used in them have bad temperature ratings. Future systems should use C0G ceramic capacitors whose temperature coefficient is zero. The stability of the reference voltage should also be considered. The output of DAC's are known to be susceptible to temperature changes. It can be improved by using temperature controlled DAC modules such as LMP2066 from Texas Instruments.

We float the main coil of the helical resonator using a pi-filter, which is basically a bias-Tee as shown in Fig. 2.11(b). This is because a DC offset to the RF electrodes can be used to tune the spacing between the radial modes by breaking the symmetry of the trapping field. We chose to add the DC offset directly to the RF voltage by using the pi-filter since the ground blades are directly connected to the electrical ground inside the vacuum chamber and cannot be controlled from outside.

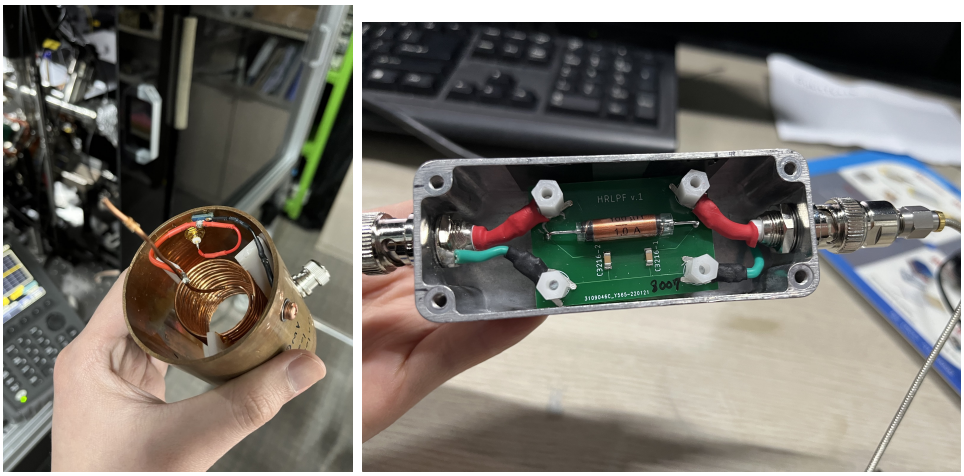

(a) (b)

Figure 2.11: (a) The RF voltage at the end of the main coil is sampled by a capacitive divider, which is the tiny blue PCB in the picture. The output of the divider goes to the SMA connector next to it and then is rectified by a rectifying circuit connected to the helical resonator on the outside. (b) The pi-filter consists of a high frequency inductor between two capacitors. It works as a symmetric bias-tee, and enables us to apply DC offset to the RF electrodes. It is on the ground side of the coil, and therefore not subject to the high voltage RF which is formed at the end of the main coil.

2.4 Trap and vacuum chamber

2.4.1 Blade trap

Our trap assembly follows the blade trap geometry first conceived by Rainer Blatt's group at University of Innsbruck [59]. Its electrodes are tapered towards the center of the trap to increase the field strength, which results in a tighter confinement for the ion. The trap geometry is shown in Fig. 2.12 and Fig. 2.13.

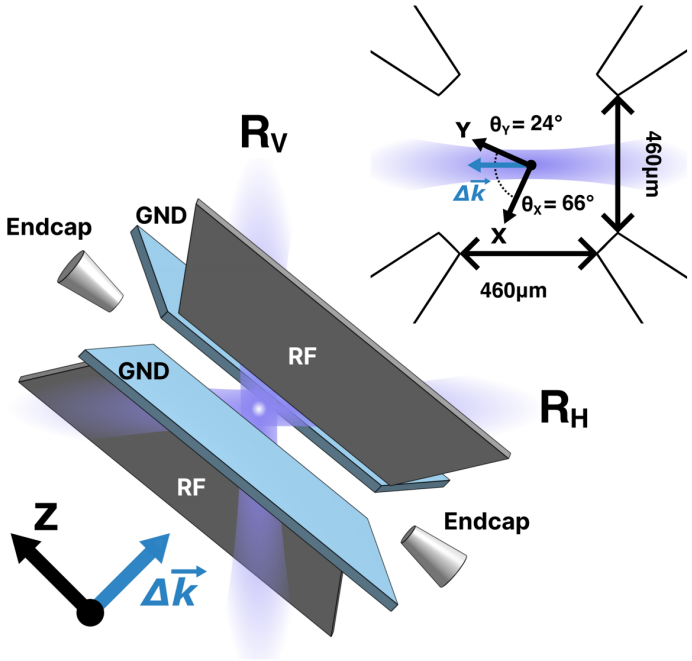

Figure 2.12: (Upper right) transversal cross section of the trap (Bottom Left) The trap electrodes and the direction of the pulse laser beams [60].

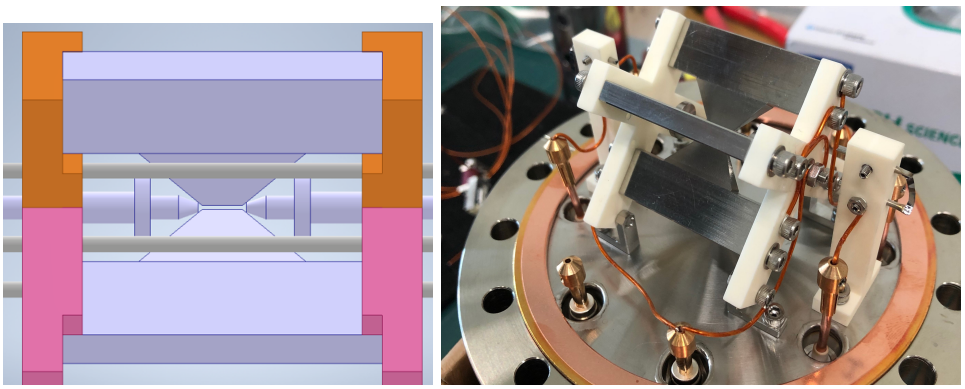

(a) (b)

Figure 2.13: (a) A CAD image of the trap assembly. The trap is viewed from the backside flange(hidden) to which it is mounted. Gray cylindrical rods are the compensation rods, and the pair of electrodes on the left and right with a disk shaped feature in the middle are the endcap electrodes. The distance between them is 6.0 mm. The colored parts are MACOR blade holders. (b) A picture of the actual trap assembly before being installed in the vacuum chamber. The ovens are installed in the ceramic pillars on the left and right. Atom beams emitted from the ovens enter the holes in the endcap electrodes and reach the trap center.

In the transverse plane, the distance between neighboring electrodes is 460 μm and electrode-to-ion distance is 325 μm. The shortest distance between the endcap electrodes is 6 mm, which has been a major obstacle in multi-ion operations. The resulting axial confinement is too weak, leading to a weak coulomb interaction between the trapped ions. In most of the experiments presented in this thesis, the endcap electrodes were kept at 1300 V, and the axial secular frequency was $(2\pi)120$ kHz. At $(2\pi)1.2$ MHz of radial secular frequency, the transverse cm and tilt modes were only 6 kHz apart which forced us to use both modes simultaneously.

2.4.2 Vacuum chamber

The trap assembly and the vacuum chamber were built by Dr. Kwon at SKT. Not much information about the trap and chamber is available to us apart from a CAD file from which I was able to find the trap dimensions. The vacuum chamber consists of 3.75" viewports, electrical feedthroughs for DC and RF voltage supply, and a large recessed viewport for imaging. The DC voltages for the DC electrodes are supplied via SHV connectors which are rated for 5000 V and 5 A, although we have not used voltages higher than 2 kV because breakdown and arcing might occur within the vacuum chamber or the DC low-pass filters.

The ground electrodes are directly connected to the chamber ground within the vacuum chamber. This is a sub-optimal design as it forces us to use the RF blades for both the DC offset and RF voltage. The wires connecting the DC electrodes and the SHV feedthroughs are neither shielded nor equipped with bypass capacitors. It may have contributed to the erratic behavior of the micromotion where the DC voltage required for compensation increases almost

linearly with the secular frequency. We were eventually able to suppress the micromotion sideband to about 1/10 of the carrier transition, but the DC electrode connections are poorly designed and should be improved in the next iteration of the blade trap setup.

The RF electrodes are connected to the signal pin of one of the SHV connectors in the backside flange. It can be improved as well since we have to somehow connect the main coil of the helical resonator to the SHV connector. I had to make an intermediate connector for this purpose by soldering thick copper wires to the exterior and signal pin of an SHV connector. It required significant crafting skills because the voltage carrying copper wire would short out when too close to the SHV connector or the grounded wire. I had to cut out a sizable portion of the connector to prevent shorting and wasted about a dozen of them before making a functioning one. I also designed and installed a shield for the area between the SHV connector and the helical resonator because the design of the feedthrough exposes the two tips of the main coil. A picture of the helical resonator and the neighboring area is shown in Fig. 2.15(a). The Q factor and resonance frequency of the helical resonator are measured by a spectrum analyzer which feeds the circuit with RF signals of varying frequencies and measures the reflected signal. The Q factor is 176 and resonance frequency is 15.0 MHz. The resonance frequency may change slightly when a strong RF power is applied due to thermal effects and should be fine-tuned in-situ in actual experimental conditions. The resonator actually heats up noticeably after applying a few watts of RF power for a few minutes.

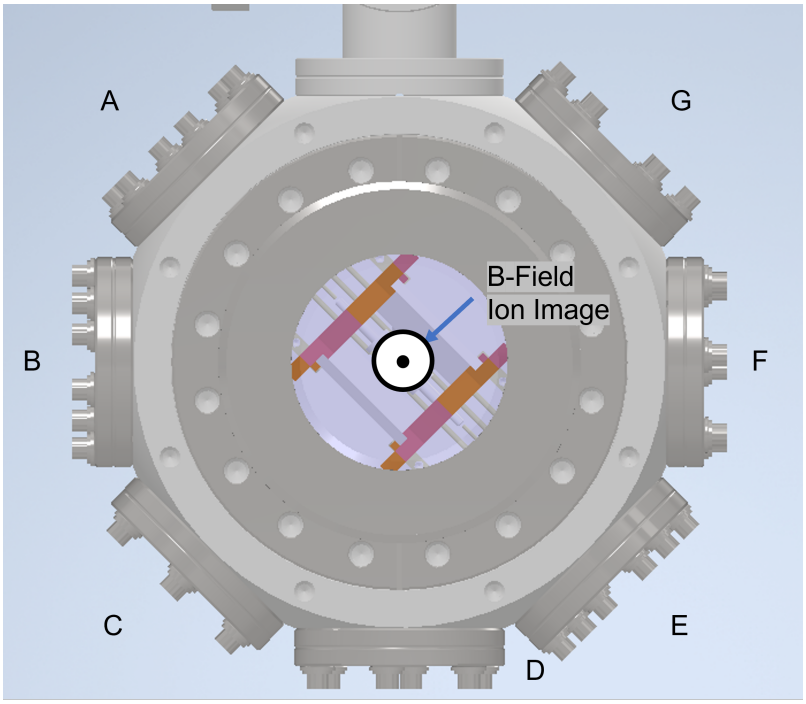

Figure 2.14: The vacuum chamber is viewed from direction of the imaging lens(hidden). The bias B field and ion imaging direction is out of the page. The ion pump is connected to the top of the image. Ports A and E cannot be used because they are blocked by the trap holders. Port G is used for Microwave Antenna, while D and F are used for the pulse laser beams. Through B enters the 369.5 nm beams(cooling, initialization and detection). C is for the repumper and ionizer beams. The compensation coils are installed on A and G, and the main coil for the bias B-field is wound around the recessed viewport(imaging viewport)

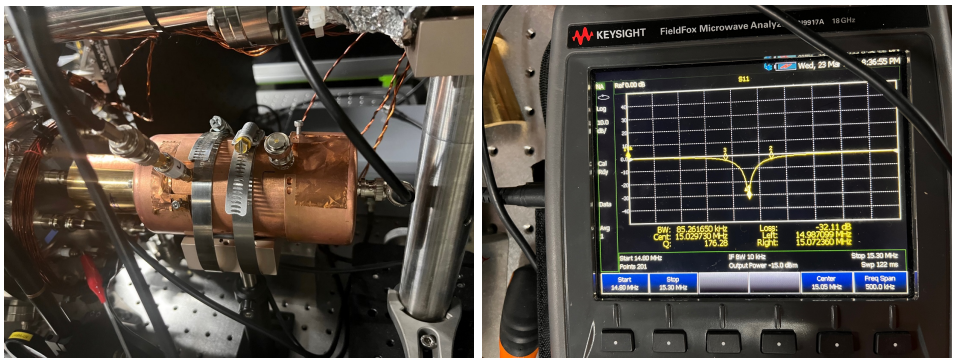

(a) (b)

Figure 2.15: (a) The helical resonator is connected to the vacuum chamber via an SHV connector in the backside flange. The area in between is shielded. (b) The resonance frequency and quality factor of the helical resonator.

Due to the lack of documentation, we had not known which of the 2.75" viewports had AR coatings until we tested them out. The diagonal viewports(A, C, E and G in Fig. 2.14) are not AR coated, and reflect 370 nm and 399 nm strongly. We initially tried to use C for the initialization and detection beam, but could not because the reflection from G was too strong and made its way to the PMT, which greatly reduced the signal to noise ratio of photon counting. Currently C is used for the repumper and the ionizer. The ionizer is also strongly reflected by viewport G, but the atomic beam fluorescence can still be imaged when an EMCCD is used.

2.5 Control software

The experimental control system was virtually non-existent when I first joined the lab, so I had to develop it from scratch. There was a crude system for running experimental sequences based on a custom python wrapper for the custom FPGA program. However, it was not very intuitive and too much of basic FPGA operations was left to the end user, making the system very complicated. Luckily, I was able to muster a small crew of talented and passionate students with background in computer science, and the development of the new control program progressed very quickly once I decided on the requirements and basic structure. The details and design patterns of the control program pertaining to software engineering were decided with the help of Hoon Hur and Jiyong Kang, whose expertise in software development has been invaluable.

Its design is inspired by the custom control program for the Vuletić trapped ion lab which was written in C# and various sub-GUI's were integrated in a single program using tabs. Our new control program was built using Python, an obvious choice considering its versatility, wide range of existent libraries and ease of use. It was designed with the following principles.

- Modularity: The program, although it appears to be a single program, is actually a collection of several programs. Each program can be modified, added and removed separately. They are only held together by the main control program which enables communication between each module.

- Simplicity: We hid information irrelevant to the end user as much as possible. This is especially true for the experimental sequencer. There are many steps that can be specified by the user, such as the number of FPGA clock cycles required to realize a branching operation. We decided

that controlling all these steps offered little advantage while making the sequencer GUI excessively complicated. Therefore we chose to limit the minimum time resolution of the experimental sequence to 100 ns, although the hard-coded minimum time step of the FPGA program is 10 ns. During the 100 ns, every extra operation such as resetting the TTL signals and branching operations are taken care of. We made sure we simplified the GUI in a consistent and knowable way so that the sequencer would not behave in unexpected and mysterious ways.

- Reliability: We tried to make the system as fool-proof as possible. This means that the peripherals such as the RF sources and the motorized stages operated strictly within given parameters. Fool-proofing is needed as the end user can physically damage the setup simply by sending the wrong commend. For example, they can destroy the RF amplifier for the trap RF by setting the output amplitude of the RF source to a value that exceeds the damage threshold of the amplifier. Although it is physically protected by an RF attenuator installed before the amp, we also protect it by limiting the output of the RF source on the software side. This is realized in multiple layers including the API that controls the RF source and the GUI used for setting its parameters.

- Connectedness: One of the reasons why we integrated the various modules in a single GUI was because the communication between them was essential in the experiments. Almost all of our experiments can be understood as scanning certain parameters of the system and observing its response which in our case is the number of photons scattered by the ions. Therefore, subsystems such as the RF sources, motorized stages, AOM's and the PMT have to be controlled simultaneously.

The modules in the control program can be summarized as follows.

- Experimental Sequencer: This module allows the user to compose experimental sequences by using a time table which specifies the duration and TTL output pattern in each of the subsection of the experimental sequence. It can also repeat subsets of the sequence and scan various experimental parameters such as DDS frequencies by communicating with the other modules of the control program.

- Data Reader: It displays the photon counting result of the experiment with some postprocessing. It can be configured to show the total photon counts, average photon counts in each shot of the experiment, or the qubit state of the ion calculated from the threshold method. It can also show two qubit populations using histogram fitting when the basis histograms are provided. Basic analysis of the data such as fitting to a sinusoidal function is also possible with in the GUI.

- RF Source Controllers: RF sources such as the DDS and signal generators can be controlled with the GUI. This is the first module that was developed in an object-oriented manner, where the various types of RF sources were implemented as classes. Their instances are created when the control program loads configuration files which contain device information such as RF amplitude, frequency, phase and limits for these values. This module is also the first to be designed in client-server architecture. The server retains all information on the current state of the RF controllers regardless of whether the GUI is running or not. The GUI communicates as a client with the server via TCP/IP protocol, and merely acts as an interface to retrieve and control the parameters stored in the server. It was an attempt at separating the GUI from the actual control system,

which is the recommended design pattern for instrument control systems. It has worked flawlessly and we intend to redesign every module in client-server architecture. We expect the next iteration of the control system to replace the current one in the next few months.

- Others: The other modules include the motorized stage controller and the Raman transition controller. They have been essential in the calibration of the Molmer-Sorensen gate because it requires a precise and reliable control of the beam position and frequency. The photon correlation measurement module has also been integrated into the control program, although it is no longer used since we now measure the size of the micromotion sideband to detect micromotion.

Development of the control software, although it seems trivial, is just as important as that of other systems such as optics. In a sense, it can be the limiting factor for the capabilities of the experimental setup because the ability to run certain experimental sequences quickly increases the amount of information that can be gained in a given time. In other words, it defines the speed at which we characterize the setup. As an example, when we first observed the time evolution of the spin-dependent force, it was very difficult to get a reproducible result because the trap frequency was not stabilized and the detuning for the force drifted quite quickly. We were only able to understand the situation correctly after seeing the ion's frequency domain response by using a "zipped scan" of the red and blue sideband frequencies in which they were scanned as a list of paired variables.

The control program will only become more important as we move on from two qubits to more qubits. We will have to run more complicated and longer sequences, and calibrate the system more frequently because there are more

normal modes and more types of entangling gates that have to be performed. As a consequence, running complex quantum circuits will almost certainly require a periodic recalibration system, which keeps track of and stabilizes the normal mode frequencies, adjusts the position of the laser beams and measure the qubit frequencies of the ion qubits. Doing all this manually with a five qubit system will take too much time.

Along these lines, a network of sensors that monitor the environmental parameters can be beneficial for the stability of the system. Such a system has already been implemented in a Bose-Einstein condensate setup [61]. In this paper, the authors were able to significantly reduce the atom number fluctuation in the quantum gas sample by identifying its correlation with the variation in environmental parameters and applying control loops to reduce it. A similar system for our setup which monitors such variables as the temperatures of the instruments, magnetic field, laser power and pointing stability, and photon counts can be used to improve the stability and characterization of the setup.

The current control program certainly has its limits, and we intend to move on to a new system that addresses them. This will include a unified client-server architecture for all modules, and a complete redesign of the sequence generator based on the ARTIQ hardware [62].

Chapter 3

Basic Ion Manipulation and Qubit Characterization

The fact that we can control individual atoms in ways that preserve their fragile quantumness still amazes me. It is in part enabled by the modern electrical and optical engineering introduced in the previous chapter, but it is also made possible by the theory of electromagnetism and quantum mechanics. In this chapter, I will introduce some of the basic concepts in trapped ion physics. The interaction between light and atom will be discussed, and topics specific to the trapped ion such as micromotion, motional heating and coherence will be presented together with relevant experimental results.

3.1 Cooling

Trapping requires not only a confining potential but also a dissipative force. For trapped ions, it is usually provided by lasers. The first tool we use to reduce

the temperature of the ion is Doppler cooling. Deriving its name from Doppler effect, it can be understood as a sort of feedback system based on velocity-dependent scattering of photons. It is realized by a laser that is nearly resonant and slightly red detuned from an atomic transition. When the atom moves towards the laser, the frequency of the laser is increased in the frame of the atom due to Doppler effect, which results in increased scattering and loss of momentum as shown in Eq. (3.1) where $\delta = \omega - \omega_0 + kv$ is the Doppler shifted detuning between the laser and the atom, Ω is the Rabi frequency and Γ is the linewidth of the transition [63].

$$R_s = \frac{\Gamma}{2} \frac{\Omega^2/2}{\delta^2 + \Omega^2/2 + \Gamma^2/4} \tag{3.1}$$

Conversely, the scattering rate decreases when the atom moves away from the laser. These two effects reduce the temperature of the atom to a level that is proportional to the linewidth of the transition, which defines the sensitivity of the velocity-dependent photon scattering. This temperature is called the Doppler limit and defined as $T_d = \hbar\Gamma/2k_b$ where k_b is the Boltzmann constant. This limit is achieved when $\delta = \Gamma/2$. A plot of T_d as a function of the detuning for $^{171}Yb^+$ is shown in Fig. 3.1. In this case, the optimal detuning is about -10 MHz, and the corresponding temperature is $\sim$500 μK. This is equivalent to about 9 phonons in a trap whose secular frequency is $(2\pi)1.2$ MHz.

In other atomic physics setups such as magneto-optical traps, the cooling beams come from all three directions. However, only a single beam is usually sufficient in a trapped ion experiment because the confinement is provided solely by the electric potential of the electrodes and the laser beam is only used for dissipation.

When we initially trap ions, we do not set the detuning at half the linewidth,

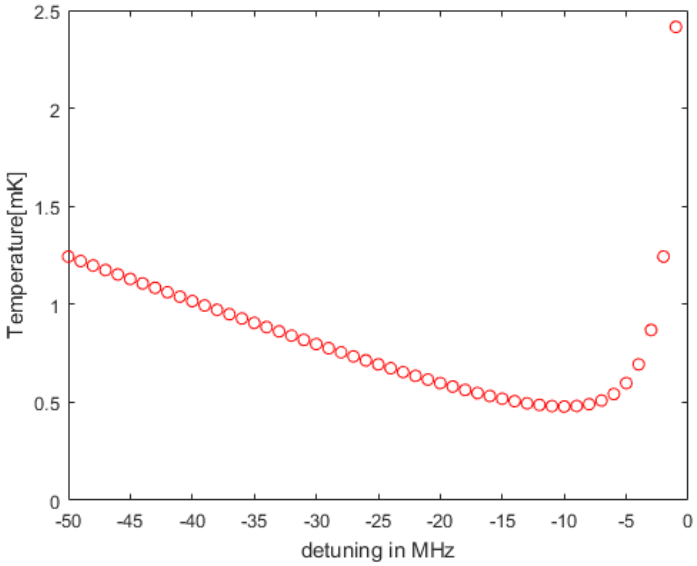

Figure 3.1: The lowest temperature is achieved at half the linewidth, which is about -10 MHz. When the detuning becomes positive, the laser heats up the ion.

which gives us the lowest equilibrium temperature. Instead, we detune it by at least -100 MHz. This is because the initial speed of the atoms in the atom beam is hundreds of meters per second, and at this speed the Doppler shift is significant, meaning that the cooling beam may actually be blue-shifted so much that it heats up the ion or barely interact with it. Either way the ion is not cooled down, and we experimentally determined that about -100 MHz of detuning cools down the ions efficiently and yields high trapping rates. After the ion is trapped and sufficiently cooled, we change the detuning to a value closer to resonance. The exact detuning does not affect the experiment because ground state cooling is achieved by sideband cooling anyway and the Doppler limit temperature does not strongly depend on the detuning.

The next step is the resolved sideband cooling, which is achieved by using

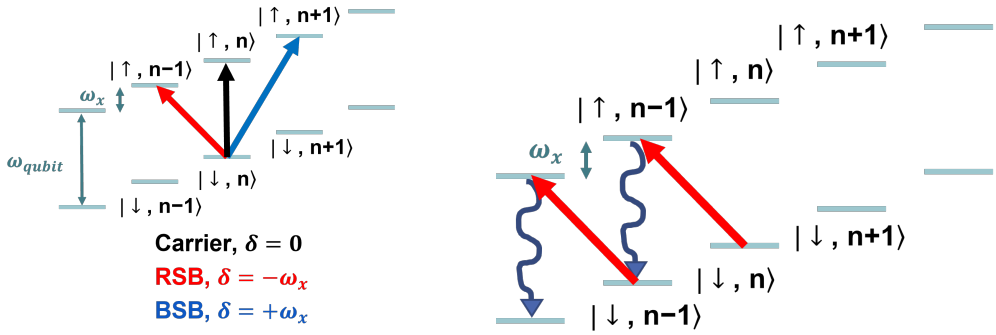

Figure 3.2: (a) Schematic diagram of various transitions for an ion qubit trapped in a harmonic potential with secular frequency ω_x. Carrier transition flips qubit state without affecting motion, RSB(red sideband) transition subtracts a phonon from the motion and BSB(blue sideband) adds one to the motion. (b) Resolved sideband cooling works by removing one or more phonons by a RSB π pulse, initializing the spin state and repeating these two steps until the ion reaches the dark state which is the motional ground state.

the pulse laser. Taking advantage of the narrow linewidth of Raman transition, we can resolve motional sidebands. That is, we can selectively drive Rabi oscillations where the laser field exchanges with the motion of the ion a chosen number of phonons. Some of them are shown in Fig. 3.2(a). These transitions form the basis of trapped ion motion control, but we will focus on the first red sideband transition which we use for ground state cooling.

The Rabi frequency for transitions involving phonon exchange is given by the Fock state representation of the motional part of the laser field, which is as follows [64]:

$$\Omega_{n',n} = \Omega_0 |\left\langle n' \right| e^{i\eta(\hat{a}^\dagger + \hat{a})} \left| n \right\rangle| = \Omega_0 e^{-\eta^2/2} \eta^{|n'-n|} \sqrt{\frac{n_<!}{n_>!}} L_{n_<}^{|n'-n|}(\eta^2) \tag{3.2}$$

where Ω_0 is the carrier transition Rabi frequency and η is the Lamb-Dicke factor defined as $\eta = \sqrt{\omega_{recoil}/\omega_{trap}}$. $n_<(n_>)$ is the smaller(larger) of n' and n, and $L_{n_<}^{|n'-n|}(\eta^2)$ is the associated Laguerre polynomial. Due to the $\eta^{|n'-n|}$ term, transitions involving change of phonons are exponentially suppressed as the number of exchanged phonons is increased.

An illustration of the sideband cooling process is shown in Fig. 3.2(b). In the first step, an RSB π pulse is applied, which extracts one phonon from the motion. The initialization beam returns the qubit state to $|\downarrow\rangle$ to close the cooling cycle. This process is repeated multiple times, about 50 times in our setup, before the motion is cooled to the ground state. It sounds straight forward, but the dynamics of sideband cooling is made complicated by the fact that the RSB Rabi frequency changes as a function of phonon number as shown in Eq. (3.2) and graphically represented in Fig. 3.3(a). This means that the optimal π time of the RSB pulse changes as the ion's temperature is lowered, and for some n's, the transition is prohibited due to the zero crossing of the associated Laguerre function. This is usually not an issue because the zero crossing occurs at $100 < n$ for the range of Lamb-Dicke factors used in trapped ion quantum information experiments. The cooling process we currently use consists of three sets of 1st order RSB pulses with different durations. We settled with it by trial and error but we note that the cooling sequence can be optimized numerically as done in [65].

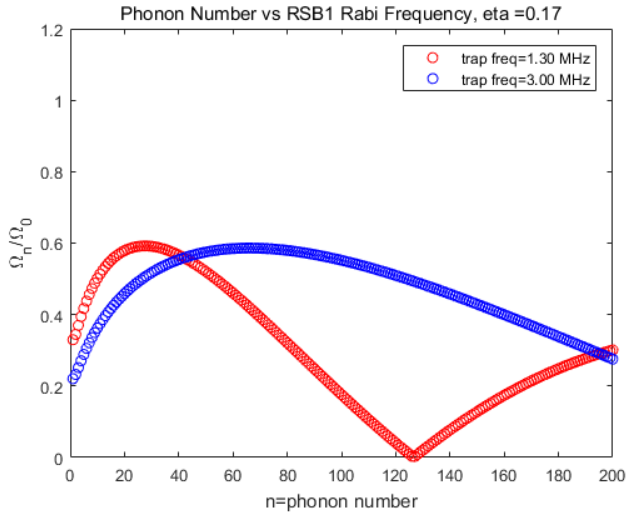

(a)

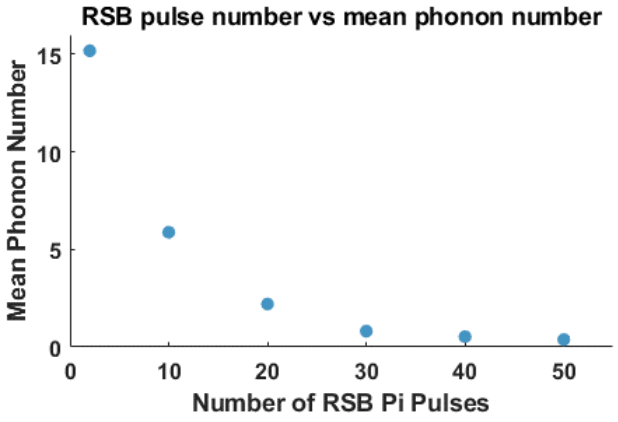

(b)

Figure 3.3: (a) First red sideband Rabi frequency($n' = n - 1$) as a function of the initial phonon number. The red curve assumes a secular frequency of 1.3 MHz and matches our setup. In this case, the red sideband transition is prohibited for $n = 125$. (b) Experimentally measured mean phonon number of a motional mode of the ion as a function of applied cooling pulses.

3.2 Ion manipulation with pulse saser

As mentioned in the previous chapter, the 355 nm pulse laser is a simple solution to the problem of individually controlling the $^{171}Yb^{+}$ ion. It can be tightly focused, bridges the qubit energy gap in a coherent manner, and has the extra benefit of being at the magic wavelength where the differential stark shift between the qubit states is minimized.

For most purposes, the interaction between the ion and the frequency comb formed by the pulse laser is almost identical to that between the ion and a pair of monochromatic CW laser beams whose frequency differences equal the Raman detuning. A detailed semi-classical analysis of the interaction is presented in [66]. Here, we will focus on the its conceptual understanding.

3.2.1 Understanding the frequency comb picture

In the frequency space, the pulse laser forms a frequency comb whose teeth are separated by the repetition rate, ω_{rep}. When the qubit frequency is an integer multiple of ω_{rep}, we can drive the qubit transition simply by irradiating the ion with the pulse laser because the required frequencies are already present in the comb. However this is rarely the case since we cannot continuously tune ω_{rep}. It is also not desirable because even a very weak scattered beam can affect the qubit state. Therefore, ω_{rep} is chosen such that $\omega_{qubit} \simeq (N + 1/2 \pm 1/4)\omega_{rep}$ to prevent single comb qubit transition.

We make another copy of the comb by using a beam splitter and control their frequencies separately with AOM's in their respective beam paths, which enables us to set an arbitrary Raman detuning between them. The scheme is illustrated in Fig. 3.4. From here we will assume that the ion absorbs a photon

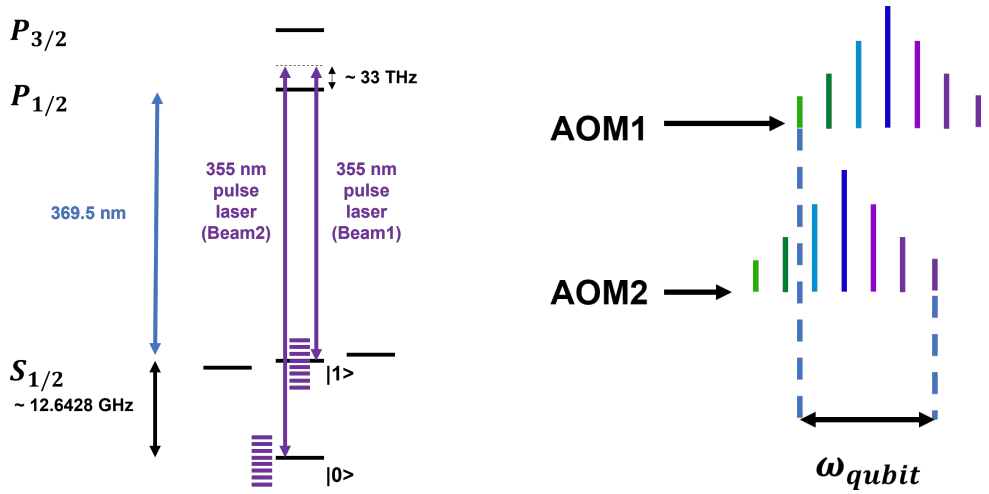

(a) (b)

Figure 3.4: (a) The virtual state used in the Raman transition is +33 THz detuned from the $\left|P_{1/2}\right\rangle$ state and -66 THz from the $\left|P_{3/2}\right\rangle$ state. (b) A continuous tuning of the Raman detuning is enabled by splitting the frequency comb into two and adding differential frequency offsets to them.

from Beam 2(controlled by AOM2) and emits one to Beam 1(controlled by AOM1). The offset frequencies required for the qubit transition can be found as follows:

$$\omega_{qubit} = N\omega_{rep} + \omega_2 - \omega_1 \tag{3.3}$$

where $\omega_{2(1)}$ is the frequency shift from AOM2(1). Our job now is to find the solution of the variables we can control (N, ω_1, ω_2) that satisfy Eq. (3.3). There are multiple solutions as shown in Fig. 3.5. An appropriate solution is chosen based on factors such as the resonance frequency of the AOM's and possibility of exciting other transitions such as micromotion and Zeeman sidebands. In most of our experiments, we use the comb spacing $N = 107$. In this configuration, the ion absorbs a photon from a doublepass AOM and emits energy to the beam

controlled by a single pass AOM. This means that the momentum transfer vector is defined as $\Delta\vec{k} = \Delta\vec{k}_{double} - \Delta\vec{k}_{single}$. We can do the opposite and flip the sign of the vector if we choose to use $N = 104$, but we use $N = 107$ because the required AOM frequencies are closer to the resonance of the AOM's, which is 200.0 MHz. When realizing spin-dependent force, we drive the red and blue sideband transitions simultaneously with the same comb spacing and this realizes a "phase-sensitive" configuration [49]. However, one can drive the red and the blue sidebands with different comb spacings and the opposite momentum vectors. In this case, the total momentum transfer for the spin-dependent force is nearly zero and the transition becomes 'phase-insensitive', which means that the phase of the force is insensitive to the phase fluctuation of the Raman beams [49]. This distinction becomes important when we implement an actual quantum circuit in which the phase of the spin-dependent force or the Bell state resulting from Molmer-Sorensen gate is important. In the phase-sensitive scheme, the phase of the Bell state is sensitive to the beam path fluctuation and has to be measured relative to the phase-sensitive $\pi/2$ gate. In the phase-insensitive case, the phase of the Bell state is not affected by the beam path fluctuation and can be measured by microwave $\pi/2$ gates because the microwave field phase is not affected by air currents or acoustic noises due to its long wavelength.

3.2.2 Control of spin and motion

We have the following Hamiltonian for a trapped ion in a one-dimensional harmonic oscillator with a secular frequency ω_x and subject to a pair of Raman beams with frequency $\omega_{0,1}$ and phase $\phi_{0,1}$ [64]:

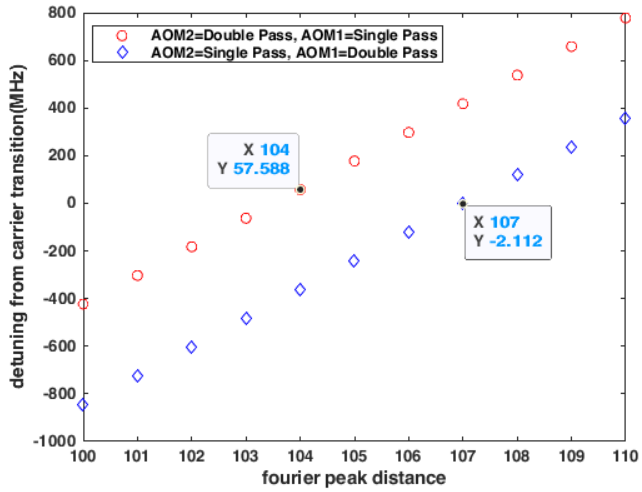

Figure 3.5: Raman detuning from the qubit transition for various comb spacings. For the red circles, $\omega_{rep} = 120.1MHz, \omega_1 = 190.0MHz, \omega_2 = 400.0MHz$, and the comb spacing we use is $N = 104$. For the blue diamonds, $\omega_{rep} = 120.1MHz, \omega_1 = 400.0MHz, \omega_2 = 190.0MHz$, and the comb spacing we use is $N = 107$. The Raman detunings can be made zero by tuning the AOM frequencies.

$$\begin{aligned} \hat{H} &= \hbar\omega_{qubit}\frac{\hat{\sigma}_z}{2} + \hbar\omega_X(\hat{a}_X^\dagger\hat{a}_X + \frac{1}{2}) \\ &+\frac{\hbar}{2}\Omega_0(|e\rangle\langle 0| + |0\rangle\langle e|)e^{i(k\hat{x}-\omega_0 t+\phi_0)} + \frac{\hbar}{2}\Omega_1(|e\rangle\langle 0| + |0\rangle\langle e|)e^{i(k\hat{x}-\omega_1 t+\phi_1)} \end{aligned} \tag{3.4}$$

In the interaction picture, the effective Hamiltonian becomes:

$$\hat{H} = \frac{\hbar}{2}\Omega\hat{\sigma}_+(e^{i\eta_X(\hat{a}_X^\dagger e^{i\omega_X t}+\hat{a}_X e^{-i\omega_X t})})e^{-i\delta t} + h.c. \tag{3.5}$$

where $\eta_X = kx_0 = k\sqrt{\hbar/(2m\omega_X)}$ is the Lamb-Dicke factor, Ω is Raman transition Rabi frequency, $\delta = \omega_L - \omega_{qubit}$ and ω_L is the frequency of the Raman beams defined as the frequency difference between the comb teeth of interest

in each arm of the Mach-Zehnder interferometer.

In the Lamb-Dicke limit where $\eta_X < 1$, Eq. (3.5) can be linearized as follows:

$$\hat{H} = \frac{\hbar}{2}\Omega\hat{\sigma}_+(1 + i\eta_X(\hat{a}_X^\dagger e^{i\omega_X t} + \hat{a}_X e^{-i\omega_X t}))e^{-i\delta t} + h.c. \tag{3.6}$$

It can be seen from Eq. (3.6) that when $\delta = 0$, that is when the Raman detuning is set to be resonant with the qubit transition, the transition between the two qubit states is driven. When $\delta = \omega_X$, the Raman beams drive the blue sideband ($\hat{H}_b \sim \hat{\sigma}_+\hat{a}^\dagger$) transition and when $\delta = -\omega_X$, the red sideband ($\hat{H}_b \sim \hat{\sigma}_+\hat{a}$) transition. The blue sideband transition flips the spin from down to up, while adding a single phonon to the motional mode. The red sideband does the same to the spin but subtracts a phonon from the quantum motion. We note that it is possible to drive higher order transitions with detunings that are multiples of the trap frequency. These transitions are regularly used by researchers for sideband cooling or to realize quantum states of motion such as the squeezed state. We stop at the first order transitions because in the experiments presented in this thesis we do not use these second order transitions, although they can be readily used in our setup.

3.3 Micromotion

Micromotion is an inevitable consequence of the dynamic nature of the Paul trap. It is basically a driven motion of the trapped ion that is caused by the oscillating trapping field. Mathematically, the motion of the ion in a harmonic potential with secular frequency ω and RF trapping field frequency Ω_{RF} can be expressed as follows [67]:

$$u(t) = (u_0 + u_1 \cos\omega t(1 + \frac{q}{2}\cos\Omega_{RF}t)) \tag{3.7}$$

In the above equation, u_0 is the difference between the stable point of the pseudopotential and that of the total electric potential that additionally takes into account the DC potentials. u_1 is the amplitude of the secular motion which is a function of temperature. q is the q-parameter in Eq. (1.1). The part that oscillates at $\omega \pm \Omega_{RF}$ is called the intrinsic micromotion(IMM) in the sense that it cannot be made zero by fine-tuning the DC compensation voltages. However, its size is proportional to $u_1 * q/2$ and usually $q << 1$. Thus, its size is at least an order of magnitude smaller than the other oscillating term, $u_0 \cos\Omega_{RF}t$. This term is called the excess micromotion(EMM). Its size is proportional to u_0, and can be made arbitrarily small by an appropriate choice of compensation voltages.

The voltages are calibrated by observing the size of EMM at different voltages. Our trap has two sets of compensation electrodes, and they are optimized using different methods. As shown in Fig. 3.6, the RF field responsible for micromotion is perpendicular to the compensation field directions. The Y micromotion is compensated by changing the voltage of the X electrode and vice versa.

The X-electrode, which pushes the ion along the direction of the momentum vector of the Raman transition, is optimized by observing how the ion's position shifts as we lower or raise the trapping RF voltage. When the RF trap is weak, the equilibrium position formed by the linear DC potential and the quadratic RF potential is moved in favor of the DC potential. Therefore, one can minimize u_0 by minimizing the change in the position of the ion when the strength of the RF trap is changed. For now, this is the only method available for us to

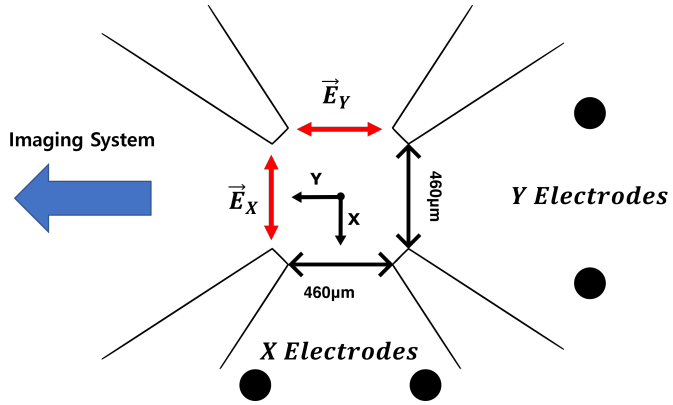

Figure 3.6: Simplified RF field lines(red) and position of compensation electrodes. The Y electrodes push the ion along the Y axis, which changes the magnitude of the X micromotion. The X electrodes move the ion along the X axis and change the Y micromotion. The X micromotion is parallel to the pulse laser momentum vector and can be detected by observing qubit transitions by the Bessel sidebands. The Y micromotion is optimized by minimizing ion position change when the RF trap power is lowered.

minimize the Y micromotion because our lasers, both CW and pulse lasers, do not interact with it.

The X micromotion is parallel to the laser momentum vector, $\Delta\vec{k}$, and can thus be measured using Raman transitions. Just like in an EOM, micromotion along $\Delta\vec{k}$ modulates the electric field phase of the laser when measured in the frame of the trapped ion, which results in n-th order Bessel sidebands, $J_n(\beta)$, where $\beta = \Delta\vec{k} \cdot \vec{V}_0/\Omega_{RF}$ is the phase modulation index with $\Delta\vec{V}_0$ being the amplitude and direction of the micromotion. We can drive qubit transitions using the Bessel sidebands by setting the Raman detuning to equal $\pm\Omega_{RF}$. The Rabi frequency of these transitions, $\Omega_{\pm 1}$ is proportional to the size of the micromotion in the direction of $\Delta\vec{k}$. It is known that $\frac{\Omega_{\pm 1}}{\Omega_0} \simeq \beta/2$ [67]. Therefore, the size of micromotion can be estimated by comparing the Rabi frequencies of the Bessel sidebands to that of the carrier. We typically find that the Bessel

sidebands are about an order of magnitude slower at optimal compensation voltage, which implies $\beta \sim 0.1$.

When scanning for the best compensation voltage for the first time, we were quite confused because there seems to be multiple values of compensation voltages where $\Omega_{\pm 1}/\Omega_0$ is minimized. This was to be expected because the Bessel function has many extrema, and $J_0(\beta)$ and $J_{\pm 1}(\beta)$ oscillate out of phase as shown in Fig. 3.7. A better method is to observe the 2nd sideeband as well. This is done by setting the Raman detuning to $\pm 2\Omega_{RF}$. The 2nd sideband oscillates out of phase with the 1st sideband and the carrier, but at $\beta = 0$, both of the sidebands are minimized while the carrier is maximized. Therefore, we found the optimal voltage by observing all three curves and finding the value of the voltage where the sidebands are simultaneously suppressed but the carrier is maximized.

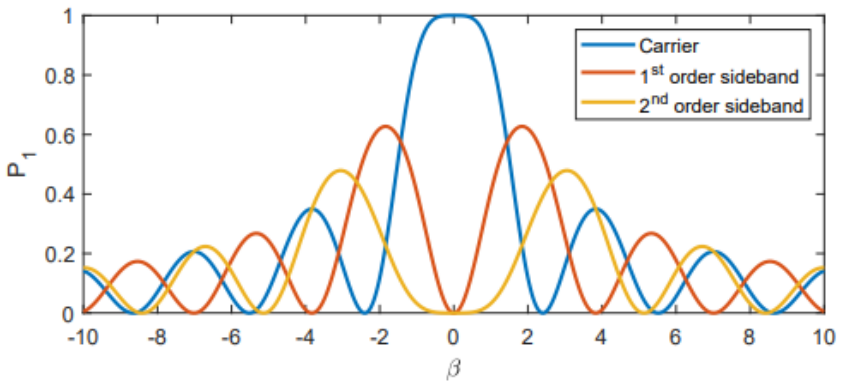

Figure 3.7: Evolution of zero-th, first and second order Bessel functions [68]

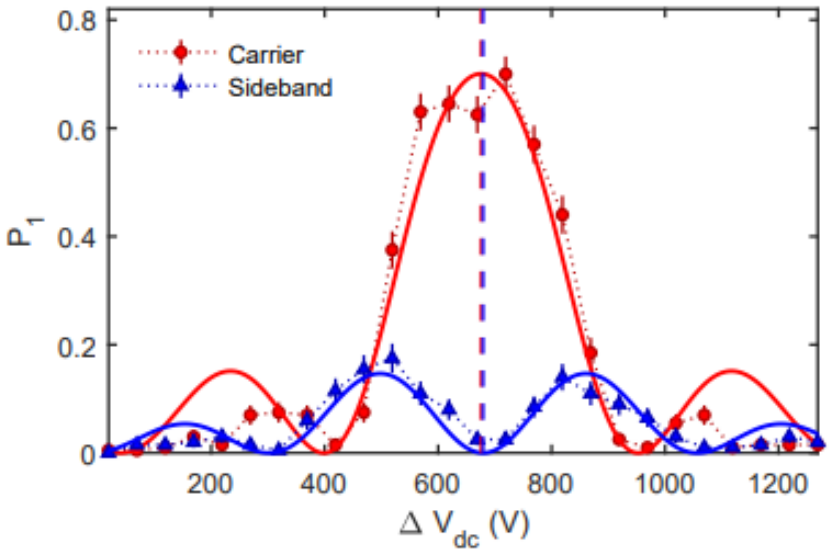

Figure 3.8: Experimentally measured values of the Bessel function. Here, the probe time was fixed while scanning the value of the Y electrode voltage. Also note that this data set was taken at $V_{endcap} = 500V$ as opposed to the usual operating condition of $V_{endcap} = 1300V$. The ΔV_{dc} values are absolute values, and their actual values range from $0V$ to $-1300V$ [68].

In a well-designed trap, the primary source of EMM is the presence of stray charges that adhere to trap surfaces. Therefore, minimizing EMM is achieved by finding the right combination of DC electrode voltages that counters the effect of stray charges on the electric potential landscape. In our setup, EMM compensation rarely needs to be recalibrated. We believe it is because the electrodes are entirely made of conductor and the ion is relatively far away from them.

We note that probably due to the misalignment of the trap electrodes or RF pickup by the DC electrodes, there are significant couplings between the RF power, endcap voltage, and the Y compensation voltage. For example, the data in Fig. 3.8 was taken with $V_{endcap} = 500V$ which is much lower than the endcap voltage we usually use, $1300V$. At $1300V$, the compensation voltage is $-1270V$ instead of ~ -700 V as shown in the figure. There is also a weaker dependence on the trap RF power, although it does not change much between powers corresponding to radial secular secular frequencies $(2\pi)1000kHz \sim (2\pi)1400kHz$. Also, there is probably a small axial micromotion, which is present in most linear Paul traps due to the finite length of the RF electrodes. We currently neither have the ability to detect nor correct it, and believe that it does not affect the experimental results. However, if we change direction of the pulse laser beams and change the direction of $\Delta\vec{k}$, we will be affected by the axial micromotion. This could be problematic because the two endcap electrodes are electrically shorted in the vacuum chamber, and therefore we currently do not have any means to cancel out axial micromotion.

3.4 Motional heating and decoherence

The stability of the motional quantum state is essential because most trapped ion experiments utilize it to some degree. Therefore, we should correctly characterize the heating rate and the motional coherence time.

3.4.1 Heating rate measurements

The heating rate for the motional modes can be measured as follows. First, we cool the motion to the quantum ground state using sideband cooling. Second, we wait for a certain amount of time, T_{wait}, with all the lasers turned off so that the ion's motion exchanges energy only with the environment, which includes the noises in the electric potential of the trap and collision with the background gas. Finally, we measure the strength of the red and blue sideband transitions. They are functions of phonon number as shown in Eq. (3.2), so with some math we can convert them into the mean phonon number of a Boltzmann distribution, which corresponds to the temperature of the ion [65, 69]:

$$\bar{n} = \frac{P_r/P_b}{1 - P_r/P_b} \tag{3.8}$$

where $\bar{n}$ is the mean phonon number, and P_r and P_b are the red and blue sideband excitation probabilities with the same probe beam intensity and probe time. The results are shown in Fig. 3.9 and Fig. 3.10.

The heating rate for the X mode is 34.26 ± 27.16 $phonons/s$, and for the Y mode 6.97 ± 3.95 $phonons/s$. Note that because theses are calculated in terms of $phonons/s$, they will change when the secular frequencies change. The heating rate is significantly smaller for the Y mode even after considering the difference in secular frequency. This was an unexpected results, because our

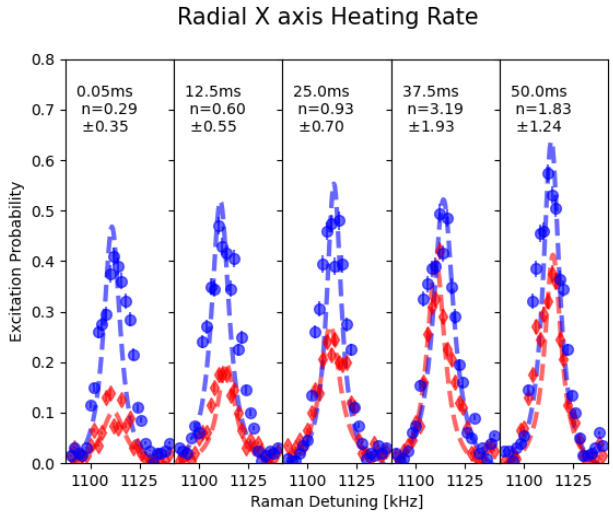

(a)

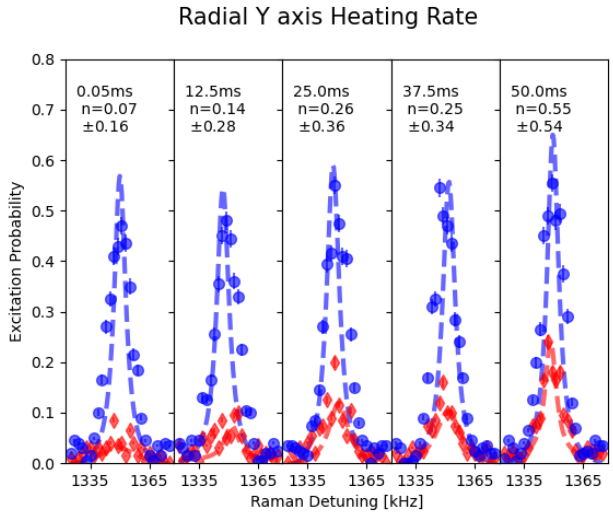

(b)

Figure 3.9: (a) Red and blue sideband scan results of the radial X mode. (b) Red and blue sideband scan results of the radial Y mode. The vertical axes are qubit excitation probability, and the horizontal axes are absolute values of the Raman detuning in kHz. Red and blue lines are fits to a Lorentzian model for the red and blue sideband transitions.

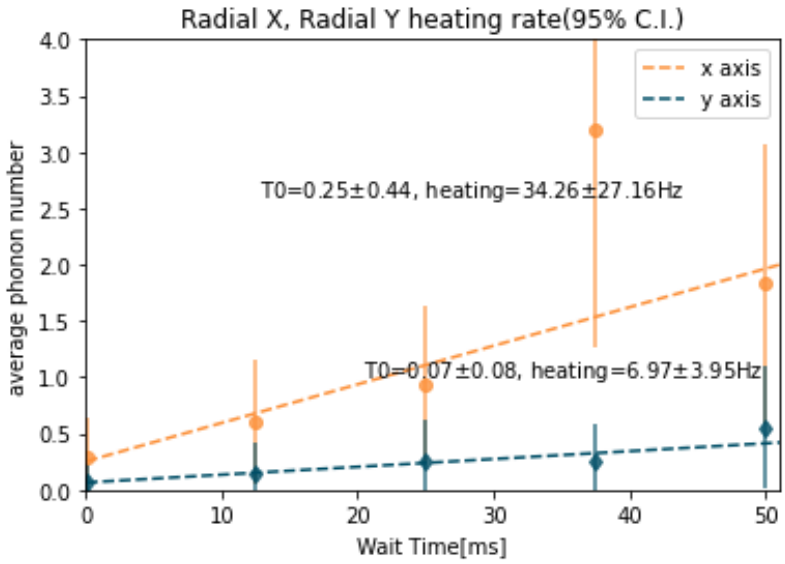

Figure 3.10: The heating rates for the X and Y modes are estimated by linear regression to the mean phonon numbers measured after waiting for T_{wait}. The X mode gains about 34 phonons per second while the Y mode heats up by 7 phonons per second. The uncertainties represent 95% confidence intervals.

trap has cylindrical symmetry and therefore the two transverse axes should be subject to the same magnitudes of electrical noises. It could be due to the misalignment of the trap electrodes, which might position the ion closer to an electrode along the X axis. It is known that the heating rates typically scale as d^{-k} where d is the distance between the ion and the electrode surface and $2 \lesssim k \lesssim 4$ [70, 71]. Therefore, an anisotropy in the ion-electrode distance could result in anisotropic heating rates. It has not been verified in our setup, as we do not have the ability to measure d precisely. Also, we note that the heating rate measurements were done with the X and Y modes separated by about 300 kHz. This is achieved by adding a few volts of DC offset voltage to the RF electrodes. It has the side-effect of rotating the principal axes, and in this case the angles between $\Delta\vec{k}$ and the two axes, θ_X and θ_Y, are 45°. In most

of our experiments we set the DC offset to a lower value which rotates the principal axes and changes θ_X and θ_Y by about 20°. Thus, the heating rates in these experiments are expected to be slightly different from the values shown in Fig. 3.10. Numerical simulations which will be introduced in the remaining chapters indicate that in all experiments heating rates of the same order of magnitude as the measured values do not affect the experimental results.

3.4.2 Motional state coherence time measurements

We measure the coherence time of the motional states by observing the Ramsey fringes of a superposition of the motional ground state and the first excited state. The procedure is as follows. First, we cool the motional states to the ground state using sideband cooling. Second, we apply a blue sideband(BSB) $\pi/2$ pulse that results in $|\psi\rangle = 1/\sqrt{2}(|\downarrow\rangle|0\rangle + |\uparrow\rangle|1\rangle)$ where the first mode indicates the spin state and the second the number of phonons in the motional mode. This puts the state vector on the equator of the Bloch sphere formed by $|\downarrow\rangle|0\rangle$ and $|\uparrow\rangle|1\rangle$. Next, we wait for a variable amount of time, T_{wait} during which the state vector evolves either coherently due to the detuning of the Raman pulses or incoherently due to fluctuations in the secular frequency. The sequence ends with another BSB $\pi/2$ pulse. In an ideal situation where the BSB pulses are exactly on resonance and the trap is perfectly stable, the qubit state is $|\uparrow\rangle$. Any deviation from $|\uparrow\rangle$ indicates a non-zero detuning or decoherence.

How the coherence of the quantum state changes with time can be quantified in several ways. In the 'phase Ramsey' scheme, one drives the BSB $\pi/2$ pulse precisely on resonance with the motional mode of interest. This removes the precession of the state vector on the Bloch sphere due to detuning. After waiting for T_{wait}, a second $\pi/2$ pulse is applied with a relative phase ϕ to the first one.

When we measure the qubit state while ϕ is scanned from 0 to 2π, we observe a sinusoidal oscillation. Its amplitude is recorded and we move on to the next value of T_{wait} and repeat the same measurement. The results from a representative data set is shown in Fig. 3.11.

In the 'time Ramsey' scheme, we intentionally detune the BSB pulses, by δ. The state vector precesses at a rate of δ, and this produces a phase difference between the first and second BSB $\pi/2$ pulses. As a result, we observe an oscillation in the $|\uparrow\rangle$ population as a function of T_{wait} with a frequency of δ. If decoherence is significant, the amplitude of the oscillation will decay, resulting in a damped oscillation of the form $P_{\uparrow}(T_{wait}) = 1/2(1 - cos(\delta T_{wait})e^{-T_{wait}/\tau})$ where τ is the coherence time.

Representative data for the time Ramsey experiments are shown in Fig. 3.12. Note that in Fig. 3.12, the sideband cooling sequence was not optimized and therefore the maximum amplitude of the oscillation is not unity. Also note that both the time and phase Ramsey results were obtained with the trap RF stabilizing PID system engaged. The coherence time was on the order of a few 100 μs without PID.

The results for the phase Ramsey and time Ramsey experiments differ, with the coherence times estimated by phase scanning being about half that estimated by applying detuned Ramsey pulses. The stability of the trap potentials may have degraded over time because the phase Ramsey experiment was done a few months after the time Ramsey experiment. Also, the phase Ramsey experiment was done with near degenerate transverse modes that are separated by 27.8 kHz. The BSB pulses may have slightly excited the other transverse mode that is not being measured. The bump at around 6 ms present in both the X and Y data might have been caused by the interaction of the X and Y

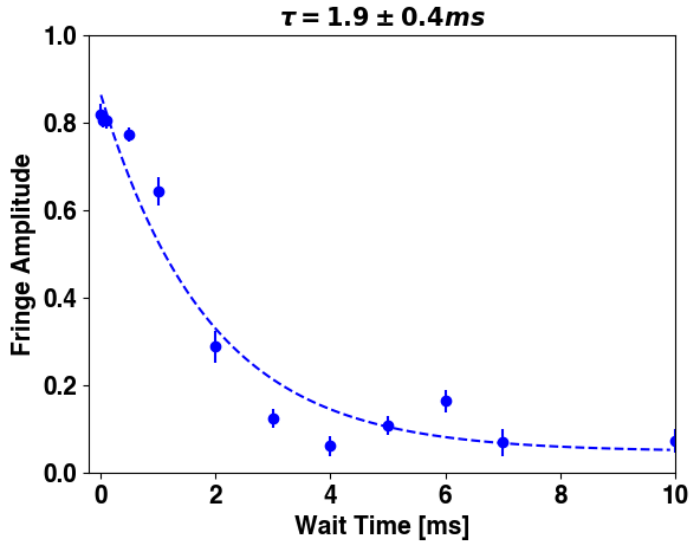

(a) X mode phase Ramsey results

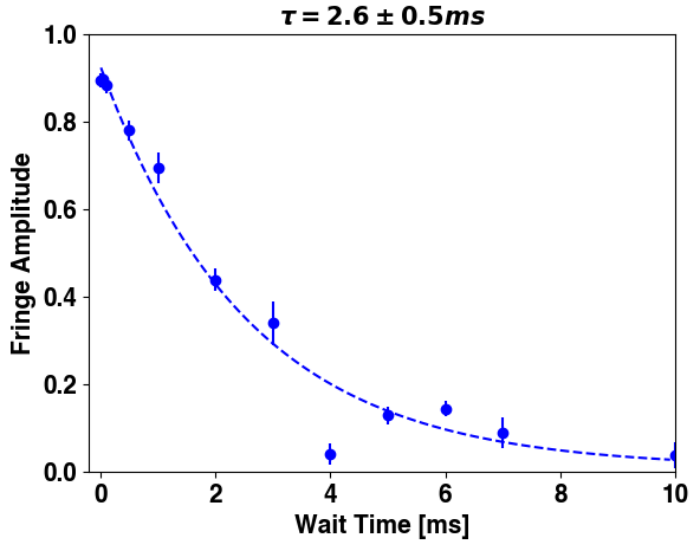

(b) Y mode phase Ramsey results

Figure 3.11: (a) Ramsey sequence with BSB pulses resonant to the X mode. Coherence time estimated from fitting the individual data to sinusoidal oscillation and then fitting the oscillation amplitudes to an exponential decay curve of the form $A * exp(-t/\tau) + C$ where τ corresponds to the motional state coherence time. (b) Ramsey sequence with BSB pulses resonant to the Y mode.

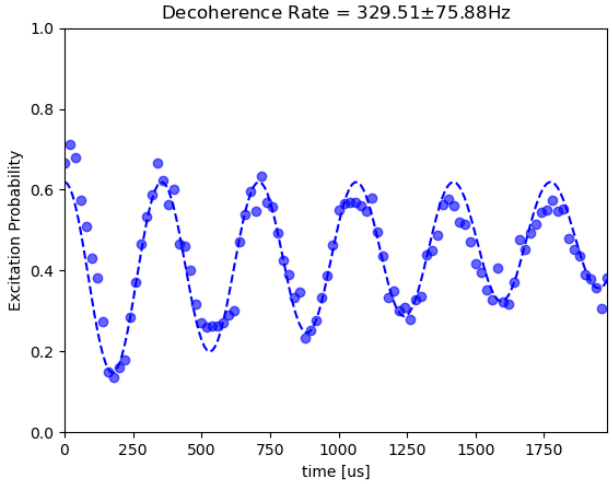

(a) X mode time Ramsey results

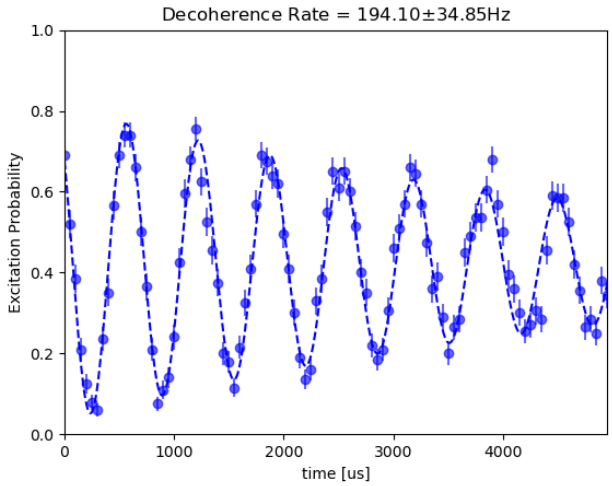

(b) Y mode time Ramsey results

Figure 3.12: (a) Ramsey sequence with a $\sim$ 3 kHz detuning for the X axis. Coherence time estimated from fitting the data to damped sinusoidal oscillation is $1/(329.51\ Hz) \simeq 3.0\ ms$ (b) Ramsey sequence for the Y mode with a detuning of $\sim$ 1.5 kHz. Estimated coherence time is $1/(194.1\ Hz) \simeq 5.2\ ms$

mode as well.

3.5 Qubit state coherence time and magnetic field calibration

3.5.1 Magnetic field calibration

We have three sets of coils that independently produce magnetic fields in three orthogonal directions. They are wound around the viewports of the vacuum chamber as explained in Fig. 2.14. We calibrate them by tracking the Zeeman sublevels ($\left|S_{1/2}, F=0, m_F=0\right\rangle \rightarrow \left|S_{1/2}, F=1, m_F=\pm 1\right\rangle$) as a function of the applied current for the bias coil. The results are shown in Fig. 3.13.

The data were fitted to a formula that takes both the ambient field and the applied field into account. The size of the Zeeman shift is proportional to the magnitude of the B field. Therefore, if we define the magnitude of the B field as $|\vec{B}| = \sqrt{(B_x + B_{ax})^2 + (B_y + B_{ay})^2 + (B_z + B_{az})^2}$ where a indicates ambient, the observed Zeeman splitting should be $\omega_{zeeman} = \mu_B |\vec{B}|$ ($\mu_B = 1.4$ MHz/G). If we fix two of the applied B fields and scan the other, the Zeeman splitting should be minimized when the applied B field cancels the ambient B field in its direction. For example, we can assume that $\omega_{zeeman} = \mu_B \sqrt{(k_x I_x + B_{ax})^2 + C}$ where k_x is the ratio of the applied current and the B field, I_x is the applied current for the X coil, and C is the sum of the ambient and applied fields in the other directions. By fitting the data in Fig. 3.13 to this model, we can find the ambient field components and the coil proportionality constant in a single fit. The results of the fit are presented in Fig. 3.13. Currently, the Y coil is used to provide the bias field in the direction of the imaging system, and the X and Z coils are used to cancel ambient fields. The coil calibration experiment was mainly carried out by Jiyong Yu.

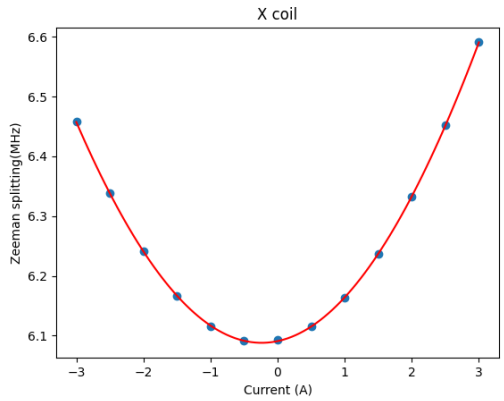

(a)

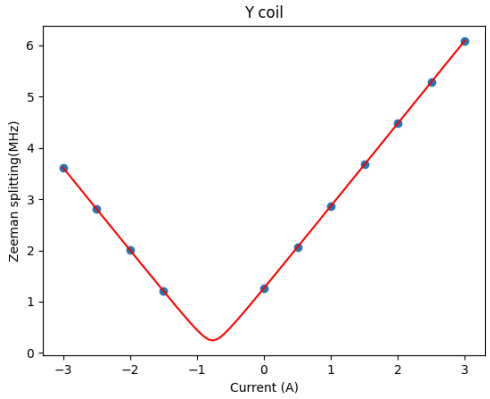

(b)

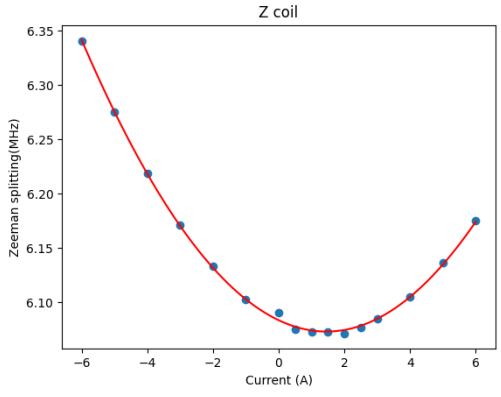

(c)

Figure 3.13: The data points in each plot were obtained by scanning the current of the coil of interest while the other two are fixed. The coil constants in G/A are as follows: $k_x = 0.557, k_y = 0.133, k_z = 0.175$. The ambient fields are: $|B_{ax}| = 0.133G, |B_{ay}| = 0.886G, |B_{az}| = -0.255G$

3.5.2 Qubit state coherence time measurement

Ramsey interferometry is an essential tool for characterizing the stability of the setup because it allows us to probe the coherence time of the system without continuously applying control fields such as the laser or microwave fields. In this section, we utilize it to characterize the coherence time of the qubit states.

The Ramsey sequence is identical to that of motional state coherence measurement. However, we drive the carrier transition to change only the qubit state and leave the motional states in their initial states. Fig. 3.14 shows the coherence time for the qubit states measured by two control fields, microwave and co-propagating pulse laser beams. They are ideal for measuring the relatively long coherence time of the qubit itself. They are not affected by control field phase fluctuations during the Ramsey wait time because of their relatively long wavelength of about two centimeters. If we try to measure the qubit coherence time with pulse laser beams in perpendicular geometry, the phase fluctuation between the two beams will scramble the phase difference between the first and second Ramsey pulses. The measured coherence time would show the coherence of the interfering fields rather than the qubit states.

The qubit coherence time measured from these experiments are 242 ms for the microwave and 275.2 ± 34.5 ms for the pulse laser. The result from the microwave experiment was obtained before we were able to sufficiently characterize the setup, but we present the data for reference. The measured coherence time is of the same order of magnitude as other trapped ion systems with $^{171}Yb^{+}$ ion qubits, perhaps closer to the shorter end [72, 5]. Nonetheless, our coherent manipulation sequence is typically 2$\sim$3 ms at maximum. Therefore a coherence time close to 300 ms is enough for all the experiments presented in this thesis.

We believe the qubit coherence time is currently limited by the stability of

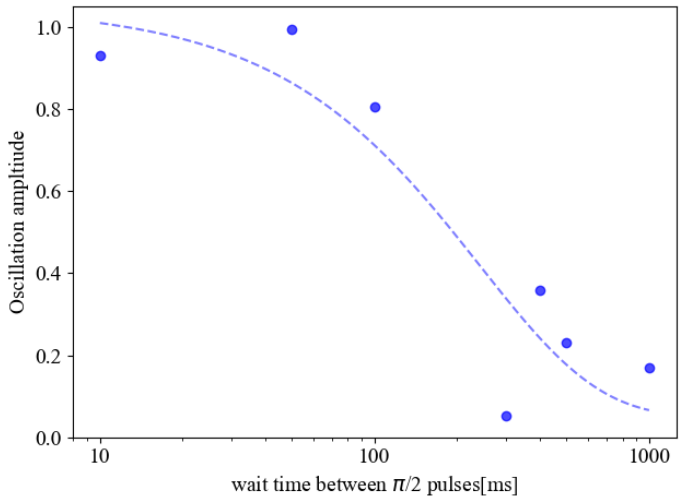

(a) Time Ramsey result for the qubit states with microwave $\pi/2$ pulses.

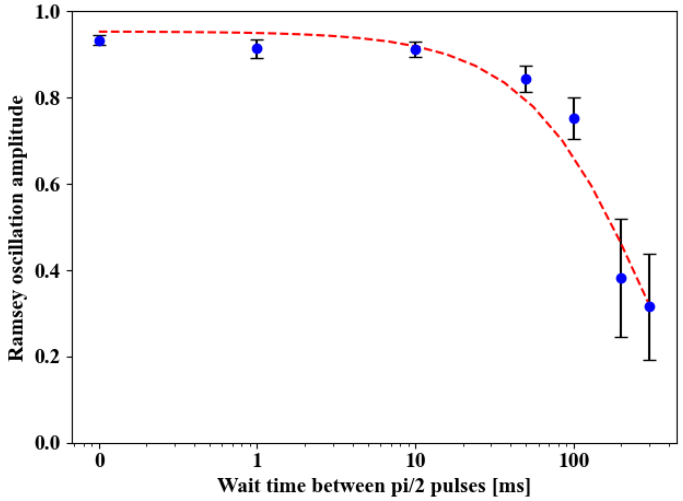

(b) Phase Ramsey result for the qubit states with co-propagating pulse laser $\pi/2$ pulses

Figure 3.14: (a) Coherence time measurement for the qubit state with slightly detuned microwave pulses. (b) Qubit state coherence time measurement with co-propagating pulse laser beams. Since the two beams used for the Raman transition physically overlap, beam path fluctuation and the resulting phase noise can be ignored. Note that the horizontal axes are in log scale.

the magnetic fields generated by copper wire coils. A commercial power supply (Keithley, 2230G) drives the coil currents, and currently we do not have any stabilizing mechanism. Due to second order Zeeman effect, the qubit frequency changes as a function of the bias magnetic field as $f_{qubit} = 12.642812118.5 + (310.8)B^2$ Hz where B is the magnitude of the bias field in Gauss [72]. Therefore, we can infer the stability of the qubit frequency from the output current stability of the power supply δI.

$$\delta f_{qubit}/\delta I = (\delta f/\delta B) * \delta B/\delta I = (310.8Hz)2Bk \tag{3.9}$$

In Eq. (3.9), k is the B field generated per unit current. $I = 4.3$ A but 0.767 A is used to cancel ambient field, so the effective current is 3.532 A. Also, by measuring the position of the Zeeman sidebands we have found that $k = 1.154$ G/A. The magnitude of the bias field is 4.076 G. Therefore, $\delta f = 2924\ Hz/A * \delta I$. According to the data sheet for the power supply, the current noise is 5 mArms, which implies $\delta I \simeq 5$ mA, and a qubit frequency noise amplitude of $\delta f_{qubit} \simeq 14.6$ Hz or 68.5 ms which is of the same order of magnitude as the experimentally measured coherence time. The B field can be further stabilized by using a current PID system and improving the power supply stability [38], or substituting the coils with a permanent magnet [73].

Chapter 4

Quantum Gates

Digital or gate-based quantum computing is a paradigm for quantum computation in which complex quantum circuits are reduced to a combination of a few types of quantum operations, just like a classical computer that carries out every calculation by combining simple logic gates. Such sets of quantum operations are called universal gate sets and Solovay and Kitaev proved that such sets indeed exist [74, 75]. Single qubit rotations and CNOT operation comprise one such set.

Experimentally realizing and then increasing fidelity of such gate sets have been the focus of the field of experimental quantum computation in the past few decades. In the trapped ion system, the components of the universal gate set can be realized by implementing Rabi oscillations with various phases to generate single qubit rotations, and combining Molmer-Sorensen interaction with single qubit rotation on select qubits to realize the CNOT gate. Therefore, the requirement for the universal quantum computer is conceptually simplified

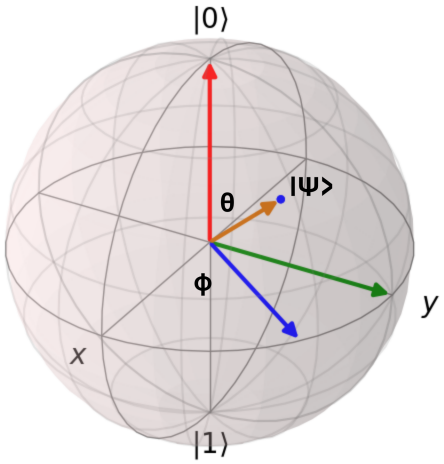

Figure 4.1: The quantum state of a single qubit, $|\psi\rangle = \cos(\theta/2)\,|0\rangle + e^{i\phi}\sin(\theta/2)\,|1\rangle$ can be faithfully represented as a point on the Bloch sphere with its azimuthal angle ϕ representing the phase between $|0\rangle$ and $|1\rangle$ and altitude corresponding to $\cos(\theta/2)$.

to phase-locked Rabi oscillation and Molmer-Sorensen interaction. These are sometimes called 'native gates' [5].

In this chapter, I will show how they are implemented in our setup. Single qubit operations will be covered first, and then the experimental realization of Molmer-Sorensen interaction and entangling gate operation will be presented.

4.1 Single qubit gates

In a trapped ion system, single qubit gates can be relatively easily implemented because they do not use the motional degree of freedom. They only require that your qubit and control field is of high quality, and the first is basically guaranteed by choosing good qubit states such as the hyperfine clock states. The second is not as trivial, but the modern microwave technology is surprisingly well developed, and one can purchase very stable phase-locked commercial RF

sources that can drive qubit transitions with high fidelity.

In this section, we will focus on single qubit gates with microwave as the control field. The pulse laser can also drive single qubit Rabi oscillation. However, when we obtained interesting results on single qubit gates, the pulse laser system was not ready. Thus most of the results in this section were achieved with microwave. Microwave single qubit gates can be combined with Molmer-Sorensen gates implemented with pulse laser beams when it is in the phase-insensitive configuration [49].

Rabi oscillation can be derived from the spin term of the interaction Hamiltonian in Eq. (3.6):

$$\hat{H}_{int} = -\frac{\hbar\Omega}{2}(\hat{\sigma}_+ e^{-i(\delta t+\phi)} + \hat{\sigma}_- e^{i(\delta t+\phi)}) \tag{4.1}$$

where ϕ is the phase of the control field, δ is the detuning from the qubit transition. On resonance, $\delta = 0$ and the above equation becomes $\hat{H}_{int} = -\hbar\Omega/2\hat{\sigma}_\phi$ and the time evolution operator is

$$\begin{aligned}
&\hat{U}_{int}(t) = e^{-i\frac{\Omega t}{2}\hat{\sigma}_\phi} = e^{-i\frac{\Omega t}{2}\hat{n}_\phi\cdot\vec{\sigma}} \\
&= \sum_{k=0}^{\infty} \frac{i^k[\Omega t/2\hat{n_\phi}\cdot\vec{\sigma}]^k}{k!} = \hat{\sigma}_I\cos(\frac{\Omega}{2}t) + i\hat{\sigma}_\phi\sin(\frac{\Omega}{2}t) \\
&= \hat{\sigma}_I\cos(\frac{\Omega}{2}t) + i\hat{\sigma}_x\sin(\frac{\Omega}{2}t) + i\hat{\sigma}_y\sin(\frac{\Omega}{2}t) \\
&= \begin{pmatrix} \cos(\theta/2) & -i\sin(\theta/2)e^{-i\phi} \\ -i\sin(\theta/2)e^{i\phi} & \cos(\theta/2) \end{pmatrix}
\end{aligned} \tag{4.2}$$

In the last line we set $\theta = \Omega t$, and the resulting matrix can be interpreted as $R_\phi(\theta)$, which is a rotation by θ around an axis on the equator defined by ϕ [76]. Therefore, we can fully control rotation of the state vector on the Bloch sphere

by controlling Ωt, the strength or duration of the resonant pulse, and ϕ, the phase of the laser. We realized $R_{x,y}(\pi/2), R_{x,y}(\pi)$ by calibrating the pulse duration and relative phase of the RF sources used to modulate the control fields. $R_z(\theta)$, azimuthal rotation, is virtually implemented by shifting the reference phase [77] or decomposing it to a combination of R_x and R_y.

In order to implement a quantum circuit consisting of multiple gate operations, we should be able to switch the phase of the control fields during the sequence. This is done by either installing a phase shifter or switching between phase-locked RF sources with identical frequencies but different phases. We used both methods, the phase shifter for the microwave gates and the switching method for the pulse laser gates. The digital phase shifter(G.T. Microwave,) is controlled by a dedicated FPGA, which output the control bitstrings depending on a 3-bit TTL input. This enables us to switch between R_x and R_y by a TTL signal emitted from the main FPGA.

We calibrated the pulse length required for π and $\pi/2$ gates by observing single qubit oscillations as shown in Fig. 4.2. It should be noted that in the current setup, the co-propagting pulse laser transition is prohibited because we are using a lin-perp-lin configuration of polarization. Installing the individual addressing setup will enable us to send a laser beam parallel to the bias B field, and then we will be able to drive co-propagating transitions again.

With the single qubit gates ready, we carried out a randomized benchmarking experiment to estimate single qubit gate fidelity [79, 80]. We generated random gate sequences each consisting of a few tens of single qubit gates. They were constrained such that the resulting qubit state after every N gates is the $|1\rangle$ state. We truncate the randomized sequence so that its length is a multiple of N. This means that we should always observe $|1\rangle$ at the end of each

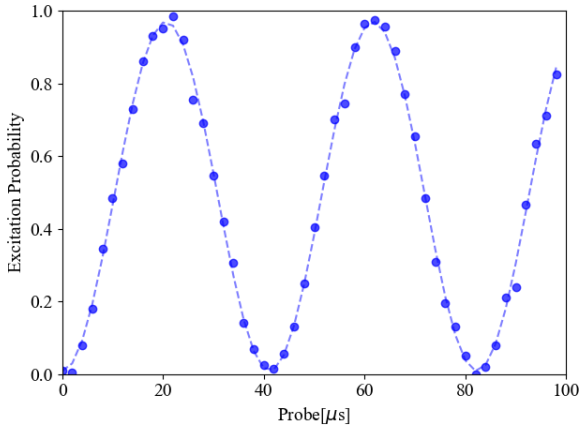

(a) Microwave Rabi oscillation

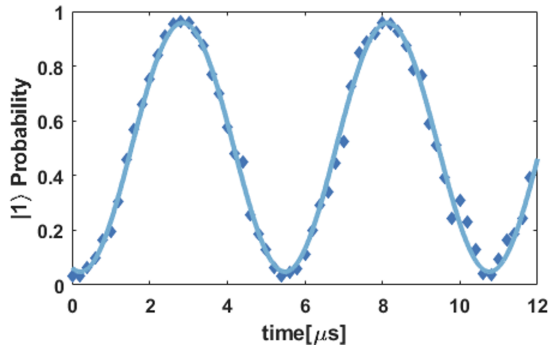

(b) Co-propagating pulse laser Rabi oscillation

Figure 4.2: Note that the co-propagating pulse laser single qubit rotation experiment was done with the same trap but in the previous lab in 2019, and does not represent the current condition of the setup.

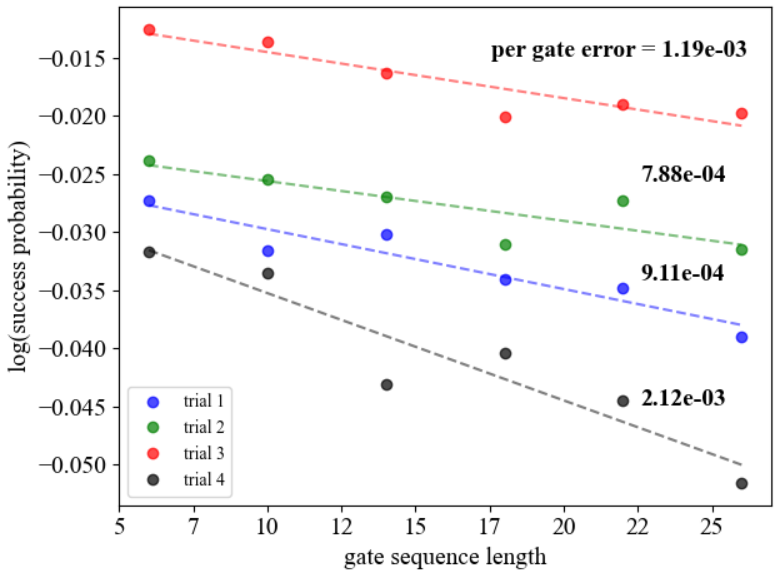

Figure 4.3: Randomized sequences of microwave single qubit gates were applied, and the qubit state at the end was compared with the theoretically expected one. By measuring how the success probability changes with gate lengths, one can measure per gate error independent of SPAM errors. We ran the benchmark four times with different randomized sequences. The per gate errors range from 0.212 % to 0.079 % depending on the sequences used.

truncated sequence, and any deviation from that is either due to SPAM errors or gate infidelities. By increasing the length of the truncated sequence, we add more gate operations and accumulate gate errors. In the end, the success rate(or error rate) is plotted against the number of gates, and fitting it to a compounding error model, $(1-p)^n$ where p is the per gate error rate, allows us to extract gate error rates. The results are shown in Fig. 4.3 and Fig. 4.4, each for microwave and pulse laser gates. The estimated gate error rates are between 0.079 % and 0.212 % for the microwave experiment, and $0.4 \pm 0.2\%$ for the pulse laser experiment.

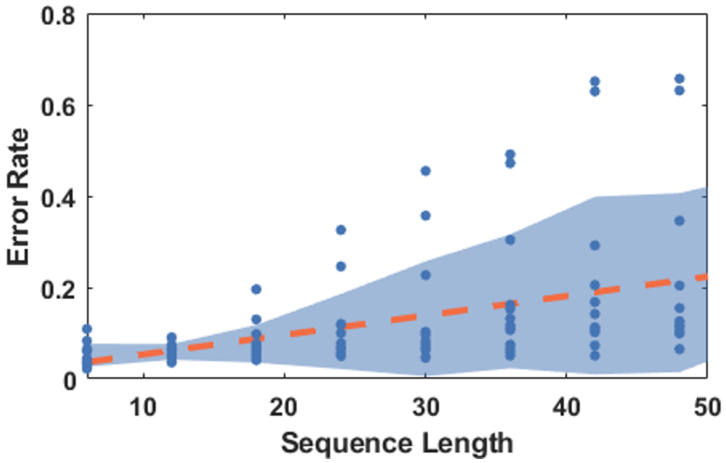

Figure 4.4: Randomized sequences of single qubit gates with co-propagating pulse laser beams were executed, and the qubit state at the end was compared with the theoretically expected one [78]. The shaded area represents the standard deviation of the 14 iterations of the benchmark. The dashed line is a linear fit to the data points and yields 0.4 ± 0.2 % of per gate error. The Y axis is error rate, not success rate as in Fig. 4.3 Note that this was done with the same trap but in the previous lab in 2019, and does not represent the current condition of the setup.

4.2 Two qubit gates

In trapped ion systems, two qubit gate are usually implemented by Molmer-Sorensen interaction [81, 6]. It uses spin-dependent force(SDF) to adiabatically drive the collective wave packet of two ions in phase space. The motion in phase space generates geometric phase. Assuming that the individual ions see the same laser phase, the eigenstates of a two qubit system with a net spin of zero, $|01\rangle$ and $|10\rangle$ stay at the origin. The other eigenstates, $|11\rangle$ and $|00\rangle$, are subject to the SDF and acquire geometric phase. This makes the composite wave function inseparable, which means that the two qubit states are entangled.

4.2.1 Spin-dependent force

The spin-dependent force is the main work horse of motional state manipulation in trapped ion experiments. It is realized by a balanced bichromatic drive that drives both the first red and blue sidebands of a motional mode simultaneously. When they are driven with a symmetric detuning of $\delta = -\delta_r = \delta_b$, we can derive the spin-dependent force Hamiltonian from Eq. (3.6).

$$\hat{H}_{SDF}(t) = \frac{\hbar\eta\Omega}{2}\hat{\sigma}_\phi(\hat{a}^\dagger e^{-i(\delta t+\phi')} + \hat{a}e^{i(\delta t+\phi')}) \tag{4.3}$$

In the above equation, $\hat{\sigma}_\phi$ is the spin operator in the direction defined by $\phi = (\phi_r + \phi_b + \pi)/2$ and the i in the coefficient of Eq. (3.6) is absorbed into it. $\phi' = (\phi_b - \phi_r)/2$ is the phase offset for the SDF, and is determined by the phase of the red and blue sideband beams. We can control them precisely by changing the phase of the DDS.

The time dependent force Hamiltonian can be represented as the sum of the raising and lowering operator for the quantum harmonic oscillator the ion is confined in.

$$\hat{H}_{force}(t) = -x_0(F_c(t)\hat{a}^\dagger + F_c^*(t)\hat{a}) \tag{4.4}$$

where $F_c(t) = (F_0/2)e^{-i((\omega-\delta)t+\phi')}$ is the complex form of the force which satisfies $F_c(t) + F_c^*(t) = F(t) = F_0\cos((\omega-\delta)t+\phi')$. $F(t)$ is the classical oscillation force that drives the ion at a frequency of $\omega - \delta$, and ϕ' is the phase offset of the force. Eq. (4.4) can be directly derived by assuming a force Hamiltonian of the form $-xF(t) - pG(t)$ [82].

When we compare Eq. (4.3) and Eq. (4.4), it is evident that Eq. (4.3)

produces a force oscillating at δ with magnitude proportional to $\eta\Omega\hat{\sigma}_\phi$. The time evolution operator for Eq. (4.3) is in fact a displacement operator in phase space. It can be shown using Magnus expansion:

$$\hat{U}_{SDF}(t) = e^{-i\hat{H}_{SDF}(t)t/\hbar} = e^{\Sigma_{k=1}^{\infty} M_k(t)} \tag{4.5}$$

$$\begin{aligned} M_1(t) &= -\frac{i}{\hbar}\int_0^t \hat{H}_{SDF}(t_1)dt_1 \\ &= -\frac{i\eta\Omega}{2}\hat{\sigma}_\phi \int_0^t (\hat{a}^\dagger e^{-i(\delta t_1+\phi')} + \hat{a}e^{i(\delta t_1+\phi')})dt_1 \\ &= \frac{\eta\Omega}{2}\left((\frac{e^{-i\delta t}-1}{\delta})e^{-i\phi'}\hat{a}^\dagger - (\frac{e^{i\delta t}-1}{\delta})e^{i\phi'}\hat{a}\right) \end{aligned} \tag{4.6}$$

$$\begin{aligned} M_2(t) &= \frac{1}{2!}\left(\frac{-i}{\hbar}\right)^2 \int_0^t\int_0^{t_1} [\hat{H}_{SDF}(t_1), \hat{H}_{SDF}(t_2)]dt_2dt_1 \\ &= -\frac{1}{2\hbar^2}\left(\frac{\hbar\eta\Omega}{2}\right)^2 \int_0^t\int_0^{t_1} \sigma_\phi^2([\hat{a},\hat{a}^\dagger]e^{-i\delta(t_1-t_2)} - [\hat{a},\hat{a}^\dagger]e^{i\delta(t_1-t_2)})dt_2dt_1 \\ &= -\frac{1}{2\hbar^2}\left(\frac{\hbar\eta\Omega}{2}\right)^2 \int_0^t\int_0^{t_1} \hat{\sigma}_\phi^2 2i\sin(\delta(t_1-t_2))dt_2dt_1 \\ &= -\frac{1}{2\hbar^2}\left(\frac{\hbar\eta\Omega}{2}\right)^2 \frac{2i}{\delta^2}(\delta t - \sin(\delta t)) \\ &= -i\hat{\sigma}_\phi^2\left(\frac{\eta\Omega}{2\delta}\right)^2 (\delta t - \sin(\delta t)) \end{aligned} \tag{4.7}$$

The first term, $e^{M_1(t)}$ is a displacement operator $D(\alpha(t)) = exp(\alpha(t)\hat{a}^\dagger - \alpha^*(t)\hat{a})$ with the displacement defined as $\alpha(t) = (\eta\Omega/2)(e^{-i\delta t}-1)/\delta e^{-i\phi'}$. The second term is a spin-dependent geometric phase term, $exp(i\hat{\sigma}_\phi^2\Phi(t))$ where $\Phi(t) = (\eta\Omega/(2\delta))^2(\delta t - \sin(\delta t))$. The first and second terms commute. Therefore, $\hat{U}_{SDF}(t) = \hat{D}(\alpha(t))exp(i\hat{\sigma}_\phi^2\Phi(t))$. The effect of the time-dependent Hamiltonian in Eq. (4.3) is to entangle spin and motion and imbue the spin eigenstates

with corresponding geometric phases. The first is used to generate spin-motion entanglement, and the second is used to entangle the spin states in the MS gate. Higher order terms vanish because $[[\hat{H}_{SDF}(t_1), \hat{H}_{SDF}(t_2)], \hat{H}_{SDF}(t_3)] = 0$.

Before moving on to two-qubit gate experiment, we first characterized spin-motion entanglement in our setup by trapping a single ion and observing the time evolution of its spin state under the time evolution operator Eq. (4.5). Since we only have a single ion, the geometric phase, while mathematically present, cannot be measured because it is a global phase. Thus the observed physics will be a bipartite entanglement of the spin and one-dimensional motion. For a non-zero δ, the entanglement will form and disappear periodically. We applied the SDF with a few KHz of detuning because it allows us to extract information such as coherence time.

We first initialize the qubit state to $|0\rangle$ via optical pumping. Since $|0\rangle = 1/\sqrt{2}(|+\rangle + e^{i\phi}|-\rangle)$ where $|\pm\rangle$ are the eigenstates of the $\hat{\sigma}_\phi$ operator, the wave function under the SDF evolves as $1/\sqrt{2}(|+\rangle|\alpha(t)\rangle + |-\rangle|-\alpha(t)\rangle)$, which corresponds to the superposition of two separate wave packets in the phase space. After a variable amount of time evolution, we measure only the spin state, so the measured spin excitation probability is expected start from 0 but approach 0.5 as the spin wave packets move away from each other in the phase space because we trace out the motional degree of freedom. When the periodic SDF returns the wave packets to the origin, the spin and motion disentangle and the initial qubit state, $|0\rangle$, is recovered. This is illustrated in Fig. 4.5(a). In (a), the spin state is initialized to $|0\rangle = 1/\sqrt{2}(|+\rangle + e^{i\phi}|-\rangle)$. In (b), the SDF displaces the two spin states in opposite directions. Because the spin and motion are entangled, measuring the spin state in this situation should give a mixed state. (c) corresponds to $t = 2\pi/\delta$. Here, the wave packets return to the origin and

we again have a pure spin state $|0\rangle$.

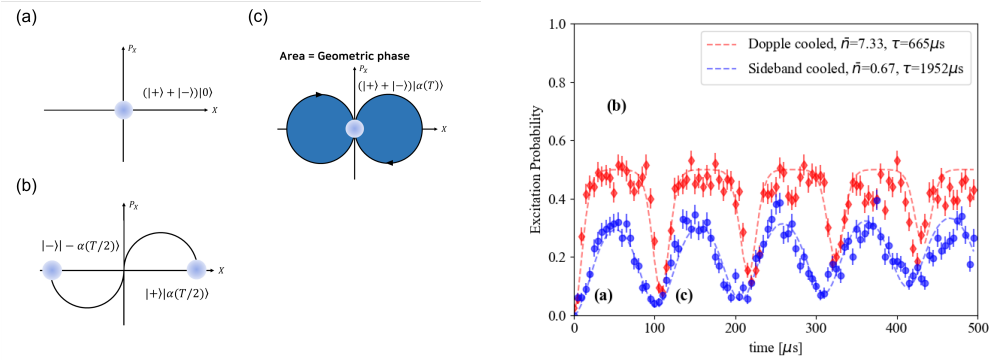

(a) (b)

Figure 4.5: (a) The wave packets split and move along a circular trajectory in phase space. The area enclosed by the trajectory corresponds to the geometric phase. (b) Time evolution of the spin state under spin-dependent force with $\delta \simeq (2\pi)10$ kHz. The spin state is modulated with a period of $2\pi/\delta$ as it is periodically entangled with the motional state. The dashed lines are fits to the theoretical model which takes into account the mean phonon number and coherence time.

The results are shown in (b) for the application of the SDF after Doppler cooling and ground state cooling. The experimental data were fitted to a theoretical model of the following form:

$$P_1(t) = \frac{1}{2}(1 - e^{(\overline{n}+1/2)|\alpha(t)|^2} e^{-t/\tau}) \tag{4.8}$$

where $\overline{n}$ is the initial mean phonon number and τ is the coherence time of the wave packet [49]. We observe that due to the effect of decoherence and imperfect experimental parameters such as change in the trap secular frequency during time evolution, the spin state does not fully return to $|0\rangle$. Such effects are detrimental to the fidelity of entangling gates because residual entanglement of spin and motion at the end of a gate pulse results in a partially mixed spin

state.

Minimization of residual spin-motion entanglement has been intensely studied in the last few years, especially because it becomes increasingly difficult to disentangle all the motional modes in a long ion chain [83, 84, 85, 86, 87]. Most of the techniques developed so far modulate the power, phase or frequency of the control fields used to drive the SDF. One of the simplest forms of pulse shaping is the Walsh gate, which is basically making an 'echo' in phase space [88]. In this scheme, the wave packet is driven in the opposite direction after completing a single circular trajectory. Any offset from the origin in phase space is canceled in the second trajectory. This can be repeated multiple times by making $2N$ loops in phase space, in which case the gate infidelity due to incomplete motional disentanglement is suppressed as $\sim O(\Delta\delta^{2n+2})$. $\Delta\delta = 2\pi/t_g - \delta$ is the effective detuning mismatch parameter defined as the difference of the actual and expected detunings from the motional mode. It quantifies the offset from the origin at the end of gate pulse.

We have experimentally verified its effect in our setup, and the results are presented in Fig. 4.6. This time, we fixed the duration of time evolution under the SDF Hamiltonian and scanned the detuning. We applied the SDF pulse for $T_{SDF} = 40\mu$s, which results in a modulation of the spin excitation probability with a period of $1/(T_{SDF}) \simeq 25$ kHz. After completing the first loop in phase space, we flipped the direction of the force by switching the phase of the DDS. This changes the laser phase and therefor the direction of SDF. We applied the flipped SDF for another 40 μs and measured the spin state. The data were fitted to the theoretical curves which can be obtained by plugging the following forms of displacement into Eq. (4.8):

$$\alpha_{unmod.}(t) = \frac{\eta\Omega}{2\delta}(1 - e^{i\delta t}) + \frac{\Delta\delta}{\delta}$$
$$\alpha_{mod.}(t) = \frac{\eta\Omega}{2\delta}(2 - e^{i\delta t} - e^{-i\delta t}) + \frac{\Delta\delta}{\delta} \tag{4.9}$$

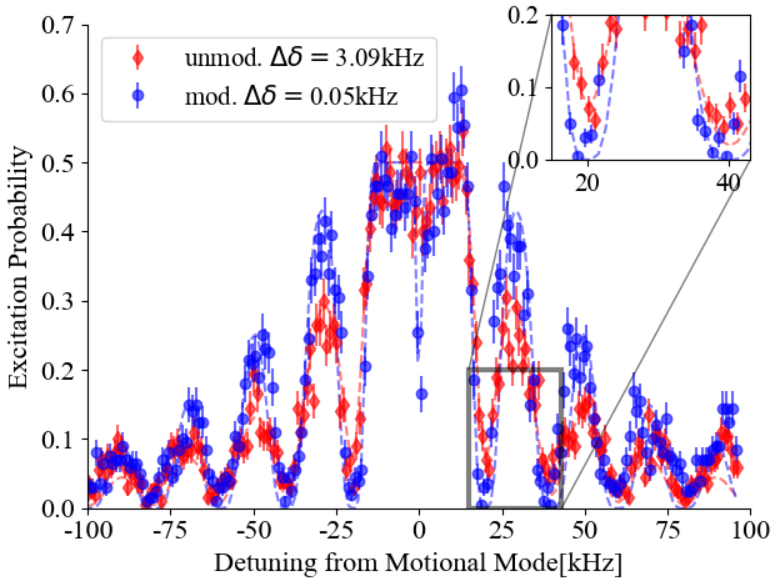

Figure 4.6: Red data points are the unmodulated SDF detuning scan results. Blue data points are obtained by applying the 1st order Walsh gate where we make two loops in phase space with opposite phases. In both experiments, each SDF pulse were applied for 40 μs. The dashed lines are fits to theory.

The blue data points, obtained by applying Walsh SDF pulses, are closer to $P_1 = 0$ as expected. The inset clearly shows the effect of Walsh pulse modulation. The value of the effective detuning mismatch $\Delta\delta$ estimated from the fits are 3.09 kHz for the native SDF and 0.05 kHz for the Walsh SDF, almost two orders of magnitude smaller.

One notable feature of this curve is that at $\delta = 0$ for the Walsh SDF, the wave packet follows a linear trajectory for 40 μs and then comes straight back to the origin during the second SDF evolution of the same duration. Ideally,

this results in the wave packet at the origin and the disentanglement of spin and motion. This effect is observed in the data, although the spin only partially returns to $|0\rangle$. This could be due to imperfection in phase calibration for the second SDF. Any deviation from π of the phase difference between the first and second SDF results in a proportional offset from the origin at the end of the pulses.

4.2.2 Molmer-Sorensen gate theory

The theory of spin-dependent force should be slightly expanded to describe the generation of entangled qubit states by Molmer-Sorensen interaction. First, let us examine how the time evolution operator of Eq. (4.7) acts on the $|00\rangle$ state by expressing $\hat{\sigma}_\phi^2$ in the two-qubit basis. Since $\sigma_\phi = e^{i\phi}\sigma_- - e^{-i\phi}\sigma_+$, $\sigma_\phi^2 = \sigma_-^2 e^{i2\phi} - \sigma_+^2 e^{-i2\phi} - \sigma_+\sigma_- - \sigma_-\sigma_+$. Also, $\sigma_\pm^2 = \sigma_\pm^{(1)} \otimes \sigma_\pm^{(2)}$ where the number in parenthesis indicates the which ion in the chain the operator acts on. We know from the arithmetics of angular momentum ladder operators that $\sigma_+\sigma_- + \sigma_-\sigma_+ = 2(\sigma_x^2 + \sigma_y^2)$. Thus, σ_ϕ^2 expressed in the two qubit basis is:

$$\hat{\sigma}_\phi^2 = \begin{pmatrix} -2 & 0 & 0 & 2e^{2i\phi} \\ 0 & -2 & -2 & 0 \\ 0 & -2 & -2 & 0 \\ 2e^{-2i\phi} & 0 & 0 & -2 \end{pmatrix} \tag{4.10}$$

where each column represents to $|00\rangle, |01\rangle, |10\rangle$ and $|11\rangle$ from the left. Decomposing the initialized two-qubit state into the eigenstates of $\hat{\sigma}_\phi^2$ yields $|00\rangle = |e_1\rangle + |e_2\rangle = 1/\sqrt{2}(|00\rangle + e^{-2i\phi}|11\rangle) + 1/\sqrt{2}(|00\rangle - e^{-2i\phi}|11\rangle)$ where $|e_{1,2}\rangle$ are two of the eigenstate of $\hat{\sigma}_\phi$. Therefore, $\hat{U}_{SDF}(t_g)|00\rangle = 1/\sqrt{2}(\cos 2\Phi(t)|00\rangle - i\sin 2\Phi(t)|11\rangle)$. Here we can see that as the geometric phase increases, the two-

qubit state oscillates between $|00\rangle$ and $|11\rangle$. A Bell state of the form $|00\rangle - i\,|11\rangle$ is created when $\Phi = \pi/8$ which is satisfied when $\Omega = \delta/(2\eta)$ and $\delta t_g = 2\pi$.

The above derivation can be extended to consider more than a single motional mode by modifying the expression for Φ. In our system, due to the close spacing of the cm and tilt modes, at least two motional modes have to be taken into account. It should also be noted that the tilt mode acquires a negative geometric phase owing to the out-of-phase nature of the motion while the cm mode acquires a positive one. Considering this, we can derive the following time evolution of the spin population [60]:

$$\begin{aligned}
P_{01}(t) = P_{10}(t) &= \frac{1}{8}\left(2 - e^{-8(\overline{n}_1+\frac{1}{2})|\alpha_1(t)|^2} - e^{-8(\overline{n}_2+\frac{1}{2})|\alpha_2(t)|^2}\right) \\
P_{00}(t) &= \frac{1}{8}(2 + e^{-8(\overline{n}_1+\frac{1}{2})|\alpha_1(t)|^2} + e^{-8(\overline{n}_2+\frac{1}{2})|\alpha_2(t)|^2} \\
&\quad +4\cos(4\Phi(t))e^{-2((\overline{n}_1+\frac{1}{2})|\alpha_1(t)|^2+(\overline{n}_2+\frac{1}{2})|\alpha_2(t)|^2)}) \\
P_{11}(t) &= \frac{1}{8}(2 + e^{-8(\overline{n}_1+\frac{1}{2})|\alpha_1(t)|^2} + e^{-8(\overline{n}_2+\frac{1}{2})|\alpha_2(t)|^2} \\
&\quad -4\cos(4\Phi(t))e^{-2((\overline{n}_1+\frac{1}{2})|\alpha_1(t)|^2+(\overline{n}_2+\frac{1}{2})|\alpha_2(t)|^2})
\end{aligned} \tag{4.11}$$

where the subscripts 1 and 2 each indicate the center-of-mass and tilt mode.

4.2.3 Two qubit state measurement

So far, we have relied on the threshold discrimination technique to determine the spin population of the ion. However, this method cannot be easily applied to two or more qubits because the photon distribution profiles of $|10\rangle$ or $|01\rangle$ and $|11\rangle$ overlap significantly, due to their Poissonian nature. Thus, a number of novel techniques have been developed for the measurement of multi-qubit states.

EMCCD's have been utilized for multi-qubit detection in which the image of the ion chain is analyzed to obtain the photon statistics for each qubit separately [16, 17, 18]. Also, PMT arrays have been aligned to the ion chain so that the photons from each ion impinge on fibers that individually connect to each of the PMT's. They register the photon counts from each ion, and the resulting histograms are analyzed by the conventional threshold method [19, 20, 21]. These methods are scalable in that they can accomodate a large number of ions. However, they need specialized equipment such as an EMCCD or a fiber array. Neither were readily available to us, so we decided to take an alternative approach which is to collect the fluorescence from two qubits with the same PMT, and decompose it to the histograms of the three possible qubit states: $|11\rangle, |00\rangle$ and $|01\rangle$ or $|10\rangle$ [89, 90]. This is done by assuming the following relation between the aggregate photon counts from the PMT and the population of each of the three qubit states:

$$\vec{\psi} = P_{00}\vec{A}_{00} + P_{01+10}\vec{A}_{01+10} + P_{11}\vec{A}_{11} \tag{4.12}$$

where $|\psi\rangle$ is the observed histogram, P_{ij} is the population of the qubit state $|ij\rangle, i, j = 0, 1$, and $\vec{A}_{ij}$ is the measured basis histogram for the qubit state $|ij\rangle$. The n-th element of each of the histogram vectors in Eq. (4.12) is the normalized number of events for detecting n photons in a single shot. We note that the $\vec{A}_{01+10}$ basis histogram was obtained by detecting the fluorescence of a single qubit in the $|1\rangle$ state. The difference between $\vec{A}_{01+10}$ and $\vec{A}_1$ was considered to be minimal because the mean photon number of $\vec{A}_1$ is close to half of that of $\vec{A}_{11}$. Also, the histogram fitting method was tested with the microwave Rabi oscillation of two qubits. Since the microwave pulse drives independent qubit transitions on the ions, the expected population is $1/2(\cos(\theta/2)|0\rangle + \sin(\theta/2)|1\rangle) \otimes$

$(\cos(\theta/2)\,|0\rangle + \sin(\theta/2)\,|1\rangle) = 1/2(\cos^2(\theta/2)\,|00\rangle + \cos(\theta/2)\sin(\theta/2)(|01\rangle + |10\rangle) + \sin^2(\theta/2)\,|11\rangle)$. The results are displayed in Fig. 4.7(b) and shows the expected pattern.

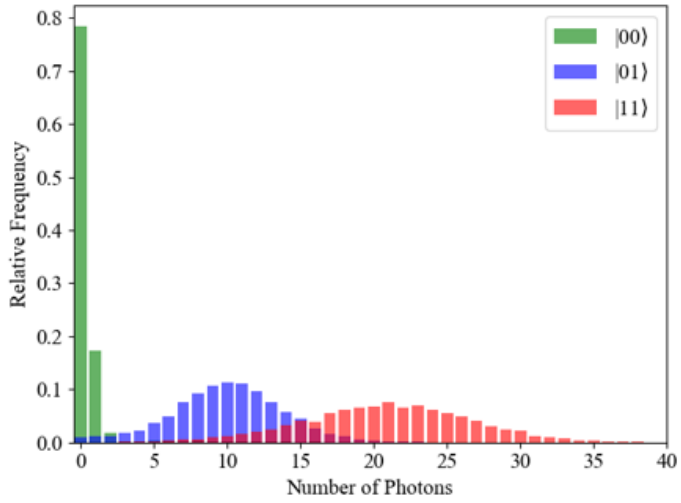

(a)

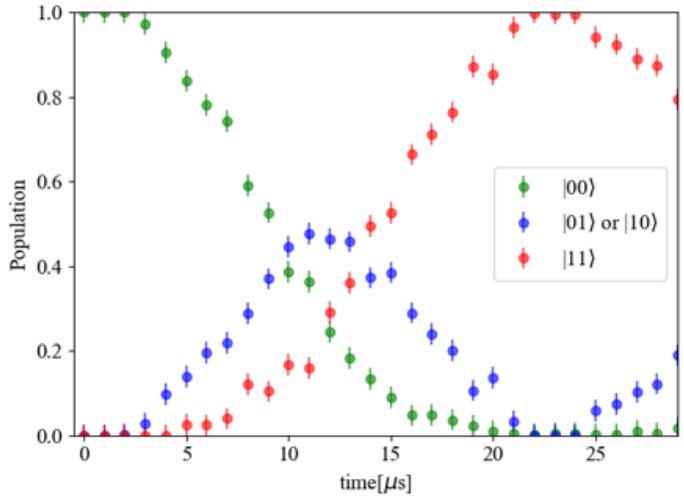

(b)

Figure 4.7: (a) Basis histograms for the three possible qubit states. Each contain approximately 10^4 shots of measurement. (b) Two-qubit microwave Rabi oscillation with populations inferred by histogram fitting method. Error bar represents standard error of the fitted population.

4.2.4 Gate parameter calibration

An MS gate sequence has to be calibrated meticulously to satisfy the following two conditions. First, the motional wave packets should return to the origin at gate time t_g in all phase spaces involved. Second, the geometric phase Φ at t_g should equal the desired value. For $|00\rangle + |11\rangle$, $\Phi = \pi/8$.

Since $\Phi \sim \Omega^2$, the size of the geometric phase can be easily optimized in a single scan of the pulse laser intensity. The gate time t_g can also be optimized in a single scan by fixing the gate detuning δ and scanning the duration of the MS gate pulse, and finding the t where P_{01+10} equals zero [6, 14]. However, in our system, due to the weak axial potential, the center-of-mass(cm) mode and the tilt mode are very close. This prohibits us from using only one of the motional modes. That means that we have to find a laser frequency that satisfies $\delta_{tilt} = N^{\pm 1}\delta_{cm}$ because only under this condition do the two modes simultaneously return to the origin at the same time. The situation is schematically represented in Fig. 4.8. Here, we separate the X and Y modes by about 300 kHz by applying a few Volts of DC offset voltage to the RF electrodes. We choose the Y mode for entangling gate operation, because it has a lower heating rate and longer coherence time as discussed in Fig. 3.10 and Fig. 3.12.

The first step of the calibration is balancing the Rabi frequencies at each ion. Since we do not individually address the ions or detect their individual states, we check their balance by driving the carrier transition. If Rabi oscillation for each qubit occurs at the same rate, the observed brightness of the two ions should evolve sinusoidally with a single frequency. However, if there is an imbalance in Rabi frequency between the two ions, their Rabi oscillations will eventually go out of phase and the total brightness will evolve with multiple frequencies. We observe more than 10 periods of Rabi oscillation, which allows us to balance

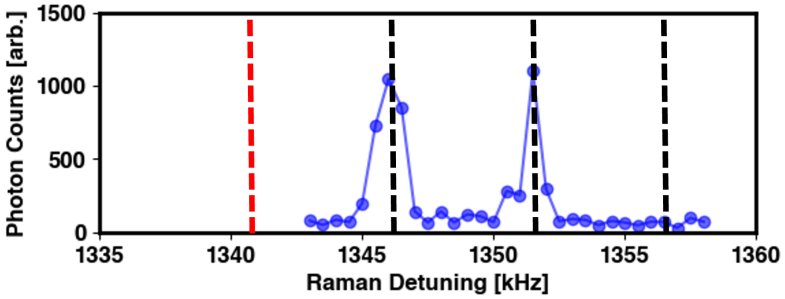

Figure 4.8: Two ion spectThe dashed vertical lines indicate detuning at which $\delta_{cm}/\delta_{tilt} = N$ or $\delta_{tilt}/\delta_{cm} = N$. The red dashed line is the detuning where the two-qubit operations results presented in this section were obtained. Here, $\delta_{Y_{tilt}}/\delta_{Y_{cm}} = 2$ The x modes are located at around $(2\pi)1000$ kHz and are not visible in this figure.

the beam intensities to better than 10%. The ratios of the Rabi frequencies can tuned by moving the horizontal and vertical Raman beams with motorized stages. The diameters of the beams are between $10 \sim 20$ μm, so steps as small as 2 μm are needed. It would be nice to be able to use smaller steps, but we are currently limited by the repeatability of the motorized stage. An example of Rabi frequency balancing is presented in Fig. 4.9.

We first set the gate time to the inverse of $\omega_{tilt} - \omega_{cm}$ and scan the gate detuning. The result is shown in Fig. 4.10. We set the Raman detuning to a value such that $\delta_{cm} \simeq -(2\pi)6.0$ kHz and $\delta_{tilt} \simeq -(2\pi)12.0$. This means that for gate pulse duration of $t_g = 167\mu s$, the wave packet makes a single loop in the tilt phase space, while in the cm phase space the wave packet makes two loops. The optimal t_g and δ are correlated because $t_g = 2\pi/\delta$ should be satisfied. Therefore the detuning scan is repeated at different values of t_g, and we settle with δ and t_g that gives the lowest odd state population. We further optimize the gate parameters by fine-tuning the frequencies of the BSB and RSB transitions to account for AC Stark shift. The intensities of the BSB and

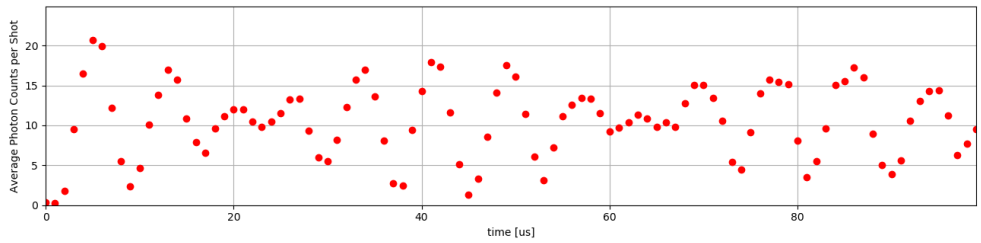

(a)

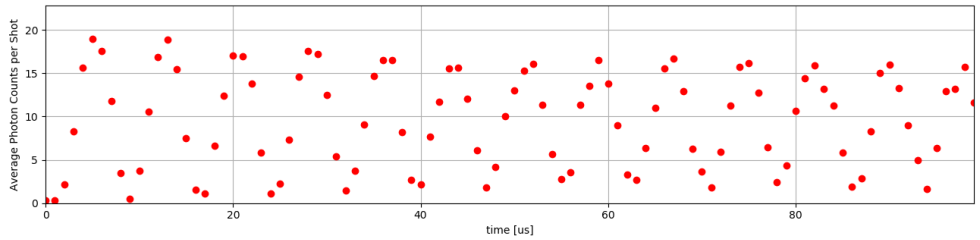

(b)

Figure 4.9: (a) Two ion Rabi oscillation when the horizontal beam is 4 μm away from the center of the ion chain. The spin states of the two ions evolve with different rates, resulting in the revival and decay of the collective spin state. (b) When the Rabi frequencies are well-balanced, the collective spin state evolves in phase, resulting in a simple sinusoidal time evolution.

RSB are also separately scanned, with the goal of minimizing the odd state population after executing the entangling gate.

The time evolution of the qubit state population is shown in Fig. 4.11. Here, we see an excellent agreement with the experiment and theory. The theoretical curves are as defined in Eq. (4.11), except for a phenomenological decoherence factor $e^{-t/\tau}$ that is multiplied to each exponential term of the form $e^{|\alpha(t)|^2}$.

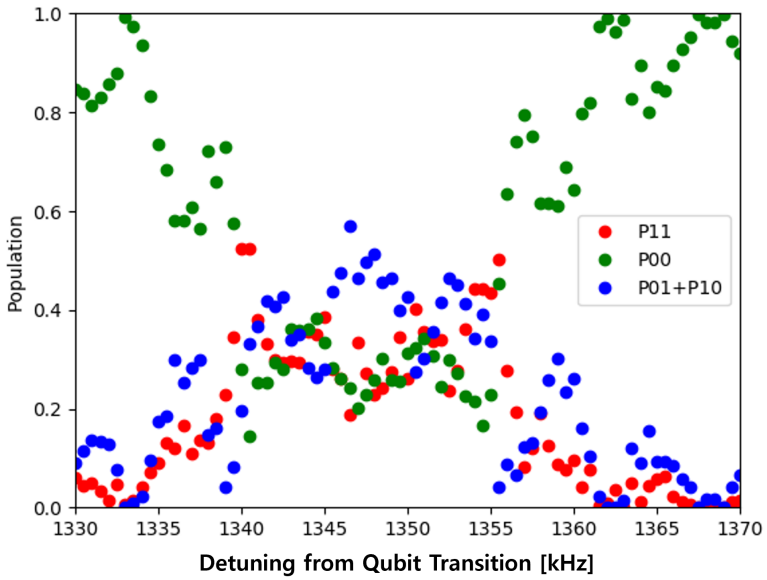

Figure 4.10: MS gate detuning scan with an expected gate time of $t_g = 2\pi/\delta \simeq 167\mu s$

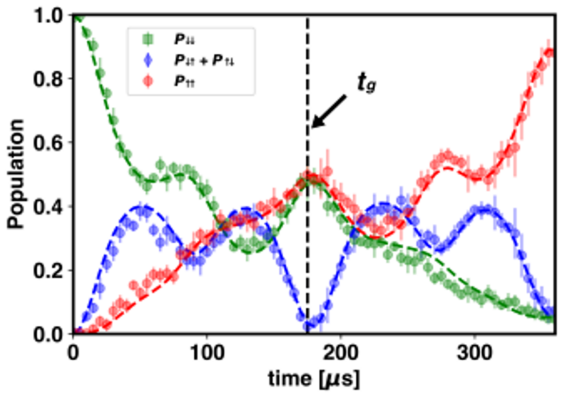

(a)

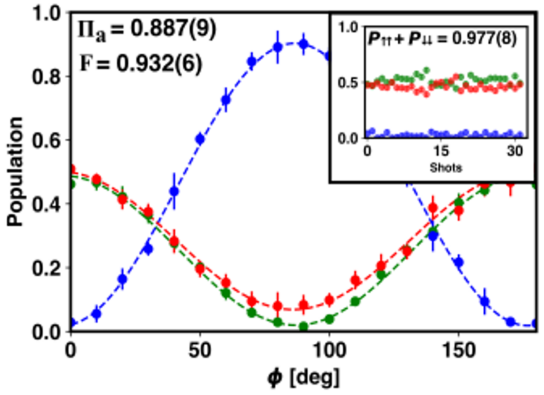

(b)

Figure 4.11: (a) The time evolution of the spin eigenstates under MS interaction. The optimal gate time t_g is indicated with a dashed vertical line. The lines are fits to Eq. (4.11) which is modified to include an exponential decoherence factors. (b) Parity oscillation of the spin states and population measurement. Parity oscillation is observed by the application of a phase-locked $\pi/2$ pulse with relative phase ϕ. When ϕ is scanned, the even states oscillate in phase while the odd states oscillate out of phase as expected [60].

4.2.5 Fidelity measurement

Characterizing a quantum state is not as simple as measuring its population distribution. Its full characterization is only achieved by measuring every element of its density matrix, or equivalently obtaining quantum state tomography with quasi-probability distributions such as Wigner function or Q function [91, 92, 43]. It is usually a time consuming and difficult task because it requires a very large amount of measurements. Luckily, while full tomography is more complicated, the fidelity of the two-qubit state can be easily measured by observing the oscillation of the spin parity defined as the difference between the even and odd spin population, $\Pi = P_{00} + P_{11} - P_{01} - P_{10}$. Fidelity is a measure of how similar two qubit states are and is defined as $F = |\langle\phi|\rho|\phi\rangle|$ where $\rho = |\psi\rangle\langle\psi|$ is the density matrix of the experimentally created quantum state and $|\phi\rangle$ is the target state.

When the target state is a Bell state of the form $|00\rangle + |11\rangle$, F can be decomposed into diagonal and off-diagonal terms as follows [6, 93]:

$$\begin{aligned} F &= \frac{1}{2}(\rho_{00,00} + \rho_{11,11}) + Im(\rho_{00,11}) \\ &= \frac{1}{2}(P_{00} + P_{11}) + \frac{1}{2}A_\phi \end{aligned} \tag{4.13}$$

The first term is obtained by measuring the sum of the $|00\rangle$ and $|11\rangle$ state population. The second term is proportional to the amplitude of the qubit state parity oscillation, A_ϕ, which is realized by applying an individual $R_\phi(\pi/2)$ gate to the entangled qubits and scanning ϕ. The results for the population measurement and parity oscillation experiment is shown in Fig. 4.11(b). From the measurements, $A_\phi = 0.887(9)$ and $P_{00} + P_{11} = 0.977(8)$, which yield a fidelity of 0.932(6). About half of the infidelity originates from miscalibration of

gate parameters such as gate detuning, gate time and Rabi frequency. The other factors include histogram fitting errors, motional state decoherence and beam pointing instability. Their contributions are quantified via numerical simulation in the next section.

4.2.6 Error analysis

In this section, we will first discuss the factors that decrease fidelity, and present numerical simulation result which shows how much infidelity they account for.

The first source of error to be examined is the accuracy of two-qubit state histogram fitting. This is quantified by fitting each of the basis histogram data to the histogram fitting model itself. It is known that imperfect measurement of a perfect Bell state, $|00\rangle + |11\rangle$, results in an infidelity of $3/2(\epsilon_0 + \epsilon_1)$ where ϵ_0 and ϵ_1 are the detection error probability for the $|0\rangle$ and $|1\rangle$ states, respectively [94]. ϵ_0 and ϵ_1 can be deduced from two-qubit state detection error rates ϵ_{00} and ϵ_{11} [94]. We estimate ϵ_0 and ϵ_1 using $\epsilon_{0,1} = 1/2(1 - \sqrt{1 - 2P_{01+10}})$. When we prepared the $|00\rangle$ state, $P_{01+10} = 0.0058$, and $\epsilon_0 = 0.0029$. For the $|11\rangle$ state, $P_{01+10} = 0.012$ and $\epsilon_1 = 0.0064$. Therefore, detection error explains 0.014 or 1.4% of the 6.8 % of measured infidelity.

Heating rate and motional decoherence were quantified in Fig. 3.10 and Fig. 3.12. The coherence time for the qubit state was measured in Fig. 3.14(b). We identify another source of qubit state decoherence that probably results from the combination of 4-th order Stark shift [45] and beam pointing and phase fluctuation. We observe this type of decoherence when we carry out microwave Ramsey experiment with the pulse laser beams turned on but set to an off resonant frequency so that it does not drive any transition.

The presence of the pulse laser beams significantly shorten the coherence

time measured by microwave gates and shifts the qubit frequency. We observed the amount of qubit frequency shift and decoherence rate at various values for the geometric mean of the powers of the two Raman beams. The pulse laser frequencies were bichromatic and symmetrically detuned, which emulates the situation during a MS gate sequence. The results are shown in Fig. 4.12.

We discovered that the qubit frequency shift is quadratic to the geometric mean of the two Raman beam powers which is basically the Raman Rabi frequency. Non-linear Stark shift is a characteristic of the 4-th order Stark shift [45]. It originates from the interaction of the atomic transitions and the two frequency combs that interfere at the location of the ion. Its scale changes significantly at different repetition rates or comb spacings of the pulse laser, and have been minimized in other groups by adjusting the repetition rate [95].

We also found that the microwave Ramsey curves that we took are not very consistent, with spurious jumps in the observed qubit state. This is very noticeable as shown in Fig. 4.13 and gets worse for longer wait time. The presented data is the average of five runs of the same Ramsey sequence, which were taken over a period of $2 \sim 3$ minutes. The vertical error bars result from run-to-run deviation of the measured qubit state, which should not be present under a static Stark shift. The rather slow rate at which the size of the Stark shift changes is roughly in the same time scale as the beam pointing or phase fluctuation due to air current. We think the 4-th order Stark shift changes the qubit frequency, and its magnitude changes in time due to beam path fluctuation which may affect how the frequency combs interfere.

We do not have a definitive proof for this yet, but measuring how a co-propagating pair of Raman beams affect the qubit coherence will be useful in determining its cause. In this configuration, the two beam physically overlap

and phase fluctuation is canceled out. If co-propagating 4-th order Stark shift turns out to be much more consistent, that we can conclude that making the beam phases more stable by means such as high-power UV fibers for pulse laser will lower the decoherence rate.

In order to estimate how much the heating rate, motional decoherence and Stark shift fluctuation contributes to the observed gate infidelity, we ran a numerical simulation of the qubit state time evolution under MS Hamiltonian. We used QuTip(Quantum Toolbox in Python), specifically its mesolve() method, to solve the Lindblad master equation. We first verified that the simulation adequately explains the system by comparing a single qubit time evolution under SDF to its simulation. We compared the measured qubit state to the simulation at $t = N * 2\pi/\delta$, multiples of the time it takes for the ion to make a single loop in phase space. At these values of t, the ideal spin state is $|0\rangle$ because the wave packet periodically returns to the origin. Also, we varied the coherence time of the motional state by changing the gain of the trap power PID system, and the numerical simulation was run with different motional decoherence rates. The results are shown in Fig. 4.14 and shows excellent agreement between experiment and numerical simulation. The difference between the experimentally measured residual spin-motion entanglement values(excess $|1\rangle$ population) and their numerical simulation is 0.49 % on average and 1.82 % at maximum. We also ran simulations with 25 % underestimated and overestimated motional decoherence rates and confirmed that the residual entanglement is overestimated and underestimated accordingly.

After confirming that the Lindblad master equation with the known sources of decoherence correctly explains the experimental imperfections, we moved on to simulate MS interaction. The simulation takes a much longer time because

the dimension of the Hilbert space increases by at least 20 times. This is because we have to take into account another spin(2x) and another motional mode with up to 10 phonons(10x). As a result, the size of the matrix increases by 20^2. Each simulation takes between $1 \sim 2$ hours even after optimization. The results are summarized in Table 4.1.

	Value	Contribution
Heating Rate	6.97±3.95Hz	0.00%
Motional Decoherence	194.1±34.85Hz	0.70%
I^2 Decoherence	330Hz	1.30%
Average readout error	(0.29%+0.65%)/2=0.47%	1.41%
Gate parameter error	$\Omega_{ion1}, \Omega_{ion2}, t_g, \delta_g, t_{\pi/2}$	3.39%

Table 4.1: Identified sources of MS gate infidelity

The biggest offender revealed by MS gate error analysis is gate parameter error. Its contribution to infidelity is calculated by subtracting errors due to known sources from the total infidelity. The rather high contribution can be understood as a consequence of the fact that we have to drive both the cm and tilt modes simultaneously. When only a single mode is excited, the gate time is given as $t_g = 2\pi/\delta$, and can be found by a single scan. This corresponds to choosing any point on a line in the parameter space of gate time and detuning. However, in our case we have to search for the right point in it. Finding the right gate parameters can be made easier by the use of pulse modulation as it will make the gate operation less sensitive to gate parameters. We note that the MS gate results presented here was obtained only by unmodulated, constant gate pulses. Utilizing even the simplest form of pulse shaping such as Walsh pulses may increase gate fidelity significantly.

The second largest contribution to infidelity comes from readout error. The detection laser is currently locked to a wavemeter with software PID control.

Naturally, the bandwidth of the PID loop is very low, and the laser frequency fluctuates between ± 10 MHz of the lock point. Also, its intensity is not stabilized. The fluctuation in frequency and intensity of the detection laser decreases the accuracy of histogram fitting. Therefore locking the laser to a ULE cavity and employing intensity stabilization will help. Also, we think we can get a slightly improved result by moving on to a PMT array detection system where we can use threshold method with each qubit instead of histogram fitting.

The third biggest contribution comes from "I^2" decoherence which is probably due to fluctuating 4-th order Stark shift. It can be reduced by improving beam path shielding or sending the pulse lasers through a UV fiber. One can also consider modifying the pulse laser so that we can control the repetition rate, which can then tuned to minimize 4-th order Stark shift.

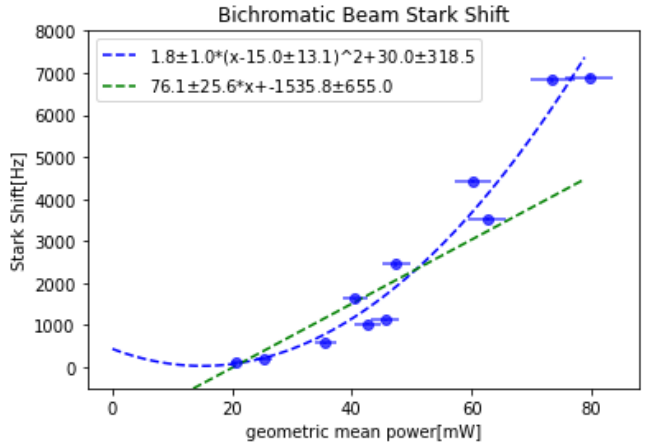

(a)

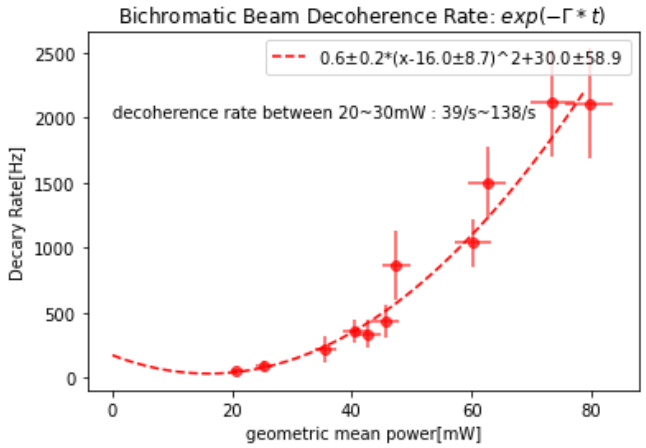

(b)

Figure 4.12: (a) The change in the qubit frequency in the presence of off resonant, bichromatic pulse laser beams. Horizontal error bars are calculated from the accuracy of the power meter we used to measure beam powers. The blue dashed line is a fit to a quadratic model, while the green is a fit to a linear model. We observe a quadratic dependence of the Stark shift to the geometric mean of the beam powers, which hints that it is a 4-th order Stark shift. (b) The decoherence rate of the qubit state as a function of the beam power. It is also quadratic to the applied beam power. Vertical error bars are the standard errors in decoherence rate estimated from fitting the Ramsey data.

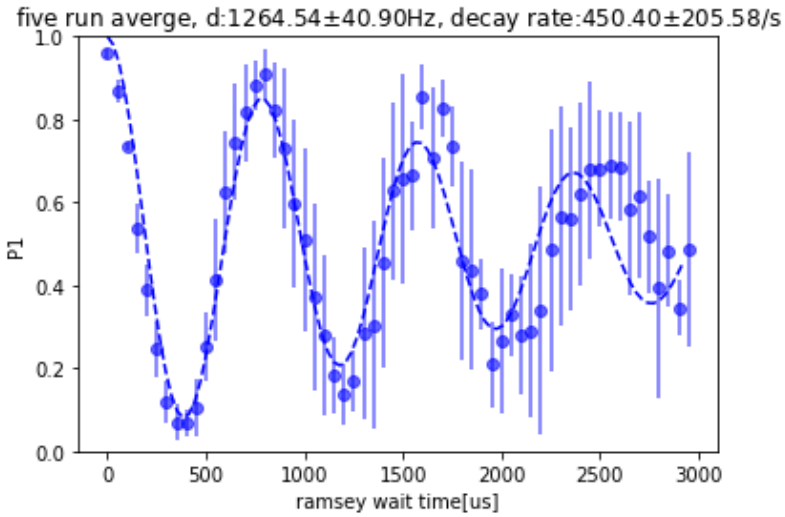

Figure 4.13: The microwave is set to be resonant with the qubit transition, and a Ramsey sequence was run with the detuned pulse laser beams turned on. The qubit frequency is shifted due to Stark shift. Its magnitude fluctuates over time, which causes decoherence. The blue dashed line is a fit to an exponentially decaying sine model.

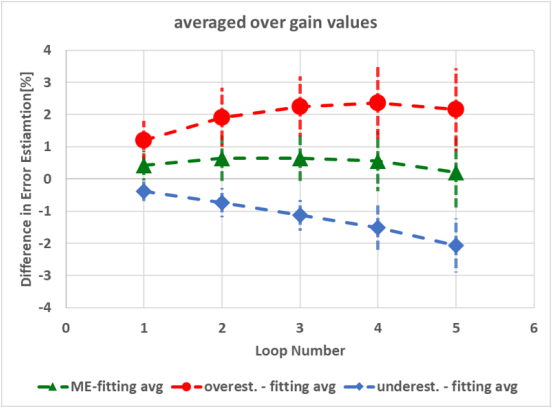

(a)

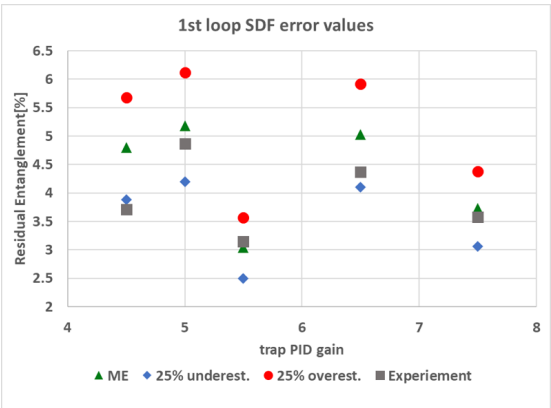

(b)

Figure 4.14: (a) The difference between the measured excess $|1\rangle$ population and numerical simulation with decoherence. The green data points are the difference between the correct master equation simulation and the experiment, while the red and blue data points use overestimated and underestimated motional decoherence rates for comparison. The error bars are the standard deviation of the data points produced from experiments with different motional decoherence rates. (b) Residual entanglement values that are experimentally measured and numerically simulated. We see an excellent agreement between experiment and simulation across a wide range of motional state coherence time.

Chapter 5

Generation and Characterization of Entangled Coherent States

The coherent state has been the focus of intense research both theoretically and experimentally because it is the most classical of quantum states. Its wave packet follows the trajectory of a classical harmonic oscillator, and its quadrature variables, such as position and momentum, have the smallest dispersion in phase space allowed by the uncertainty principle, making it as classical as possible within the boundaries of quantum mechanics. In this chapter, we will discuss its bipartite version, the two-mode entangled coherent state. We will present a brief overview of the quantum state, and show how it can be generated in our system with two-dimensional SDF that acts on both of the two radial modes of a single trapped ion and projective measurement of the spin state. Also, experimental results for its basic characterization will be discussed. Finally, we will show that two-dimensional SDF can be used to realize MS interaction with a reduced Rabi frequency requirement.

5.1 Introduction

The coherent state is a quantum analog of a classical harmonic oscillator. Its quantum superposition, the cat state, is a very interesting quantum state in that it is the quantum superposition of the most classical quantum state. Even its name originates from the famous thought experiment that highlights the paradoxical nature of quantum mechanics. The cat state has been created in various platforms such as trapped ion [42, 96, 43], and photons [97, 98, 99].

Its multipartite extension, the entangled coherent state or ECS, has also been investigated theoretically in various field including quantum sensing [31], fundamental studies of quantum mechanics [28, 29], quantum information processing [34, 33, 100, 101, 36], and quantum communication [32, 35]. The ECS plays an important role in the context of continuous variable quantum computing(CVQC) because the coherent state can be used as a continuous variable equivalent of a qubit state. Coherent states with opposite phases, $|\alpha\rangle$ and $|-\alpha\rangle$, become virtually orthogonal when $1 << \alpha$, since their overlap diminishes exponentially. This kind of "encoded" qubit states have the advantage of facilitating error detection and correction, as experimentally shown in the first demonstration of quantum error correction [37] where the authors achieved a 20 fold increase in qubit lifetime by using logical qubits encoded in coherent states and applying real time error correction. In trapped ion systems, quantum information has been encoded in a motional state called the GKP state, and its error correction protocols have been realized [38, 102]. Other examples of CVQC in trapped ion system involve number states of motion and their boson sampling [103].

In this line of research, the ECS can be seen as the entangled state of two qubits encoded in coherent states and its realization will pave the way for

expanding CVQC to higher dimensions. Entangled coherent states have been experimentally realized in photons [39] and microwave cavities coupled with a superconducting circuit [41, 40]. Although the trapped ion has often been used in experiments involving single mode cat states, the ECS has not been implemented with a trapped ion. We realized the ECS in our system by using a two-dimensional SDF and projecting the spin of the resulting state. In the remainder of this chapter, details of the experiment will be presented.

5.2 Two-dimensional spin-dependent force

Let us start by considering a two-dimensional version of the spin-dependent Hamiltonian of Eq. (4.3) in which the SDF acts on the two transverse axes, X and Y, simultaneously with different detunings:

$$\begin{aligned}\hat{H}_{SDF}(t) = &\frac{\hbar\eta_X\Omega}{2}\hat{\sigma}_\phi(\hat{a_X}^\dagger e^{-i(\delta_X t+\phi')} + \hat{a_X}e^{i(\delta_X t+\phi')}) \\ &+\frac{\hbar\eta_Y\Omega}{2}\hat{\sigma}_\phi(\hat{a_Y}^\dagger e^{-i(\delta_Y t+\phi')} + \hat{a_Y}e^{i(\delta_Y t+\phi')})\end{aligned} \tag{5.1}$$

where $\eta_{X,Y}, \delta_{X,Y}$, and $\hat{a}_{X,Y}$ each represent the Lamb-Dicke parameter, symmetric detuning, and annihilation operator for the X and Y axes. In this chapter, we will use the notation $|s\rangle|a\rangle|b\rangle$ to specify the quantum state of the system, where s denotes the qubit state of the ion chain with possible values of $\uparrow$ and $\downarrow$ for a single ion and their tensor product for a chain of two ions. We switch from 0 and 1 to $\downarrow$ and $\uparrow$ for specifying the spin state to avoid confusion with the number states of motion.

Time evolution operator for Eq. (5.1) is $\hat{U}(t) = |+\rangle\langle+|\hat{D}_X(\alpha(t))\hat{D}_Y(\beta(t)) + |-\rangle\langle-|\hat{D}_X(-\alpha(t))\hat{D}_Y(-\beta(t))$ where $\hat{D}_X(\alpha(t))$ and $\hat{D}_Y(\beta(t))$ are the displacement operators defined as $e^{\alpha(t)\hat{a}_X^\dagger - \alpha(t)^*\hat{a}_X}$ and $e^{\beta(t)\hat{a}_Y^\dagger - \beta(t)^*\hat{a}_Y}$. $|\pm\rangle$ are the eigen-

states of $\hat{\sigma}_\phi$. Applying this to the initial state of the ion after sideband cooling in both the X and Y axis yields:

$$|\psi(t)\rangle = \frac{1}{\sqrt{2}}(|+\rangle\,|\alpha(t)\rangle\,|\beta(t)\rangle + |-\rangle\,|-\alpha(t)\rangle\,|-\beta(t)\rangle) \tag{5.2}$$

The wavefunction evolves into a tripartite entangled state of the X and Y motion and the qubit. When we measure the qubit state of Eq. (5.2), the population of the $|\uparrow\rangle$ state, $P_\uparrow$, will be modulated at δ_X and δ_Y as the motional wave packet periodically returns to the origin in each phase space and the spin-motion entanglement disappears. Therefore, $P_\uparrow(t)$ can be expressed as follows:

$$P_\uparrow(t) = \frac{1}{2}\left(1 - e^{-\left(\bar{n}_X+\frac{1}{2}\right)|2\alpha(t)|^2-\left(\bar{n}_Y+\frac{1}{2}\right)|2\beta(t)|^2} e^{-t/\tau}\right) \tag{5.3}$$

In the above equation, $\overline{n}_{X,Y}$ represent the mean phonon number of each mode, and τ corresponds to the phenomenological decoherence time scale. We observed the time evolution of the qubit state as it is periodically entangled with the X and Y modes. This experiment was repeated at various ratios of X and Y detunings, defined as $R = \delta_X/\delta_Y$. Fig. 5.1 shows four data sets, each corresponding to a different value of R. We set the detuning to be between the X and Y mode frequencies, thus $R < 0$. The red and blue vertical lines each represent moments when the Y and X mode return to the origin. When only a single mode has returned, the spin is still entangled with the other mode and this results in a non-zero but decreased $P_\uparrow$. When both motional modes disentangle from the spin, it fully returns to its original state $|\downarrow\rangle$. Blue curves are fits to Eq. (5.3), and it aligns with the data points nicely.

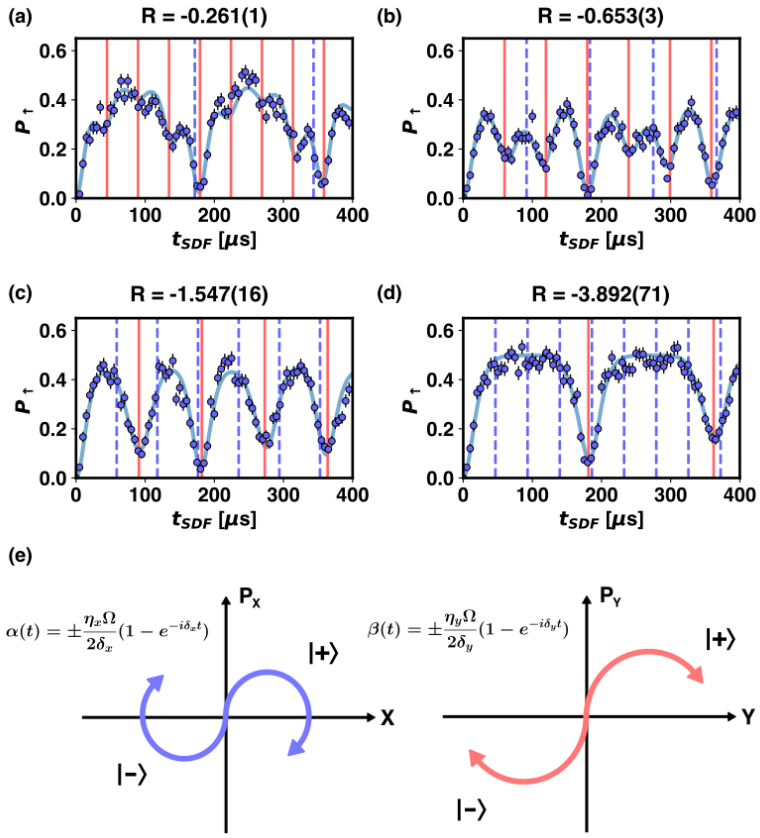

Figure 5.1: Red lines represent when the Y mode returns to the origin in its phase space. Blue dashed lines are when the X mode motion returns to the origin. Since $\delta_X \neq \delta_Y$, the X and Y modes entangle and disentangle with the spin at different periods. When they are both disentangled, the spin returns to its original state, $|\downarrow\rangle$. Titles of each subfigure shows R measured by fitting and its standard error. Error bars are quantum projection noise. The bottom row shows a schematic diagram of how the wavepackets evolve in time in each phase space.

While Eq. (5.3) explains the experimental results in Fig. 5.1, the generated quantum state is a tripartite entangled state where the qubit is entangled with the X and Y motion. We turn on the detection beam for 500 μs and then post-selected data sets with photon counts less than 2. This projects the qubit to $|\downarrow\rangle$, so that the wave function becomes:

$$|\psi_{ECS}(t)\rangle = |\downarrow\rangle \frac{|\alpha(t)\rangle |\beta(t)\rangle + |-\alpha(t)\rangle |-\beta(t)\rangle}{\sqrt{2 + 2e^{-2(|\alpha(t)|^2+|\beta(t)|^2)}}} \tag{5.4}$$

The detection time and threshold was chosen to select the $|\downarrow\rangle$ state with high fidelity; the longer you shine the detection beam and the lower your threshold is, the less likely the $|\uparrow\rangle$ is selected. Eq. (5.4) is an entangled coherent state of the X and Y motion, with the now disentangled spin in the $|\downarrow\rangle$ state. If we chose to project the spin state to $|\uparrow\rangle$, we would end up with an odd cat state. However, the resulting wave function is heavily decohered because it had scattered many photons.

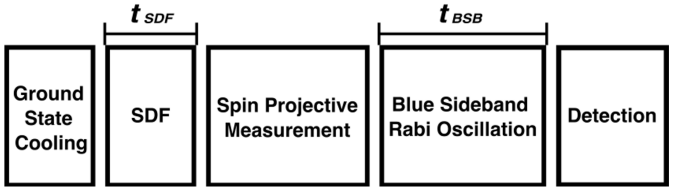

Figure 5.2: The ion's quantum state is initialized to $|\downarrow\rangle |0\rangle |0\rangle$ by optical pumping and ground state cooling. The SDF(1D or 2D) is applied for t_{SDF}. We then detect the spin state, and post-select $|\downarrow\rangle$. We drive the blue sideband Rabi oscillation on the Y mode. We use Eq. (5.5) to obtain Y mode population distribution.

5.3 Population extraction with blue sideband Rabi oscillation

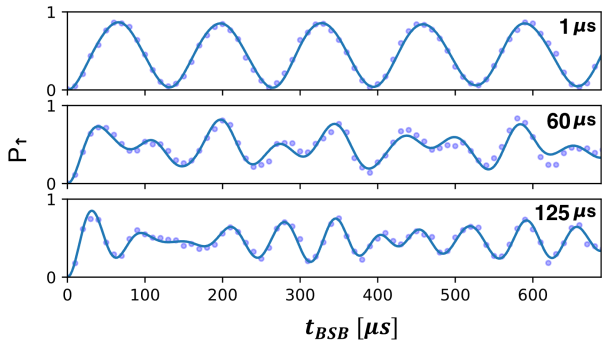

(a)

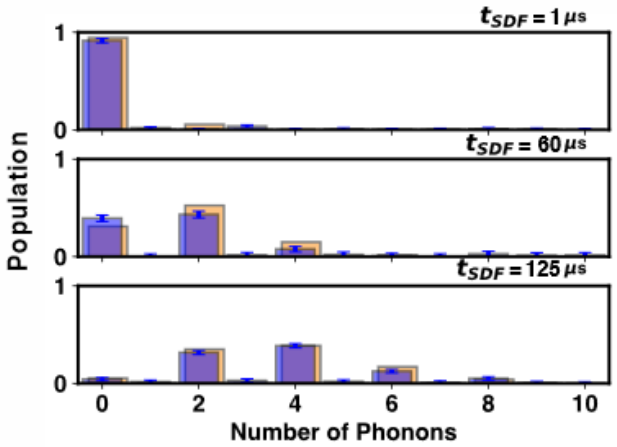

(b)

Figure 5.3: (a) Blue sideband Rabi oscillation after applying Y mode SDF for varying amounts of time. The revival of Rabi oscillation occurs later when the SDF is applied for a longer amount of time. Solid lines are generated by fitting the data to Eq. (5.5). (b) Population distribution inferred from (a). The orange bars represent the expected population for an ideal 1D even cat state. The blue bars are the experimentally measured population, and they show good agreement.

We characterize the generated state by observing how the phonon number distribution in the Y mode changes with t_{SDF}, duration of the two-dimensional spin-dependent force. This is done by driving the Y mode blue sideband transition [43, 91, 104, 44]. The blue sideband Rabi frequency is given as $\Omega_{n+1,n} = \Omega_{0,0} \langle n+1| e^{i\eta_Y(\hat{a}_Y^\dagger + \hat{a}_Y)} |n\rangle = \Omega_{0,0} exp\big(-\eta_Y^2/2\big)\eta_Y/\sqrt{n+1}\ L_n^1(\eta_Y^2)$, which is a function of the starting phonon number n. $\Omega_{0,0}$ is the carrier transition Rabi frequency. Therefore, one can fit the observed blue sideband Rabi oscillation to the following model to extract phonon number distribution of the generated state:

$$P_\uparrow(t_{BSB}) = \sum_{n=0}^{N} \frac{p_{Y,n}(t_{SDF})}{2} \left(1 - \cos\left(\Omega_{n+1,n} t_{BSB}\right) e^{-t_{BSB}/\tau}\right) \tag{5.5}$$

We first applied the blue sideband spectroscopy to a single mode cat state, which is created by a projective spin measurement of a spin-motion entangled state [43]. The results are shown in Fig. 5.3.

Fig. 5.3(a) shows the blue sideband Rabi oscillation results for various t_{SDF}. The data matches Eq. (5.5), and we can clearly see that the revival of Rabi oscillation is pushed back as t_{SDF}, hence the magnitude of displacement, becomes larger. Fig. 5.3(b) shows the population distribution extracted from each of the blue sideband Rabi oscillation data. Almost all population is concentrated in the even states, as expected of a single mode even cat state [43]. The evenness and oddness of the population distribution can be characterized by its parity which is defined as $\Pi(t) = \sum_n (-1)^n p_{Y,n}(t)$. For an even number cat state such as the one presented in Fig. 5.3, $\Pi \simeq 1$.

We can observe the blue sideband Rabi oscillation of the X mode, but since

η_Y is about twice as large as η_X, at displacement the Y mode couples to spin strongly and affects the blue sideband oscillation of the X mode. The interference between the two modes can be suppressed by reducing the Rabi frequency, but that makes the probe time longer. Due to our limited motional coherence time (5 ms in the ground state), reducing the Rabi frequency enough to observe the X mode was not possible. Also, reduced Rabi frequency means that our measurement results are more susceptible to secular frequency drift, which causes the fitting algorithm to mistakenly identify high phonon number populations. A more stable secular frequency and longer motional coherence time will enable such measurements.

5.4 Phonon distribution of entangled coherent state

If we measure the single mode phonon number parity of an entangled coherent state, the result will be less than unity because it is entangled with another mode and the single mode density matrix will be that of a mixed state. It is shown calculating the population distribution as follows:

$$\begin{aligned} p_{Y,n}(t) &= Tr(\{|\downarrow\rangle\langle\downarrow| \otimes \hat{I}_X \otimes |n\rangle\langle n|\} |\psi_{ECS}\rangle\langle\psi_{ECS}|) \\ &= \frac{e^{-|\beta(t)|^2}(|\beta(t)|^{2n}/n!)}{1+e^{-2\left(|\alpha(t)|^2+|\beta(t)|^2\right)}}(1+(-1)^n e^{-2|\alpha(t)|^2}) \end{aligned} \tag{5.6}$$

where $\alpha(t)$ and $\beta(t)$ denote the displacement of the X and Y mode at time t, respectively. When $\alpha = 0$, the wave function in Eq. (5.4) is reduced to a single-mode cat state of the Y mode ($|\psi_Y(t)\rangle = |\downarrow\rangle(|\beta(t)\rangle + |-\beta(t)\rangle)/\sqrt{2+2e^{-2|\beta(t)|^2}}$) and the phonon population is expected to be only in the even number states. However, for a non-zero α, the interference between the two coherent states with opposite phases in the Y phase space, $|\beta\rangle$ and $|-\beta\rangle$, is suppressed by the

motion in the X-axis, $|\alpha\rangle$ and $|-\alpha\rangle$. Consequently, the parity of the Y mode population is modulated as the size of the displacement in the X mode changes.

The effect of non-zero temperatures should be considered as well because it directly affects the observed parity. For example, if we have some population left in the $|1\rangle$ state of the Y mode, $p_{Y,1}$, the parity will decrease by $2p_{Y,1}$ since the $|1\rangle$ is an odd state. We construct our model to be a weighted sum of the following three cases.

- $|1\rangle_X |0\rangle_Y$ with probability of $p_{X,1}(1-p_{Y,1})$
- $|0\rangle_X |1\rangle_Y$ with probability of $(1-p_{X,1})p_{Y,1}$
- $|0\rangle_X |0\rangle_Y$ with probability $(1-p_{X,1})(1-p_{Y,1})$

The $|1\rangle|1\rangle$ state will not be considered since its probability is much lower than the three cases above. For the first case, the population distribution of the Y mode, $p_{Y,n}$, can be expressed using the number state representation of the displacement operator, $d^{\alpha}_{mn} = \langle m| D(\hat{\alpha}) |n\rangle$, as follows:

$$\begin{aligned} p_{Y,n}(t) = & \frac{1}{\left(1+e^{-2\left(|\alpha(t)|^2+|\beta(t)|^2\right)}\right)} e^{-|\beta(t)|^2} \frac{|\beta(t)|^{2n}}{n!} \\ & \times \left(1+(-1)^n \frac{\left(d_{11}^{-2\alpha}+d_{11}^{2\alpha}\right)}{2}\right) \end{aligned} \tag{5.7}$$

For the second case with the initial quantum state of $|0\rangle_X |1\rangle_Y$, the population distribution is given as:

$$\begin{aligned} p_{Y,n}(t) = & \frac{1}{2\left(1+e^{-2\left(|\alpha(t)|^2+|\beta(t)|^2\right)}\right)} \\ \times & \left(\left|d_{n1}^{\beta}\right|^2 + \left|d_{n1}^{-\beta}\right|^2 + \left(\left(d_{n1}^{\beta}\right)^* d_{n1}^{-\beta} + d_{n1}^{\beta}\left(d_{n1}^{-\beta}\right)^*\right) e^{-2|\alpha|^2}\right) \end{aligned} \tag{5.8}$$

d^{α}_{mn} is calculated by referring to [105].

The third case results in a population distribution given by Eq. (5.6). We use the weighted sum of the three distributions with weights given by the respective probabilities to fit the parity modulation data with $\Omega, p_{X,1}$ and $p_{Y,1}$ as floated parameters.

We demonstrate the generation of entangled coherent states at two values of $R = \delta_X/\delta_Y$. The left figure in Fig. 5.4(a) corresponds to $R = -2$, where the ion is periodically displaced in the X axis at a frequency which is twice of the frequency of the periodic displacement in the Y axis. Therefore, according to Eq. (5.6), the parity of the phonon distribution of the Y motion is expected to be modulated at half the period of its periodic displacement.

We repeat the same experiment with $R = -2/3$ as shown in the right panel of the same figure. In this case, the parity modulation pattern is expected to span three periods of the Y displacement. The observed variation in phonon number parity is in good agreement with the theoretical model, and is a direct consequence of the entanglement of the two motional modes. The plots in Fig. 5.4(b) are the two representative phonon distributions. The Y mode displacement is maximum for both, but the phonon number parity is 0.89 ± 0.09 for the left panel and 0.22 ± 0.06 for the right. Also, the right panel shows a clear deviation from the single-mode cat state phonon distribution with a significant population in the $|1\rangle_Y$ and $|3\rangle_Y$ states. In Fig. 5.4(a), we also plotted the time evolution of the mean phonon numbers of the Y mode, which approximately corresponds to the square of the absolute value of the displacement in the Y mode phase space. The theoretical curves for the mean phonon numbers of the X and Y modes are calculated by using the Rabi frequency and 1-phonon state population of each mode inferred by fitting the phonon number parity data.

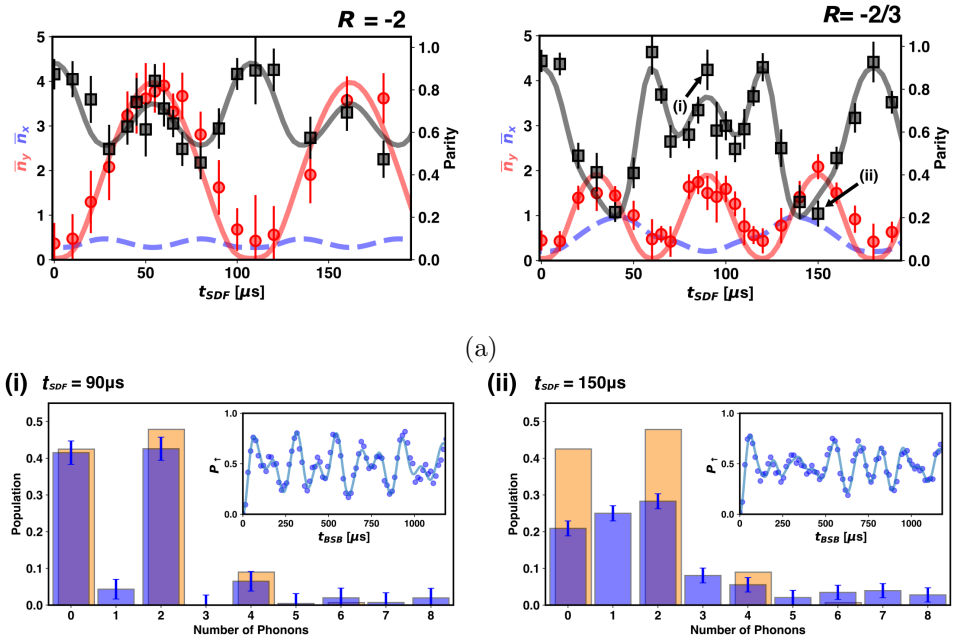

Figure 5.4: (b) Change in Y mode parity as a function of t_{SDF}. The SDF detuning ratio $R = \delta_X/\delta_Y = 2$. The black data points represent Y mode parity, while the red data points show the mean phonon numbers, both obtained from the population distribution. The black lines are fits to the ECS parity model, constructed by combining Eq. (5.6), Eq. (5.8) and Eq. (5.7). The red and blue lines are the X and Y mode mean phonon numbers expected from the parity fit and not fitted values themselves. Error bars are calculated from the standard errors in population fitting. (a) Y mode population distribution at two values of t_{SDF} with $R = -2/3$ indicated as (i) and (ii) in Fig. 5.4(a). The orange bars are the expected population for a single mode cat state, and the blue bars are the experimentally extracted population. The insets show the blue sideband Rabi oscillation for each population distribution.

We use the near-degeneracy of the radial modes of linear Paul trap to drive the two motional modes of a single ion simultaneously with detuned SDF. It does not require second order interactions as proposed in [106, 107], and is therefore advantageous in terms of interaction strength. After generating entangled coherent states, we observed a periodic modulation in phonon number parity. This is a direct consequence of the entanglement between the two phonon modes and nicely agrees with theoretical expectations. The periodic reduction in parity is analogous to the decoherence of the spin state in a spin-motion entangled system [49].

The size of the displacements generated in the experiment is mainly limited by two factors. The first is the large Rabi frequency needed to generate a strong SDF in both X and Y modes. For a SDF with non-zero detuning, the maximum displacement is limited because the phase space trajectory forms a circle whose radius is proportional to the inverse of the detuning. Thus, the maximum displacement can be increased by making the radial mode frequencies closer. Another solution is to apply a SDF resonant to both the X and Y modes, which can be realized by a tetrachromatic laser beam [108]. With this scheme, the size of the displacement will increase linearly with t_{SDF} and the coupling of the laser to each mode. The other factor limiting the size of displacement is the difficulty of characterizing motional states with large displacements. States with larger displacement magnitude are harder to probe because the coherence time of a cat state scales inversely with the square of magnitude of displacement [109].

The creation of an entangled coherent state with opposite phase, $|\downarrow\rangle (|\alpha\rangle |\beta\rangle - |-\alpha\rangle |-\beta\rangle)$, is possible with a π-pulse phase-locked to the SDF preceding the spin state measurement [43]. Also, we note that the phase between the two terms in Eq. (5.4) can be set to an arbitrary value ψ by setting the initial

qubit state to $|+\rangle + e^{i\psi}|-\rangle$ prior to the application of the two-dimensional SDF. Additionally, using our scheme, up to $3N$ modes can be entangled for an N-ion chain when all the principal axes of the trapping potential are utilized. Especially, the generation of a tripartite entangled coherent state of the X, Y and Z modes, combined with a beam splitter interaction between the phonon modes [44, 110, 111], will enable the quantum teleportation protocol in Ref. [35] with a single trapped ion. Also, entangling coherent states with opposite phases is equivalent to a two qubit gate for qubit states encoded in coherent states [38, 37]. Therefore it can be used as a building block for digital quantum computation with encoded qubits.

There have been proposals and experiments of a Ramsey-type matter-wave rotation sensor [112, 113], Rabi-type sensor [114] and Rashba and Dresselhaus-type spin-orbit coupling for quantum simulation of topological insulators and Majorana fermions in which a single ion is coherently manipulated in two or more orthogonal spatial modes [115]. The coherent control of two-dimensional motion of a trapped ion demonstrated in this work can be applied to realize such experiments.

Lastly, we note that a full quantum state tomography(QST) or its equivalent is needed for the complete characterization of the entangled coherent state generated using our scheme. A full QST should take place in a four-dimensional space spanned by the X and Y displacements α' and β' [39, 41], but takes a prohibitively long time due to the slow quantum operations in trapped ions. Additionally, the reconstruction of Wigner function, which is a prerequisite for QST, requires the implementation of a joint parity operator which measures the parity of the joint phonon number distribution. It basically corresponds to calculating phonon number parity without discriminating the two entangled

modes. The authors of the microwave cavity experiment presented in [41] were able to implement it, but to the best of our knowledge no such operation was realized with trapped ions. A less complete characterization may be possible by creating interference between the X and Y mode with beam splitter interaction [44, 110].

5.5 Molmer-Sorensen gate with two-dimensional spin-dependent force

In a related experiment, we trap two ions in a linear chain and drive two-dimensional SDF with their collective motional modes. Here, we interact with four closely spaced motional modes instead of two, as shown in Fig. 5.5

First, we observe the time evolution of two-qubit states when subjected to a two-dimensional Mølmer–Sørensen interaction. We set the detuning and Rabi

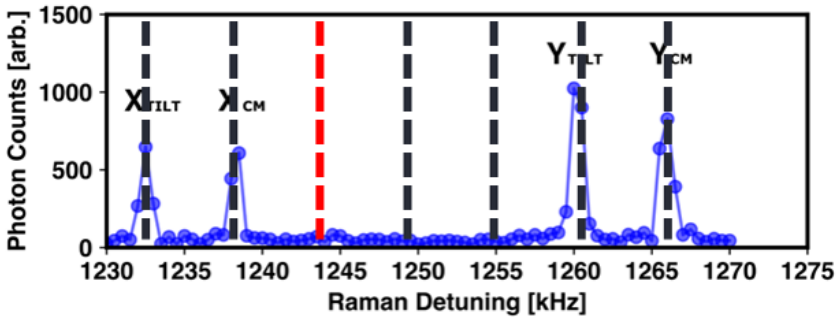

Figure 5.5: Blue sideband spectrum of a two ion chain. Due to the close spacing between the X and Y modes, all of the four transverse modes can be driven by a single laser frequency. A constant pulse MS gate can be implemented by positioning the laser detuning at the black dashed lines. At these detunings, we can find a time at which the wave packets in all four modes return to the origin. The red line indicates the detuning where the X modes and Y modes contribute equally to the required geometric phase.

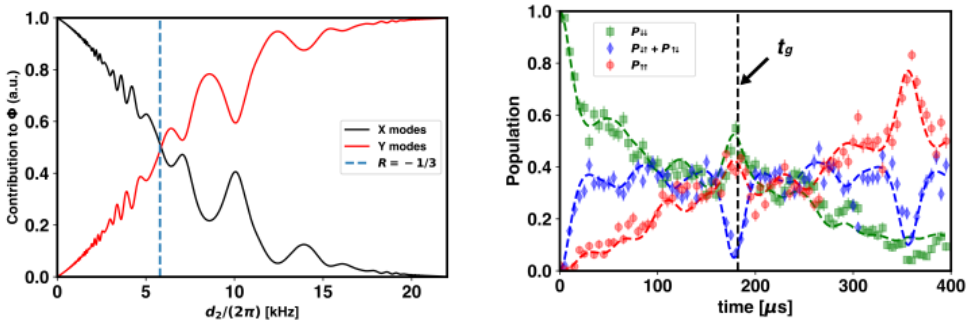

(a) (b)

Figure 5.6: (a) Geometric phase contribution of each principal axis. The dashed line indicates the detuning when $R = \delta_{X_{cm}}/\delta_{Y_{tilt}} = -1/3$. (b) Time evolution of the two-qubit states under two-dimensional MS interaction when $R = -1/3$. The gate time we used for the Bell state generation and fidelity measurement is indicated with an arrow. It is slightly different from the minimum of odd population because we iteratively optimized gate parameters after observing time evolution. Curves are obtained by fitting the data to Eq. (5.9)

frequency for the generation a Bell state of the form $(1/\sqrt{2}(|\uparrow\uparrow\rangle + |\downarrow\downarrow\rangle))$. We implemented the MS gate at $R = -1/3$, which is now defined as $\delta_{X_{cm}}/\delta_{Y_{tilt}}$. The position of the laser detuning for $R = -1/3$ is shown as the red line in Fig. 5.5. We chose to demonstrate the two-dimensional MS gate at $R = -1/3$ because at this value the X and Y modes contribute to the required geometric phase almost equally and the two-dimensional nature of the operation is most pronounced. The time evolution of the two-qubit states are shown in Fig. 5.6(b). Subsequently, we estimated the fidelity of the resulting state by examining the oscillation of qubit state parity. For this measurement, we followed the standard protocol and applied a $\pi/2$-pulse on both qubits and varied its phase. In these experiments, we have more phase space trajectories to close, and we are more constrained in our choice of gate parameters. We optimized factors such as the spacing between motional modes by fine-tuning various trap electrode voltages.

The populations of the qubit states in a two-ion chain evolve under Mølmer–Sørensen interaction with four motional states as follows [60]:

$$
\begin{aligned}
P_{\downarrow\uparrow}(t) = P_{\uparrow\downarrow}(t) = \frac{1}{8}(2 - e^{-8\left((\overline{n}_1+\frac{1}{2})|\alpha_1(t)|^2+(\overline{n}_3+\frac{1}{2})|\alpha_3(t)|^2\right)} \\
-e^{-8\left((\overline{n}_2+\frac{1}{2})|\alpha_2(t)|^2+(\overline{n}_4+\frac{1}{2})|\alpha_4(t)|^2\right)}) \\
P_{\downarrow\downarrow}(t) = \frac{1}{8}(2 + e^{-8\left((\overline{n}_1+\frac{1}{2})|\alpha_1(t)|^2+(\overline{n}_3+\frac{1}{2})|\alpha_3(t)|^2\right)} + e^{-8\left((\overline{n}_2+\frac{1}{2})|\alpha_2(t)|^2+(\overline{n}_4+\frac{1}{2})|\alpha_4(t)|^2\right)} \\
+4\cos\left(4\Phi(t)\right) e^{-2((\overline{n}_1+\frac{1}{2})|\alpha_1(t)|^2+(\overline{n}_2+\frac{1}{2})|\alpha_2(t)|^2+(\overline{n}_3+\frac{1}{2})|\alpha_3(t)|^2+(\overline{n}_4+\frac{1}{2})|\alpha_4(t)|^2)}) \\
P_{\uparrow\uparrow}(t) = \frac{1}{8}(2 + e^{-8\left((\overline{n}_1+\frac{1}{2})|\alpha_1(t)|^2+(\overline{n}_3+\frac{1}{2})|\alpha_3(t)|^2\right)} + e^{-8\left((\overline{n}_2+\frac{1}{2})|\alpha_2(t)|^2+(\overline{n}_4+\frac{1}{2})|\alpha_4(t)|^2\right)} \\
-4\cos\left(4\Phi(t)\right) e^{-2((\overline{n}_1+\frac{1}{2})|\alpha_1(t)|^2+(\overline{n}_2+\frac{1}{2})|\alpha_2(t)|^2+(\overline{n}_3+\frac{1}{2})|\alpha_3(t)|^2+(\overline{n}_4+\frac{1}{2})|\alpha_4(t)|^2)})
\end{aligned}
\tag{5.9}
$$

The geometric phase is:

$$
\Phi\left(t\right) = \sum_{i=1}^{4} \frac{\eta_{i1}\eta_{i2}}{(2d_i)^2}\left(d_i t - \sin\left(d_i t\right)\right)\Omega_0^2 \tag{5.10}
$$

In the above equations, $i = 1, 2, 3$ and 4 is the index for the motional modes participating in the interaction corresponding to $X_{tilt}, X_{cm}, Y_{tilt}$ and Y_{cm} mode, respectively. $\alpha_i(t)$ is the phase space displacement of the i-th motional mode at time t, η_{ik} is the Lamb-Dicke factor for the i-th mode and the k-th ion, d_i is the laser detuning, $\overline{n}_i$ is the mean phonon number, and Ω_0 is the Rabi frequency. The above formulae were derived by following the calculations presented in [116]. These equations were used to analyze and derive the results about Mølmer–Sørensen interaction in Fig. 5.6(b).

We estimated a gate fidelity of 89.7 ± 0.6 % from the spin parity oscillation and separate population measurement. It is comparable to our single axis Mølmer–Sørensen gate fidelity, 93.2±0.6 %. This indicates that Mølmer–Sørensen interaction can be expanded into multiple dimensions naturally. We attribute

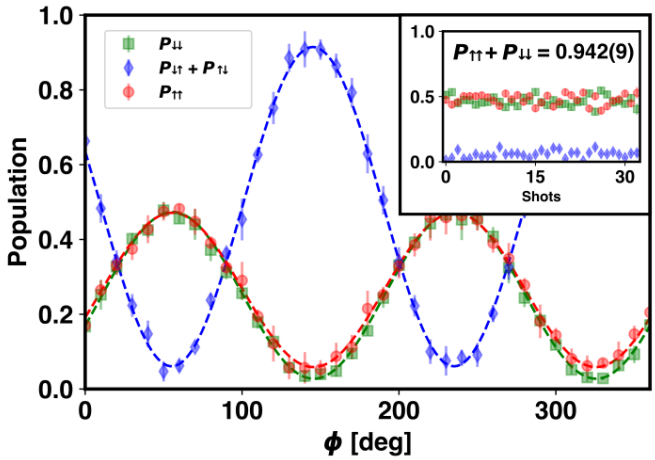

Figure 5.7: Parity oscillation of Bell state generated by two-dimensional MS interaction. The inset shows population measurement results. The estimated fidelity is 89.7 ± 0.6 %

the extra infidelity of about 3 % to residual spin-motion coupling that originates from the need to calibrate the mode spacing and gate parameters with four motional modes. We were unable to run numerical simulations to estimate error budget as was done in Table 4.1 because the computing time was prohibitively large. Now that we have to deal with four motional modes, the dimension of the matricies increases by a factor of 100, resulting in a significant increase in computing time. Perhaps a more analytic approach such as presented in [14] can be used for error estimation.

Also, we experimentally prove that the gate Rabi frequency is reduced compared to the single axis case, because more phase spaces contribute to the geometric phase as can be seen in Fig. 5.6(a). At $R = -1/3$, this effect becomes most pronounced because the geometric phase contribution is similar for both axes. As a consequence, required Rabi frequency is decreased approximately by a factor of $\simeq 1/\sqrt{2}$. The required Rabi frequency when using both axes is

estimated to be$2\pi \times 81.3 \pm 0.6$ kHz from fitting Fig. 5.6(b) to the theoretical time evolution formulae in Eq. (5.9). This is 28.3% lower compared to the X mode MS gate, and 30.1% lower compared to using only the Y axis, assuming the same gate time and gate detuning.

Using multiple principal axes for Molmer-Sorensen gate has several advantages. First, the required Rabi frequency is reduced. Using weak laser beams is preferable for a number of technical reasons, such as decrease Stark shift, ease of using fibers, and less charging of the trap. The last is a serious issue in surface traps due to the proximity of the ion to the trap surface [117, 118, 119]. Additionally, in other setups significant efforts are dedicated so as to prevent the control laser from interacting with more than one axis. This is done by either making the trap geometry highly anisotropic so that the secular frequencies are very degenerate [120], or by setting up the qubit control beam direction to be orthogonal to one of the principal axes. One can also rotate the principal axes by applying additional DC fields, but in most cases this requires a surface trap with an array of electrodes. Macroscopic traps such as ours do not have this capability. Therefore, utilizing interaction with multiple axes can be beneficial for minimizing the setup which may be necessary for the commercialization and scaling up of trapped ion quantum computation systems [121].

Chapter 6

Outlook

In this chapter, I will first discuss a list of upgrades that are being prepared or planned in order to scale the system up to five qubits. It includes individual detection with a fiber array, individual addressing of the ions with a pair of acousto-optic deflectors(AOD's). These elements are necessary for the implementation of quantum algorithms in our system.

I will also discuss a possible experiment to directly observe the coherent interaction between the two components of the entangled coherent state. This experiment will be based on the beam splitter interaction between the two modes, but we will employ a stroboscopic probe beam to track the time dependent phase between the two coherent states.

6.1 Individual detection

For individual detection with minimal crosstalk, we need a high quality imaging system that is capable of producing an image of the ion chain at the position of the imaging device, such as an EMCCD or a fiber array. We are going to use a linear array of fibers from Fibertech-Optica. Several groups have used fiber arrays for individual detection of ion qubits [19, 20, 21]. These fibers are then connected to individual PMT's. The design of the new imaging system is shown in Fig. 6.1.

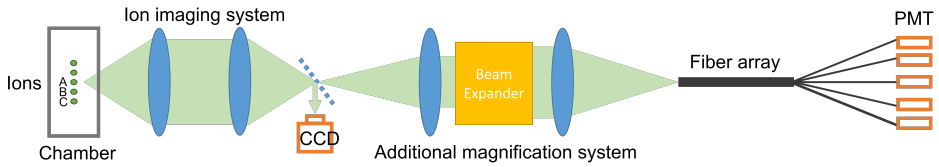

Figure 6.1: Ion chain is imaged by the first stage(M1) of the imaging system with magnification of 8. The image is transferred again to the plane of the fiber array with a variable magnification (M2).

The final image of the ion is nearly diffraction limited, and base on Zemax simulation we expect more than 99.5 % of the image of a single ion will fall onto the corresponding fiber core. This means less than 0.1 % of crosstalk between ions. The ion spacing in the final image can be continuously tuned because the second imaging stage has a tunable beam expander. This will allow us to use the same imaging setup without modification should the ion spacing changes.

The design is expected to be able to accommodate up to five ions with less than 0.1 % of detection crosstalk with the current ion spacing which is 13.8 μm. The individual detection system was designed by Jaeun Kim under my supervision.

The Fig. 6.2(a) is the actual ion chain observed by a CCD camera with a

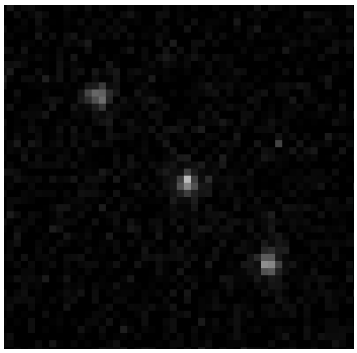

(a)

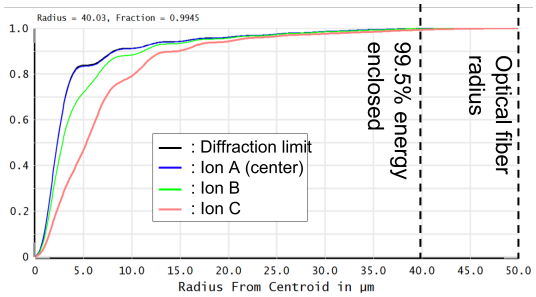

(b)

Figure 6.2: (a)A 3-ion chain is imaged by a CCD after being magnified by the two stage imaging system. The magnification of the beam expander is 1.25, and the resulting ion image spacing is about 126μm, almost identical to the smaller pitch of the fiber array. (b) Over 99.5 % of the optical power emitted by a single ion anywhere in a five ion chain arrives at corresponding multimode fiber of the fiber array.

pixel size of 7.5μm by 7.5μm (Sentech, STC-MB33USB) after M2. The image of the ion has a Gaussian radius of about two pixels, which corresponds to $10 \sim 20\mu$m. When the beam expander is set to a magnification of 1.25, the ion spacing in the image is about 126μm. This matches the smaller pitch of the custom fiber array, and we expect the ions to be individually imaged by each fiber core.

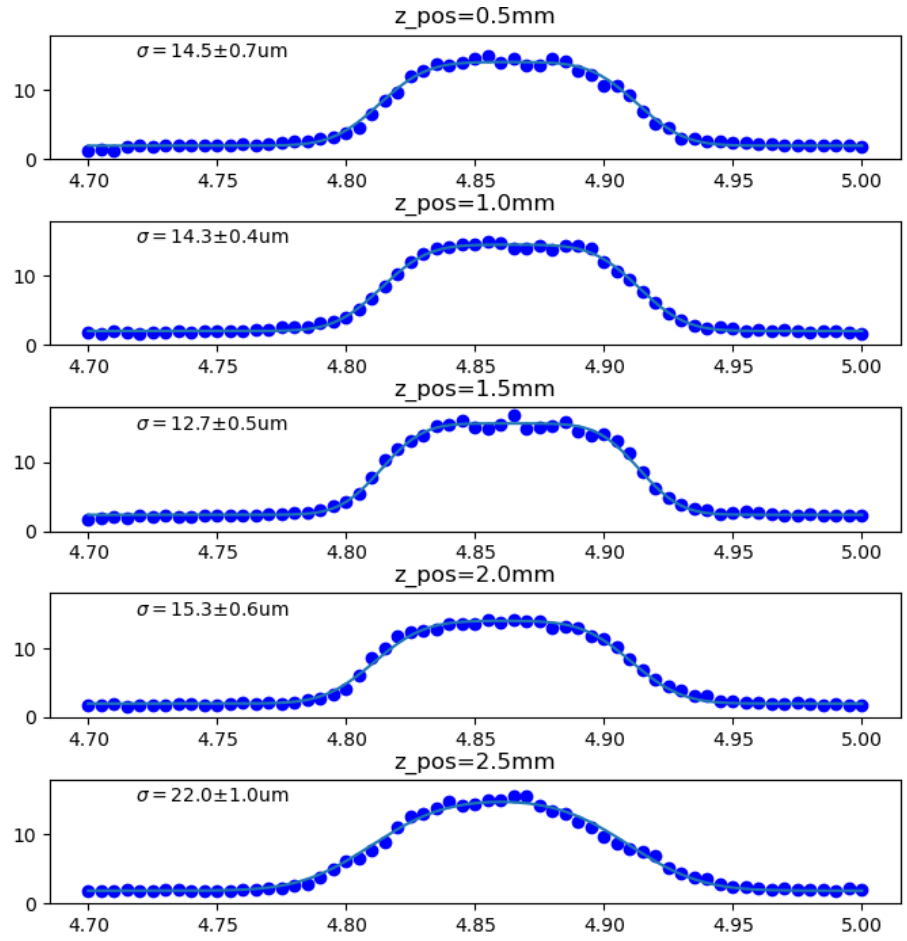

Figure 6.3: Fluorescence of a single ion was measured as the fiber array is scanned horizontally. The PMT is connected to the third fiber, which is at the center of the 127 μm spacing fiber array region. The radius of the ion image can be directly inferred by deconvoluting the measured fluorescence change.

Fig. 6.3 is the result of measuring the fluorescence of a single trapped ion with the PMT connected to fiber core 3. Since only the photons that fall into the fiber core, whose radius is $R = 50\mu$m, are collected, we can think of the situation as the convolution of the Gaussian intensity distribution of the ion image and a circular well with radius R. However, the two-dimensional integral does not have a known definite integral. Therefore, we approximate the situation to one dimension and calculate the following integral:

$$\begin{aligned} N(x, A, \sigma) &= \int_{-R}^{R} rect(\frac{x' - x}{2R}) \frac{A}{\sigma\sqrt{2\pi}} e^{-(x'-x)^2/2\sigma^2} \\ &= \frac{A}{\sqrt{\pi}}[erf(\frac{x+R}{\sqrt{2}\sigma}) - erf(\frac{x-R}{\sqrt{2}\sigma})] \end{aligned} \tag{6.1}$$

where x, A and σ are the position of the center of the fiber core, maximum value of photon counts, and the spread of the ion image on the fiber surface plane assuming a Gaussian distribution. By fitting the fluorescence scan results to Eq. (6.1), we can estimate the size of the ion image. We see that the ion's image is smallest when $z = 1.5$ mm, which corresponds to the value of the micrometer stage along the optical axis of the imaging system. We note that this analysis reduces the problem to a single dimension, an approximation which is valid when $\sigma << R$.

6.2 Individual addressing

Two popular solutions for individual ion addressing have been implemented by various groups. The first is the multichannel AOM. As the name implies, it is a linear array of AOM's that can be individually controlled [5, 20]. While it allows for a simultaneous operation of multiple qubits, the beams cannot be steered and therefore one has to align the ions to the location of the beams.

Our trap lacks the precise potential shaping capability, so we chose to use a pair of acousto-optic deflectors(AOD)(Brimrose, CQD-150-100-355) for individual control of qubits [122].

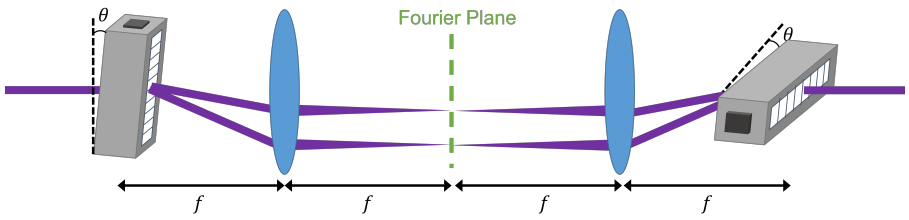

Figure 6.4: Pulse laser beam enters from the left and exits to the right where the ion chains are located.

One thing that should be considered when using AOD's for individual addressing is that the frequency of the laser beam changes as a function of its position in the ion chain. This is compensated either by a precompensation AOM or putting two AOD's in series but in an orthogonal direction, and applying the same RF frequency to them. When we use the 1st order deflection in the first AOD and the negative 1st order in the second AOD, the position dependent frequency shift is canceled, but the beam can still be steered.

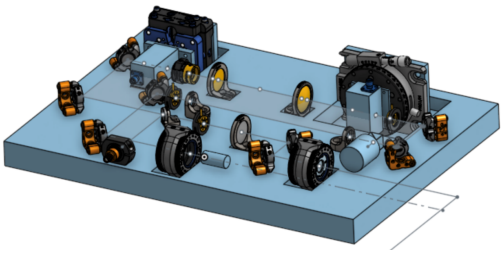

Figure 6.5: Pulse laser enters the module via a high power UV fiber. It then goes through a pair of lenses for beam size optimization and is modulated by a series of AOD's. A translatable focusing lens focuses the beam on the imaging plane of M1. M1 then images the laser beam to the ion chain.

A schematic representation of the system is presented in Fig. 6.4. The beam

will be reflected by a long-pass dichroic mirror that will be situated between M1 and M2 in the individual detection system. Zemax simulation shows that the expected spot radius is 5.5 μm at the position of the ion chain, and this value is maintained throughout the $\pm 35\mu$m of required steering range for a five ion chain. This corresponds to a 10^{-5} level of crosstalk between neighboring ions when the ion spacing is 13.8 μm. The small spot size implies that the system will be very vulnerable to the thermal drift of its optomechanical components. Therefore we have designed a fixed optics module which is watercooled and maintained at a stable temperature, similar to the 369.5 nm laser breakout board. Its preliminary CAD design is shown below. The individual addressing system was designed by Jaeun Kim under my supervision.

6.3 Stroboscopic interaction and controlled interference between two motional modes

The entangled coherent state has a major drawback that it cannot easily interact coherently with the conventional tools of trapped ion experiment. This is because the state involves two phase spaces, and in each wave packet rotates at their respective secular frequency. For the interaction between a quantum state and the laser to be coherent, their relative phase should remain constant over the duration of the experiment. In a single mode cat state, this is easily realized by setting the Raman transition to be resonant to the motional sidebands of the mode of interest. The same cannot be done for the ECS because we now have at least two modes.

Let us consider a bilinear blue sideband Rabi oscillation which is realized by driving qubit transitions simultaneously at two frequencies, ω_X and ω_Y. The resulting Hamiltonian, derived from Eq. (3.6) is:

$$\hat{H}_{X+Y} = \frac{\hbar\Omega}{2}\hat{\sigma}_+(\eta_X\hat{a}_X^\dagger + \eta_Y e^{i\psi}\hat{a}_Y^\dagger) + h.c. \tag{6.2}$$

where ψ is the phase difference between the X mode BSB laser and Y mode BSB laser which can be set by the DDS. Here, we assume that the X and Y modes are sufficiently far apart, which enables us to eliminate the cross coupling terms that oscillate at $e^{\pm i(\omega_X-\omega_Y)t}$. This Hamiltonian was utilized by the authors of [44] to observe parity oscillation of a NOON state, which is created with two motional modes of a trapped ion. They were able to coherently probe the state with Eq. (6.2) because the number state does not have dynamic phase unlike the coherent state.

Now, imagine that we apply Eq. (6.2) for a very short amount of time in a single shot experiment. In this case there should be a well define phase relation between each of mode of the ECS and the probe beams. The phase information is only erased when we average over multiple shots because the evolution of the dynamic phase of the coherent states is much faster than the experimental time scale. We may be able to overcome this issue if we shine the probe laser beams for a very short amount of time at a frequency of $\omega_Y - \omega_X$ just like a stroboscope. This fixes the phase relation between the ion's motion and the probe lasers, and in each stroboscopic cycle the wave function will evolve by a small amount in a coherent manner.

Of course, stroboscopic interaction reduces the duty cycle, $D = \tau_{ON}/(\omega_Y - \omega_X)$, of the probe operation, and the overall duration of experiment will increase by a factor of $1/D$. Thus, it will require a longer coherence time for the motional states or an increase Rabi frequency for the probe pulse. While the former requires a significant modification of the trap RF stabilization system, the latter can be achieved by moving to a wider radial mode spacing and slightly modi-

fying the pulse laser optics and RF system so that each motional mode can be separately excited. Currently, we limit the Rabi frequency for the probe pulse to under 5 kHz to prevent it from exciting the unprobed mode because the X and Y modes are very close. A non-zero τ_{ON} inevitably results in the smearing of the relative phase between the probe beam and the coherent states, thus we will need to optimize between reducing the duty cycle and increasing the phase coherence of the stroboscopic interaction.

Extracting phonon number distribution in the ψ basis is analogous to counting photon numbers in one of the output ports of a beam splitter where one of the input ports has a phase shifter which shifts the phase of the incoming mode by ψ. In this sense, Eq. (6.3) can be used to realize the joint parity operator, which is required for quantum state tomography [41].

$$\hat{H}_{BS} = \frac{\hbar\Omega\eta_X\eta_Y}{2}\hat{\sigma}_\phi(\hat{a}_X^\dagger\hat{a}_Y e^{i\psi} + \hat{a}_X\hat{a}_Y^\dagger e^{-i\psi}) \tag{6.3}$$

We can also consider a second order interaction such as Eq. (6.3). It is the beam splitter Hamiltonian, and can be realized by setting the Raman detuning to $\omega_X - \omega_Y$ and driving a bichromatic interaction [110]. The Hamiltonian rotates at the same rate as the phase difference between the X and Y mode coherent states, $\omega_X - \omega_Y$. Therefore, we can expect the Hamiltonian to act on the entangled coherent state with a well defined phase relation, enabling us to drive a beam splitter interaction with controllable phase.

This scheme also requires increasing the separation between the X and Y mode secular frequencies since at the current separation($2\pi * 28$ kHz), the beam splitter transition cannot be excited without driving the carrier transition which is much stronger.

초록

고전 컴퓨터를 이용해 양자계를 모사할 경우, 양자계의 크기가 증가함에 따라 필요한 계산의 양이 지수함수적으로 증가한다. 따라서 고전 컴퓨터를 이용한 양자계의 모사는 양자계가 아주 작을 때만 가능하다. 양자 컴퓨터는 이러한 문제를 해결하기 위해 양자적으로 작동하는 시스템으로 양자계를 좀 더 쉽게 모사하려는 시도이다. 또한 양자 컴퓨터는 고전 컴퓨터와 완전히 다른 방식으로 작동하기 때문에, 큰 수의 소인수 분해처럼 양자역학과 상관없는 몇몇 문제에 대해서도 우위를 가짐이 알려져 있어, 양자역학과 관계없는 여러 계산에도 상당한 이점을 줄 것이 기대된다. 양자컴퓨터는 안정적이고 쉽게 조작되는 양자계를 이용해 구현할 수 있다. 이온트랩은 가장 많이 사용되는 양자컴퓨터 플랫폼 중 하나이며, 포획된 이온의 스핀과 운동을 이용해 양자정보를 처리한다.

이 학위논문에서는 포획된 이온의 이차원 운동으로 벨 상태와 얽힌 결맞는 상태와 같은 다양한 양자 상태를 만드는 방법을 탐구한다. 이러한 양자상태의 구현에는 매우 안정적이고 정확히 조작되는 실험 셋업이 필요하므로, 먼저 우리가 실험에서 사용한 양자 컴퓨터 셋업의 개발에 대해 논의한다. 이온트랩 양자 컴퓨터를 이루는 진공장치, 광학계 등 각 부분에 대한 설명과 그 설계 과정이 논의될 것이다. 그 다음, 가열 속도, 다양한 종류의 결맞음 시간 같은 포획된 이온의 기본적 특성을 측정하고 분석한다. 또한 이 셋업을 이용해 보편적 양자 게이트 집합(universal quantum gate set)을 성공적으로 구현하고 그 특성에 대해 논의한다.

다음으로 이온의 이차원 운동을 양자적으로 조작하는 실험에 대해 설명한다. 슈뢰딩거의 고양이 상태를 다차원으로 확장한 것인 얽힌 결맞는 상태는 양자 측정, 양자 컴퓨팅, 양자 통신 등의 분야에서 연구되어왔으며, 부호화 된 큐비트(encoded qubit)의 연구에도 직접적인 관련이 있다. 이 양자상태는 광자와 초전도체를 이용한 실험에서 구현되었지만, 이온트랩에서는 아직까지 구현되지 않았다. 우리는 이차원 스핀 의존 힘(spin-dependent force)과 스핀상태의 측정을 통해 이온의

운동으로 이루어진 얽힌 결맞는 상태를 성공적으로 구현했다. 이후 시간에 따라 포논수의 홀짝성(phonon number parity)이 변하는 것을 관찰했고, 이를 통해 두 운동모드의 주기적 양자 얽힘에 대한 기초적 측정을 할 수 있었다.

마지막으로 우리는 이차원 스핀 의존 힘을 이용해 몰머-소렌슨 상호작용을 구현하고, 두 이온 큐비트로 벨 상태를 구현할 수 있다는 것을 보이며, 필요한 라비진동수가 줄어든다는 것을 실험적으로 증명한다.

이 연구에서는 이온트랩 양자컴퓨터를 구축하고, 이 시스템을 이용해 포획된 이온의 이차원 운동을 양자적으로 제어함으로서 큐비트 벨 상태와 얽힌 결맞은 상태를 구현할 수 있다는 것을 보였다. 특히 얽힌 결맞는 상태의 구현은, 이 양자상태가 결맞는 상태로 부호화 된 큐비트 상태의 벨 상태라는 점을 생각했을 때 더욱 중요해지며 이 연구의 결과는 부호화된 큐비트의 응용에 중요한 역할을 할 것으로 기대된다.

주요어: 포획된 이온, 양자컴퓨터, 양자계산, 얽힌 결맞는 상태, 2큐비트 게이트, 1큐비트 게이트

학번: 2015-20351

Bibliography

[1] W. Paul, Rev. Mod. Phys. **62**, 531 (1990).

[2] H. G. Dehmelt, Phys. Rev. **103**, 1125 (1956).

[3] R. P. Feynman, Int J Theor Phys **21**, 467 (1982).

[4] L. Eeckhout, IEEE Micro **37**, 4 (2017).

[5] S. Debnath, N. M. Linke, C. Figgatt, K. A. Landsman, K. Wright, and C. Monroe, Nature **536**, 63 (2016).

[6] J. Benhelm, G. Kirchmair, C. F. Roos, and R. Blatt, Nature Phys **4**, 463 (2008).

[7] J. Clarke and F. K. Wilhelm, Nature **453**, 1031 (2008).

[8] P. Jurcevic, A. Javadi-Abhari, L. S. Bishop, I. Lauer, D. F. Bogorin, M. Brink, L. Capelluto, O. Günlük, T. Itoko, N. Kanazawa, A. Kandala, G. A. Keefe, K. Krsulich, W. Landers, E. P. Lewandowski, D. T. McClure, G. Nannicini, A. Narasgond, H. M. Nayfeh, E. Pritchett, M. B. Rothwell, S. Srinivasan, N. Sundaresan, C. Wang, K. X. Wei, C. J. Wood, J.-B. Yau, E. J. Zhang, O. E. Dial, J. M. Chow, and J. M. Gambetta, Quantum Sci. Technol. **6**, 025020 (2021).

[9] J. L. O'Brien, Science **318**, 1567 (2007).

[10] P. Kok, W. J. Munro, K. Nemoto, T. C. Ralph, J. P. Dowling, and G. J. Milburn, Rev. Mod. Phys. **79**, 135 (2007).

[11] H.-S. Zhong, H. Wang, Y.-H. Deng, M.-C. Chen, L.-C. Peng, Y.-H. Luo, J. Qin, D. Wu, X. Ding, Y. Hu, P. Hu, X.-Y. Yang, W.-J. Zhang, H. Li, Y. Li, X. Jiang, L. Gan, G. Yang, L. You, Z. Wang, L. Li, N.-L. Liu, C.-Y. Lu, and J.-W. Pan, Science **370**, 1460 (2020).

[12] D. P. DiVincenzo, Fortschritte der Physik **48**, 771 (2000).

[13] P. Wang, C.-Y. Luan, M. Qiao, M. Um, J. Zhang, Y. Wang, X. Yuan, M. Gu, J. Zhang, and K. Kim, Nat Commun **12**, 233 (2021).

[14] C. Ballance, T. Harty, N. Linke, M. Sepiol, and D. Lucas, Phys. Rev. Lett. **117**, 060504 (2016).

[15] T. Harty, D. Allcock, C. Ballance, L. Guidoni, H. Janacek, N. Linke, D. Stacey, and D. Lucas, Phys. Rev. Lett. **113**, 220501 (2014).

[16] J. Zhang, G. Pagano, P. W. Hess, A. Kyprianidis, P. Becker, H. Kaplan, A. V. Gorshkov, Z.-X. Gong, and C. Monroe, Nature **551**, 601 (2017).

[17] A. H. Burrell, D. J. Szwer, S. C. Webster, and D. M. Lucas, Phys. Rev. A **81**, 040302 (2010).

[18] L. A. Zhukas, P. Svihra, A. Nomerotski, and B. B. Blinov, Phys. Rev. A **103**, 062614 (2021).

[19] J. M. Pino, J. M. Dreiling, C. Figgatt, J. P. Gaebler, S. A. Moses, M. S. Allman, C. H. Baldwin, M. Foss-Feig, D. Hayes, K. Mayer, C. Ryan-Anderson, and B. Neyenhuis, Nature **592**, 209 (2021).

[20] S. M. Clark, D. Lobser, M. Revelle, C. G. Yale, D. Bossert, A. D. Burch, M. N. Chow, C. W. Hogle, M. Ivory, J. Pehr, B. Salzbrenner, D. Stick, W. Sweatt, J. M. Wilson, E. Winrow, and P. Maunz, IEEE Trans. Quantum Eng. **2**, 1 (2021).

[21] X. Fernandez-Gonzalvo and M. Keller, Sci Rep **13**, 523 (2023).

[22] J. D. Sterk, H. Coakley, J. Goldberg, V. Hietala, J. Lechtenberg, H. McGuinness, D. McMurtrey, L. P. Parazzoli, J. Van Der Wall, and D. Stick, npj Quantum Inf **8**, 1 (2022).

[23] J. Hilder, D. Pijn, O. Onishchenko, A. Stahl, M. Orth, B. Lekitsch, A. Rodriguez-Blanco, M. Müller, F. Schmidt-Kaler, and U. Poschinger, Phys. Rev. X **12**, 011032 (2022).

[24] A. Walther, F. Ziesel, T. Ruster, S. T. Dawkins, K. Ott, M. Hettrich, K. Singer, F. Schmidt-Kaler, and U. Poschinger, Phys. Rev. Lett. **109**, 080501 (2012).

[25] V. Kaushal, B. Lekitsch, A. Stahl, J. Hilder, D. Pijn, C. Schmiegelow, A. Bermudez, M. Müller, F. Schmidt-Kaler, and U. Poschinger, AVS Quantum Science **2**, 014101 (2020).

[26] P. C. W. Davies, The Implications of a Cosmological Information Bound for Complexity, Quantum Information and the Nature of Physical Law (2007).

[27] W.-M. Zhang, D. H. Feng, and R. Gilmore, Rev. Mod. Phys. **62**, 867 (1990).

[28] M. Stobińska, H. Jeong, and T. C. Ralph, Phys. Rev. A **75**, 052105 (2007).

[29] C.-W. Lee, M. Paternostro, and H. Jeong, Phys. Rev. A **83**, 022102 (2011).

[30] J. Joo, W. J. Munro, and T. P. Spiller, Phys. Rev. Lett. **107**, 083601 (2011).

[31] J. Joo, K. Park, H. Jeong, W. J. Munro, K. Nemoto, and T. P. Spiller, Phys. Rev. A **86**, 043828 (2012).

[32] X. Wang, Phys. Rev. A **64**, 022302 (2001).

[33] H. Jeong and M. S. Kim, Phys. Rev. A **65**, 042305 (2002).

[34] H. Jeong, M. S. Kim, and J. Lee, Phys. Rev. A **64**, 052308 (2001).

[35] S. J. van Enk and O. Hirota, Phys. Rev. A **64**, 022313 (2001).

[36] S.-W. Lee and H. Jeong, Phys. Rev. A **87**, 022326 (2013).

[37] N. Ofek, A. Petrenko, R. Heeres, P. Reinhold, Z. Leghtas, B. Vlastakis, Y. Liu, L. Frunzio, S. M. Girvin, L. Jiang, M. Mirrahimi, M. H. Devoret, and R. J. Schoelkopf, Nature **536**, 441 (2016).

[38] C. Flühmann, T. L. Nguyen, M. Marinelli, V. Negnevitsky, K. Mehta, and J. P. Home, Nature **566**, 513 (2019).

[39] A. Ourjoumtsev, F. Ferreyrol, R. Tualle-Brouri, and P. Grangier, Nature Phys **5**, 189 (2009).

[40] Z. Wang, Z. Bao, Y. Wu, Y. Li, W. Cai, W. Wang, Y. Ma, T. Cai, X. Han, J. Wang, Y. Song, L. Sun, H. Zhang, and L. Duan, Science Advances **8**, eabn1778 (2022).

[41] C. Wang, Y. Y. Gao, P. Reinhold, R. W. Heeres, N. Ofek, K. Chou, C. Axline, M. Reagor, J. Blumoff, K. M. Sliwa, L. Frunzio, S. M. Girvin,

L. Jiang, M. Mirrahimi, M. H. Devoret, and R. J. Schoelkopf, Science **352**, 1087 (2016).

[42] C. Monroe, D. M. Meekhof, B. E. King, and D. J. Wineland, Science **272**, 1131 (1996).

[43] D. Kienzler, C. Flühmann, V. Negnevitsky, H.-Y. Lo, M. Marinelli, D. Nadlinger, and J. Home, Phys. Rev. Lett. **116**, 140402 (2016).

[44] J. Zhang, M. Um, D. Lv, J.-N. Zhang, L.-M. Duan, and K. Kim, Phys. Rev. Lett. **121**, 160502 (2018).

[45] A. C. Lee, J. Smith, P. Richerme, B. Neyenhuis, P. W. Hess, J. Zhang, and C. Monroe, Phys. Rev. A **94**, 042308 (2016).

[46] S. Weidt, J. Randall, S. Webster, E. Standing, A. Rodriguez, A. Webb, B. Lekitsch, and W. Hensinger, Phys. Rev. Lett. **115**, 013002 (2015).

[47] S. Weidt, J. Randall, S. Webster, K. Lake, A. Webb, I. Cohen, T. Navickas, B. Lekitsch, A. Retzker, and W. Hensinger, Phys. Rev. Lett. **117**, 220501 (2016).

[48] K. Lake, S. Weidt, J. Randall, E. D. Standing, S. C. Webster, and W. K. Hensinger, Phys. Rev. A **91**, 012319 (2015).

[49] P. C. Haljan, K.-A. Brickman, L. Deslauriers, P. J. Lee, and C. Monroe, Phys. Rev. Lett. **94**, 153602 (2005).

[50] B. Blinov, Physics **3**, 30 (2010).

[51] W. C. Campbell, J. Mizrahi, Q. Quraishi, C. Senko, D. Hayes, D. Hucul, D. N. Matsukevich, P. Maunz, and C. Monroe, Phys. Rev. Lett. **105**, 090502 (2010).

[52] R. Islam, E. E. Edwards, K. Kim, S. Korenblit, C. Noh, H. Carmichael, G.-D. Lin, L.-M. Duan, C.-C. Joseph Wang, J. K. Freericks, and C. Monroe, Nat Commun **2**, 377 (2011).

[53] E. Mount, D. Gaultney, G. Vrijsen, M. Adams, S.-Y. Baek, K. Hudek, L. Isabella, S. Crain, A. van Rynbach, P. Maunz, and J. Kim, Quantum Inf Process **15**, 5281 (2016).

[54] R. Islam, W. C. Campbell, T. Choi, S. M. Clark, C. W. S. Conover, S. Debnath, E. E. Edwards, B. Fields, D. Hayes, D. Hucul, I. V. Inlek, K. G. Johnson, S. Korenblit, A. Lee, K. W. Lee, T. A. Manning, D. N. Matsukevich, J. Mizrahi, Q. Quraishi, C. Senko, J. Smith, and C. Monroe, Opt. Lett., OL **39**, 3238 (2014).

[55] R. C. Sterling, H. Rattanasonti, S. Weidt, K. Lake, P. Srinivasan, S. C. Webster, M. Kraft, and W. K. Hensinger, Nat Commun **5**, 3637 (2014).

[56] Y. Park, C. Jung, M. Seong, M. Lee, D. D. Cho, and T. Kim, Sensors **21**, 1143 (2021).

[57] K. G. Johnson, J. D. Wong-Campos, A. Restelli, K. A. Landsman, B. Neyenhuis, J. Mizrahi, and C. Monroe, Review of Scientific Instruments **87**, 053110 (2016).

[58] Y. Shen, *Quantum chemistry simulation with trapped ion device*, Ph.D. thesis, Tsinghua University (2018).

[59] F. Schmidt-Kaler, H. Häffner, S. Gulde, M. Riebe, G. Lancaster, T. Deuschle, C. Becher, W. Hänsel, J. Eschner, C. Roos, and R. Blatt, Appl. Phys. B **77**, 789 (2003).

[60] H. Jeon, J. Kang, J. Kim, W. Choi, K. Kim, and T. Kim, Experimental Realization of Entangled Coherent States in Two-dimensional Harmonic Oscillators of a Trapped Ion (2023).

[61] T. J. Barrett, W. Evans, A. Gadge, S. Bhumbra, S. Sleegers, R. Shah, J. Fekete, F. Oručević, and P. Krüger, Quantum Sci. Technol. **7**, 025001 (2022).

[62] G. Kasprowicz, P. Kulik, M. Gaska, T. Przywozki, K. Pozniak, J. Jarosinski, J. W. Britton, T. Harty, C. Balance, W. Zhang, D. Nadlinger, D. Slichter, D. Allcock, S. Bourdeauducq, R. Jördens, and K. Pozniak, in EN*OSA Quantum 2.0 Conference (2020), paper QTu8B.14* (Optica Publishing Group, 2020) p. QTu8B.14.

[63] C. J. Foot and C. J. Foot, *Atomic Physics*, Oxford Master Series in Physics (Oxford University Press, Oxford, New York, 2004).

[64] D. Leibfried, R. Blatt, C. Monroe, and D. Wineland, Rev. Mod. Phys. **75**, 281 (2003).

[65] H. Che, K. Deng, Z. T. Xu, W. H. Yuan, J. Zhang, and Z. H. Lu, Phys. Rev. A **96**, 013417 (2017).

[66] S. Debnath, en*A Programmable Five Qubit Quantum Computer Using Trapped Atomic Ions*, Ph.D. thesis, University of Maryland (2016).

[67] J. Keller, H. L. Partner, T. Burgermeister, and T. E. Mehlstäubler, Journal of Applied Physics **118**, 104501 (2015).

[68] W. Lee, D. Chung, J. Kang, H. Jeon, C. Jung, D.-I. D. Cho, and T. Kim, In-situ micromotion compensation of trapped ions by Rabi oscillation and direct scanning of dc voltages (2023).

[69] C. Monroe, D. M. Meekhof, B. E. King, S. R. Jefferts, W. M. Itano, D. J. Wineland, and P. Gould, Phys. Rev. Lett. **75**, 4011 (1995).

[70] L. Deslauriers, S. Olmschenk, D. Stick, W. K. Hensinger, J. Sterk, and C. Monroe, Phys. Rev. Lett. **97**, 103007 (2006).

[71] I. A. Boldin, A. Kraft, and C. Wunderlich, Phys. Rev. Lett. **120**, 023201 (2018).

[72] S. Olmschenk, K. C. Younge, D. L. Moehring, D. N. Matsukevich, P. Maunz, and C. Monroe, Phys. Rev. A **76**, 052314 (2007).

[73] R. F. Spivey, en*A Compact Cryogenic Package Approach to Ion Trap Quantum Computing*, Ph.D. thesis, Duke University (2022).

[74] C. M. Dawson and M. A. Nielsen, Quantum Info. Comput. **6**, 81 (2006).

[75] A. Y. Kitaev, Russ. Math. Surv. **52**, 1191 (1997).

[76] M. A. Nielsen and I. L. Chuang, *Quantum Computation and Quantum Information* (Cambridge University Press, 2010).

[77] D. C. McKay, C. J. Wood, S. Sheldon, J. M. Chow, and J. M. Gambetta, Phys. Rev. A **96**, 022330 (2017).

[78] H. Jeon, N. Park, J. Yu, Y.-D. Kwon, D. Yum, and W. Jhe, J. Korean Phys. Soc. **78**, 251 (2021).

[79] J. Emerson, R. Alicki, and K. Życzkowski, J. Opt. B: Quantum Semiclass. Opt. **7**, S347 (2005).

[80] E. Knill, D. Leibfried, R. Reichle, J. Britton, R. B. Blakestad, J. D. Jost, C. Langer, R. Ozeri, S. Seidelin, and D. J. Wineland, Phys. Rev. A **77**, 012307 (2008).

[81] A. Sørensen and K. Mølmer, Phys. Rev. A **62**, 022311 (2000).

[82] E. Merzbacher, English*Quantum Mechanics*, 3rd ed. (Wiley, New York, 1997).

[83] T. Choi, S. Debnath, T. Manning, C. Figgatt, Z.-X. Gong, L.-M. Duan, and C. Monroe, Phys. Rev. Lett. **112**, 190502 (2014).

[84] M. Kang, Q. Liang, B. Zhang, S. Huang, Y. Wang, C. Fang, J. Kim, and K. R. Brown, Phys. Rev. Appl. **16**, 024039 (2021).

[85] R. Blümel, N. Grzesiak, N. H. Nguyen, A. M. Green, M. Li, A. Maksymov, N. M. Linke, and Y. Nam, Phys. Rev. Lett. **126**, 220503 (2021).

[86] Y. Lu, S. Zhang, K. Zhang, W. Chen, Y. Shen, J. Zhang, J.-N. Zhang, and K. Kim, Nature **572**, 363 (2019).

[87] P. H. Leung, K. A. Landsman, C. Figgatt, N. M. Linke, C. Monroe, and K. R. Brown, Phys. Rev. Lett. **120**, 020501 (2018).

[88] D. Hayes, S. M. Clark, S. Debnath, D. Hucul, I. V. Inlek, K. W. Lee, Q. Quraishi, and C. Monroe, Phys. Rev. Lett. **109**, 020503 (2012).

[89] Q. A. Turchette, C. S. Wood, B. E. King, C. J. Myatt, D. Leibfried, W. M. Itano, C. Monroe, and D. J. Wineland, Phys. Rev. Lett. **81**, 3631 (1998).

[90] D. Kielpinski, J. Opt. B: Quantum Semiclass. Opt. **5**, R121 (2003).

[91] D. Leibfried, D. M. Meekhof, B. E. King, C. Monroe, W. M. Itano, and D. J. Wineland, Phys. Rev. Lett. **77**, 4281 (1996).

[92] D. Lv, S. An, M. Um, J. Zhang, J.-N. Zhang, M. S. Kim, and K. Kim, Phys. Rev. A **95**, 043813 (2017).

[93] D. Hayes, D. N. Matsukevich, P. Maunz, D. Hucul, Q. Quraishi, S. Olmschenk, W. Campbell, J. Mizrahi, C. Senko, and C. Monroe, Phys. Rev. Lett. **104**, 140501 (2010).

[94] C. Ballance, *High-fidelity quantum logic in Ca+*, Ph.D. thesis, University of Oxford (2014).

[95] L. N. Egan, *Scaling Quantum computers with Long chains of trapped ions*, Ph.D. thesis, University of Maryland (2021).

[96] U. Poschinger, A. Walther, K. Singer, and F. Schmidt-Kaler, Phys. Rev. Lett. **105**, 263602 (2010).

[97] A. Ourjoumtsev, H. Jeong, R. Tualle-Brouri, and P. Grangier, Nature **448**, 784 (2007).

[98] A. Ourjoumtsev, A. Dantan, R. Tualle-Brouri, and P. Grangier, Phys. Rev. Lett. **98**, 030502 (2007).

[99] B. Vlastakis, G. Kirchmair, Z. Leghtas, S. E. Nigg, L. Frunzio, S. M. Girvin, M. Mirrahimi, M. H. Devoret, and R. J. Schoelkopf, Science **342**, 607 (2013).

[100] H. Jeong and N. B. An, Phys. Rev. A **74**, 022104 (2006).

[101] K. Park and H. Jeong, Phys. Rev. A **82**, 062325 (2010).

[102] B. de Neeve, T.-L. Nguyen, T. Behrle, and J. P. Home, Nat. Phys. **18**, 296 (2022).

[103] W. Chen, Y. Lu, S. Zhang, K. Zhang, G. Huang, M. Qiao, X. Su, J. Zhang, J.-N. Zhang, L. Banchi, M. S. Kim, and K. Kim, Nat. Phys. , 1 (2023).

[104] D. M. Meekhof, C. Monroe, B. E. King, W. M. Itano, and D. J. Wineland, Phys. Rev. Lett. **76**, 1796 (1996).

[105] K. E. Cahill and R. J. Glauber, Phys. Rev. **177**, 1857 (1969).

[106] C. C. Gerry, Phys. Rev. A **55**, 2478 (1997).

[107] X.-B. Zou, J. Kim, and H.-W. Lee, Phys. Rev. A **63**, 065801 (2001).

[108] E. Solano, R. L. d. M. Filho, and N. Zagury, J. Opt. B: Quantum Semiclass. Opt. **4**, S324 (2002).

[109] Q. A. Turchette, C. J. Myatt, B. E. King, C. A. Sackett, D. Kielpinski, W. M. Itano, C. Monroe, and D. J. Wineland, Phys. Rev. A **62**, 053807 (2000).

[110] H. Gan, G. Maslennikov, K.-W. Tseng, C. Nguyen, and D. Matsukevich, Phys. Rev. Lett. **124**, 170502 (2020).

[111] K. Toyoda, R. Hiji, A. Noguchi, and S. Urabe, Nature **527**, 74 (2015).

[112] W. C. Campbell and P. Hamilton, J. Phys. B: At. Mol. Opt. Phys. **50**, 064002 (2017).

[113] A. Shinjo, M. Baba, K. Higashiyama, R. Saito, and T. Mukaiyama, Phys. Rev. Lett. **126**, 153604 (2021).

[114] S. Martínez-Garaot, A. Rodriguez-Prieto, and J. G. Muga, Phys. Rev. A **98**, 043622 (2018).

[115] R. F. Rossetti, G. D. d. M. Neto, J. C. Egues, and M. H. Y. Moussa, EPL **115**, 53001 (2016).

[116] T. A. Manning, *Quantum information processing with trapped ion chains*, Ph.D. thesis, University of Maryland (2014).

[117] C. Jung, W. Lee, J. Jeong, M. Lee, Y. Park, T. Kim, and D.-I. D. Cho, Quantum Sci. Technol. **6**, 044004 (2021).

[118] S. X. Wang, G. Hao Low, N. S. Lachenmyer, Y. Ge, P. F. Herskind, and I. L. Chuang, Journal of Applied Physics **110**, 104901 (2011).

[119] M. Harlander, M. Brownnutt, W. Hänsel, and R. Blatt, New J. Phys. **12**, 093035 (2010).

[120] M. Madsen, W. Hensinger, D. Stick, J. Rabchuk, and C. Monroe, Appl Phys B **78**, 639 (2004).

[121] Y. Aikyo, G. Vrijsen, T. W. Noel, A. Kato, M. K. Ivory, and J. Kim, Applied Physics Letters **117**, 234002 (2020).

[122] I. Pogorelov, T. Feldker, C. D. Marciniak, L. Postler, G. Jacob, O. Krieglsteiner, V. Podlesnic, M. Meth, V. Negnevitsky, M. Stadler, B. Höfer, C. Wächter, K. Lakhmanskiy, R. Blatt, P. Schindler, and T. Monz, PRX Quantum **2**, 020343 (2021).